Imperial College London

Bulk and Surface Recombination Losses in Planar Perovskite Solar Cells

by

Tian Du

A thesis submitted in partial fulfilment for the degree of Doctor of Philosophy

in the

Plastic Electronics Centre for Doctoral Training

&

Department of Materials

February 2020

Declaration of Originality

This thesis is a summary of work carried out in the Department of Materials and the Centre of Plastic Electronics at Imperial College London between October 2015 and December 2019, under the supervision of Dr Martyn McLachlan and Prof. James Durrant. I declare that the work present in this thesis is my own except where specific reference is made to the contribution of others.

Tian Du

January 2020

Copyright Declaration

In early 2020, we stand firmly with the people fighting against the COVID-19

Abstract

This thesis summarizes the experimental studies on the recombination mechanisms in planar “p-i-n” type perovskite solar cells (PSCs), focusing on the role of both photoactive layer and charge transport layers. The work carried out both materials characterisation and optoelectronic measurements, probing the physical origin charge recombination and assessing their impacts on solar cell power conversion efficiency (PCE). The origin of open-circuit voltage (V_{OC}) is considered, the importance of controlling defects in photoactive layer and controlling doping level of charge transport layer is highlighted, and a couple of design principles for high-performance PSCs are discussed

In Chapter 1 an introduction of semiconductor physics relevant to solar-to-electrical energy conversion is presented, followed with a review of solar cells physics, materials and application. Chapter 2 focuses on the principle and data interpretation of the experimental methods employed in this thesis, including X-ray diffraction, electron microscopy, surface probe, photoluminescence spectroscopy and transient optoelectronic measurements.

Chapter 3 reports how the crystallinity of thin-film perovskites can be modulated by tuning the stoichiometry of precursor mix in solution processing. This chapter elucidates that both V_{OC} and PCE are governed by electronic trap states in perovskites that are correlated to the crystallinity of perovskite films. In Chapter 4 a facile modification on solution processing is reported that can remarkably remove microstructural defects in perovskite thin films, presenting both detailed microscopic characterisation of these defects and optoelectronic characterisation of their impact device performance. Chapter 5 moves from bulk perovskite to hole transport layers (HTLs), elucidating how the p-doping of HTLs causes surface recombination and is

averse to device performance. Finally, Chapter 6, new insights into the fundamental operational principles of PSC are discussed and further work based this thesis are suggested.

Acknowledgements

I had a great time at Imperial College carrying out my study and research for a doctoral degree from 2015 to 2019 and completed this thesis in early 2020. While this degree is often recognized as individual academic achievement, it is for sure shared by people and organizations that have given me firm support. It is you who makes the journal of PhD no longer lonely, and it thanks to you that I convince myself to be fully devoted in my study and research.

I would like to express my gratitude to the following people:

First of all to the donor of Stephen and Anna Hui Fellowship, Dr Stephen Hui and his family, for their financial support: your support makes the whole thing happen.

To Dr Martyn McLachlan, for being a kind, supportive and considerate academic supervisor. You always understand and help with the daily issues of a PhD student, the need for funding and the need for publishing more papers in higher-impact journals

To professor James Durrant for leading my way into the real research by always saying “show me the evidence”. I appreciate your timely reminding me to “slow down” to thinking deeper and learn more.

To my parents who stand firmly behind me, with both mental and financial support. The home visit occurs once or twice a year remains the paramount excitement of the year.

To my girlfriend, Yizhu Zhu, who just obtained her PhD degree a couple of weeks ago, for always understanding and supporting me, for our mutual encouragement during our journey.

To Jinhyun Kim (JK) for your excellence in lab tricks and spectroscopic measurement, Clair Burgess for your magics in TEM sample preparation and imaging, Shengda Xu for always getting the most proper XRD, SEM and absorption measurement. To Jiaqi Zhang for the orientation in the group when I was off the boat. To Chieh-Ting Lin, Weidong Xu and Dr Tom Macdonald for being in the “perovskite squad”.

To Dr Piers Barnes for our wonderful scientific discussion with your “let me teach you something” enlightening. To Professor Ji-seon Kim and Professor Martin Heeney for your kind support.

To Dr Xiao’e Li and Dr Pabitra Shakya Tuladhar for your kind “babysitting” technical support.

To all the past and current members of McLachlan group and Durrant group for your accompany and support – you make me feel that I am not alone for this journey.

To people in the Room 101 of RSM building and people in Room B60 of Chemistry building in SK campus, people in the fourth floor office and ground floor office of MSRH building White City campus.

To China Scholarship Council for nominating me for the Imperial-CSC scholarship (although I kindly rejected that and accepted the other).

This is a start rather than an end.

Content

List of Parameters or Constant

Description	Parameter or constant	Unit
Band gap	E_g	eV
Electron density	n	cm^{-3}
Hole density	p	cm^{-3}
Effective conduction band density of states	N_C	cm^{-3}
Effective valence band density of states	N_V	cm^{-3}
Boltzmann constant	K_B	eV K^{-1}
Temperature	T	K
Thermal energy	K_BT	eV
Fermi level	E_F	eV
Intrinsic charge carrier density	n_i	cm^{-3}
Intrinsic potential energy of semiconductor	E_i	eV
Electron mobility	μ_n	cm^2 s^{-1} V^{-1}
Donor density	N_d	cm^{-3}
Acceptor density	N_a	cm^{-3}
Hole mobility	μ_p	cm^2 s^{-1} V^{-1}
Unit charge	q	C
Conductivity	σ	Ohm^{-1} cm^{-1}
Electron quasi Fermi level	$E_{F,n}$	eV
Hole quasi Fermi level	$E_{F,p}$	eV
Quasi-Fermi level splitting	ΔE_F	eV
Electron diffusion coefficient	D_n	cm^2 s^{-1}
Hole diffusion coefficient	D_p	cm^2 s^{-1}
Electrostatic field	F	V cm^{-1}
Charge generation rate	G_n	cm^{-3} s^{-1}
Charge recombination rate	U_n	cm^{-3} s^{-1}
Absorption coefficient	α	cm^{-1}

Radiative recombination rate	U_{rad}	cm^{-3} s^{-1}
Radiative recombination coefficient	B_{rad}	cm^{3} s^{-1}
Non-radiative recombination rate	U_{nr}	cm^{-3} s^{-1}
Non-radiative recombination coefficient	B_{nr}	cm^{3} s^{-1}
Density of trap states	N_t	cm^{-3}
Probability of trap state occupation	f_t	--
Surface recombination velocity	S	cm s^{-1}
Surface recombination constant	B	cm^{3} s^{-1}
Surface charge density	N_S	cm^{-2}
Energy depth of trap states	E_t	eV
Release time of trapped charge	$\tau_{release}$	s
The time of charge being trapped	$\tau_{capture}$	s
Work function	$\emptyset$	eV
Vacuum energy level	E_{vac}	eV
Built-in bias	V_{bi}	V cm^{-1}
Permittivity of semiconductor	ε_s	F m^{-1}
Dark current density	J_{dark}	mA cm^{-2}
Saturation current	J_0	mA cm^{-2}
Photon flux	ϕ	m^{-2}
Spectral solar irradiance	F	W m^{-2} µm^{-1}
Photocurrent density	J_{ph}	mA cm^{-2}
Short circuit current density	J_{SC}	mA cm^{-2}
Open circuit voltage	V_{OC}	V
Fill factor	FF	--
Voltage at maximum power point	V_{max}	V
Current at maximum power point	J_{max}	mA cm^{-2}
Power conversion efficiency	η	%
Incident light power density	P_{in}	W m^{-2}
Goldsmidt tolerance factor	t	--
Secondary electron yield	δ	%
Spacing between adjacent lattice planes	d	Å

Incident angle of X-ray	θ	degree
Wavelength of radiation beam	λ	nm
Electrical potential	φ	V
Small-perturbation photovoltage	ΔV	V
Pseudo-first-order recombination constant	$k_{\Delta n}$	s^{-1}
Density-dependent recombination constant	k_0	cm^{-x} s^{-1}
Density-independent recombination constant	k_n	s^{-1}
Pseudo-first-order recombination lifetime	$\tau_{\Delta n}$	s
Recombination order	δ	--
Small-perturbation excessive charge	ΔQ	C
Charge density	n	cm^{-3}
Differential capacitance	C_{DC}	nF
Recombination current	J_{Rec}	mA cm^{-2}
Light ideality factor	n_{id}	--
Linearity of J_{SC} with light intensity	α	--

List of Abbreviations

Abbreviation	Description
VB	Valence band
CB	Conduction band
WF	Work function
EA	Electron affinity
IP	Ionization potential
SRH	Shockley Read Hall
ETL	Electron transport layer
HTL	Hole transport layer
CTL	Charge transport layer
AM1.5	Air mass 1.5
a-Si	Amorphous silicon
TCO	Transparent conductive oxide
DSSC	Dye-sensitized solar cell
OSC	Organic solar cell
BHJ	Bulk heterojunction
HOMO	Highest occupied molecular orbital
LUMO	Lowest unoccupied molecular orbital
PCE	Power conversion efficiency
PSC	Perovskite solar cell
J-V	Current density-voltage
OHP	Organic-inorganic halide perovskite
XPS	X-ray photoemission spectroscopy
DOS	Density of states
MA	Methylammonium

FA	Formamidinium
ITO	Indium-doped tin oxide
PEDOT:PSS	Poly(3,4ethylenedioxythiophene)-poly(styrene sulfonate)
PTAA	Poly[bis(4-phenyl)(2,4,6-trimethylphenyl)amine]
PTPD	Poly[N,N’-bis(4-butylphenyl)-N,N’-bis(phenyl)benzidine]
PFN	Poly [(9,9-bis(3'-(N,N-dimethylamino)propyl)-2,7-fluorene)-alt-2,7-(9,9–dioctylfluorene)]
MAI	Methylammonium iodide
MAPI	Methylammonium lead iodide
PTFE	Polytetrafluoroethylene
DMSO	Dimethyl sulfoxide
GBL	Gamma-butyrolactone
DMF	N,N-Dimethylmethanamide
PCBM	Phenyl-C61-butyricacid methylester
EQE	External quantum efficiency
SEM	Scanning electron microscopy
EDS	Energy-dispersive spectroscopy
TEM	Transmission electron microscopy
XRD	X-ray diffraction
BF	Bright field
DF	Dark field
STEM	Scanning transmission electron microscopy
ADF	Annular dark field
HRTEM	High-resolution TEM
KPFM	Kelvin probe force microscopy
CPD	Contact potential difference
AFM	Atomic force microscopy

PL	Photoluminescence
TRPL	Time-resolved PL
TCSPC	Time-correlated single photon counting
TAS	Transient absorption spectroscopy
TPV	Transient photovoltage
TPC	Transient photocurrent
DC	Differential charging
CE	Charge extraction
OC	Open circuit
SC	Short circuit
SIMS	Secondary ion mass spectroscopy
SAED	Selected area electron diffraction
PLQ	Photoluminescence quenching
PL_{OC}	Open circuit PL emission intensity
PL_{SC}	Short circuit PL emission intensity
PLQ_{OC-SC}	Open circuit to short circuit PL quenching efficiency

Publications

- **Du, T** *et al*. Light-Intensity and Thickness Dependent Efficiency of Planar Perovskite Solar Cells: Charge Recombination versus Extraction. *Under review*

- **Du, T.**, Xu, W., Daboczi, M., Kim, J., Xu, S., Lin, C. T., ... & Durrant, J. R. (2019). p-Doping of organic hole transport layers in p–i–n perovskite solar cells: correlating open-circuit voltage and photoluminescence quenching. *Journal of Materials Chemistry A*, *7*(32), 18971-18979.

- **Du, T.**, Burgess, C. H., Lin, C. T., Eisner, F., Kim, J., Xu, S., ... & McLachlan, M. A. (2018). Probing and Controlling Intragrain Crystallinity for Improved Low Temperature–Processed Perovskite Solar Cells. *Advanced Functional Materials*, *28*(51), 1803943.

- **Du, T.**, Kim, J., Ngiam, J., Xu, S., Barnes, P. R., Durrant, J. R., & McLachlan, M. A. (2018). Elucidating the Origins of Subgap Tail States and Open-Circuit Voltage in Methylammonium Lead Triiodide Perovskite Solar Cells. *Advanced Functional Materials*, *28*(32), 1801808.

- **Du, T**., Burgess, C. H., Kim, J., Zhang, J., Durrant, J. R., & McLachlan, M. A. (2017). Formation, location and beneficial role of PbI2 in lead halide perovskite solar cells. *Sustainable Energy & Fuels*, *1*(1), 119-126.

- Kim, J., Godin, R., Dimitrov, S. D., **Du, T.**, Bryant, D., McLachlan, M. A., & Durrant, J. R. (2018). Excitation Density Dependent Photoluminescence Quenching and Charge Transfer Efficiencies in Hybrid Perovskite/Organic Semiconductor Bilayers. *Advanced Energy Materials*, *8*(35), 1802474.

- Wijeyasinghe, N., Regoutz, A., Eisner, F., **Du, T**., Tsetseris, L., Lin, Y. H., ... & McLachlan, M. A. (2017). Copper (I) Thiocyanate (CuSCN) Hole-Transport Layers Processed from Aqueous Precursor Solutions and Their Application in Thin-Film Transistors and Highly Efficient Organic and Organometal Halide Perovskite Solar Cells. *Advanced Functional Materials*, *27*(35), 1701818.

- Wijeyasinghe, N., Tsetseris, L., Regoutz, A., Sit, W. Y., Fei, Z., **Du, T.**, ... & Payne, D. J. (2018). Copper (I) Selenocyanate (CuSeCN) as a Novel Hole-Transport Layer for Transistors, Organic Solar Cells, and Light-Emitting Diodes. *Advanced Functional Materials*, *28*(14), 1707319.

- Lin, C. T., Pont, S., Kim, J., **Du, T.**, Xu, S., Li, X., ... & Durrant, J. R. (2018). Passivation against oxygen and light induced degradation by the PCBM electron transport layer in planar perovskite solar cells. *Sustainable Energy & Fuels*, *2*(8), 1686-1692.

- Godin, R., Ma, X., González‐Carrero, S., **Du, T.**, Li, X., Lin, C. T., ... & Durrant, J. R. (2018). Tuning Charge Carrier Dynamics and Surface Passivation in Organolead Halide Perovskites with Capping Ligands and Metal Oxide Interfaces. *Advanced Optical Materials*, *6*(5), 1701203.

- Zhang, J., Morbidoni, M., Burgess, C. H., Wu, J., **Du, T.**, Harrabi, K., ... & McLachlan, M. A. (2017). Nanoscale Structure–Property Relationships in Low-Temperature Solution-Processed Electron Transport Layers for Organic Photovoltaics. *Crystal Growth & Design*, *17*(12), 6559-6564.

- Zhang, J., Tan, C. H., **Du, T.**, Morbidoni, M., Lin, C. T., Xu, S., ... & McLachlan, M. A. (2018). ZnO-PCBM bilayers as electron transport layers in low-temperature processed perovskite solar cells. *Science bulletin*, *63*(6), 343-348.

1. Theory and Background

The fundamental materials for photovoltaics are semiconductors. In this chapter a brief introduction of semiconductor physics that is relevant to photovoltaics is presented, followed with a couple of fundamental issues related to solar cell operation. Next the designs and working mechanism of a couple of photovoltaic technologies developed in recent decades are described and compared. A brief introduction on the crystallography and chemistry of metal halide perovskite materials is also presented. This chapter aims at providing a general background of the research topics relevant to my PhD studies.

1.1 Fundamentals of Semiconductors

Suitable photovoltaic (PV) materials are semiconductors with appropriate band gap (E_g). The E_g of semiconductors permits visible light absorption and provides additional potential energy for photoexcited charge carriers and allows photoexcited carriers to stay in higher energy levels at sufficient time scale to be transferred and extracted. In case of insulators, normally having rather large band gap, insufficiently absorbs the visible light. In other cases, electrons that are excited through a continuum of energy levels, such as in metals, would rapidly relax to their ground state. Similar relaxation occurs in presence of empty intra-gap electronic states can considerably accelerate charge recombination rate. For the same reason, electrons excited above the conduction band gap with rather high energy rapidly relaxes into the lowest available energy state in the conduction band, a process termed "thermalization" that occurs within femtoseconds (10^{-15} s).[1]

Energy levels are formed of large amount of split atomic orbitals when atoms come together in a solid. The "band" consists of a continuum of energy levels that charge carriers can occupy. Valence band (VB) is partially filled with valence electrons and these electrons can be excited into conduction band (CB) under certain circumstances (e.g. thermal or photo excitation). In typical semiconductors the VB is separated from CB with a certain energy, the E_g, of approximately 0.5 - 3 eV. The energetics of the bands are determined both by the crystal structure and the atoms/ions in the structure – there are a couple of works showing that the excellent optoelectronic properties of the metal halide perovskites to presence of heavy metal the crystal structure.[2–4]

1.1.1. Charge Carriers in Semiconductor

Charge Density at Equilibrium

One of the most important quantities of semiconductor density of charge carriers. The electron and hole density at equilibrium, *i.e.* no net exchanges of particles or energy between different points, is determined by density of states near the band edge and Fermi Dirac distribution function that governs the probability of electrons and holes occupying these states. With Fermi Dirac distribution function, combined with Boltzmann approximation, the electron (n) and hole (p) densities are determined by

$$n = N_C \exp\left(\frac{E_F - E_C}{k_B T}\right) \tag{1.1}$$

$$p = N_V \exp\left(\frac{E_V - E_F}{k_B T}\right) \tag{1.2}$$

where N_c and N_v are effective CB or VB density of states, k_B is the Boltzmann constant, T is temperature, and E_F is Fermi level of the semiconductor. These equations suggest that the electron and hole density depend exponentially on the relative position of E_F with respect to band edge.

From equations 1.1 and 1.2 it can be found that the product of electron and hole density is constant for a given temperature:

$$np = N_C N_V \exp\left(\frac{E_V - E_C}{k_B T}\right) = n_i^2 \tag{1.3}$$

where the constant intrinsic carrier density, n_i, can be defined. It describes the density of thermally excited electrons in the CB in thermal equilibrium (*i.e.* without illumination or bias) in intrinsic semiconductors. Equation 1.3 highlights that the intrinsic charge density is also related to energetic properties of these bands (N_v, N_c and E_g) and temperature. Combining equations (1.1), (1.2) and (1.3) shows that both n and

p can be written as a function of n_i and an intrinsic potential energy, E_i, that is equal to the E_F of the semiconductor at equilibrium.

Charge density critically determines the conductivity of semiconductor:

$$\sigma = q\mu_n n + q\mu_p p \qquad (1.4)$$

in above equation μ_n and μ_p [cm^2 s^{-1} V^{-1}] are electron and hole mobility that is correlated to multiple properties of the semiconductor. To improve charge density and thus conductivity semiconductors can be doped by replacing some of the atoms with impurities, in such case additional charge carriers, as well as electronic states, are introduced and the semiconductors are no longer intrinsic. The type of doping depends on whether impurity atoms can donate electrons to the CB (n-type) or accept holes from the VB (p-type). In **Figure 1.1 a** the schematic drawing of band diagram of intrinsic, n-type and p-type semiconductors are shown. In doped semiconductors the density of charge carriers is now controlled by density of dopants, as the density of donor, N_d, is typically much greater than n_i and are fully ionized at room temperature. As such at equilibrium $n = N_d$ and $p = \frac{n_i^2}{N_d}$. In this case the electron density is greatly enhanced becoming the majority carrier, whereas hole density is reduced as minority carrier: *i.e.* the semiconductors have more electrons than holes with charge neutrality balanced by having more positive ions (n-type dopants) than negative ions. The equilibrium Fermi level now is no longer in the centre of band gap but lies between donor states and the CB. If the semiconductor is mainly doped with acceptors with density of N_a, then $p = N_a$ and $n = \frac{n_i^2}{N_a}$. Now the majority carriers are holes and the equilibrium E_F lie between VB and acceptor states.

Charge Density at Non-equilibrium

The above analysis considers semiconductors at equilibrium, however in most solar cell operational conditions equilibrium *i.e.* under illumination or electrical bias, the semiconductors are away from equilibrium. Under these circumstances excess charge carriers are generated either optically (by photoexcitation) or electrically (by injection) and $np = n_i^2$ no longer holds. The semiconductor is now governed by a quasi thermal equilibrium, with the density of electrons and holes described by the quasi Fermi levels, $E_{F,n}$ and $E_{F,p}$, respectively.

In quasi thermal equilibrium with split electron and hole quasi Fermi levels, electron and hole density can be expressed as[1]

$$n = n_i \exp\left(\frac{E_{F,n} - E_i}{K_B T}\right) \tag{1.5}$$

$$p = p_i \exp\left(\frac{E_i - E_{F,p}}{K_B T}\right) \tag{1.6}$$

Now the charge densities are determined by the petition of quasi-Fermi level. The product of electron and hole density is now written as[1]

$$np = n_i{}^2 \exp\left(\frac{E_{F,n} - E_{F,p}}{K_B T}\right) \tag{1.7}$$

$$E_{F,n} - E_{F,p} = \Delta E_F \tag{1.8}$$

where ΔE_F refers to quasi-Fermi level splitting in the semiconductor, a key parameter determines open-circuit voltage of a solar cell.[5]

Charge Transport in Semiconductor

At non-equilibrium conditions electrical conduction occurs, *i.e.* there are electron and hole current flowing in the semiconductor -- a fundamental process of semiconductor devices. Charge transport can be described using Boltzmann transport equation:

$$J_n = \mu_n n \nabla E_{F,n} \tag{1.9}$$

$$J_p = \mu_p \mathrm{p} \nabla E_{F,p} \tag{1.10}$$

Where J_n and J_p are electron and hole current density [A cm^{-2}], respectively. Importantly, the equations suggest that electron or hole current is driven by gradient of quasi Fermi levels. As we schematically show in **Figure 1.1 b**, in general Fermi level gradient can be created by i) a gradient in CB or VB edges that are typically caused by electric field or ii) a gradient in carrier density.

Further analyses show that J_n and J_p can then be resolved into i) a drift current, where carriers are driven by electric field to reduce their electrostatic potential energy, and ii) a diffusion current, caused by concentration gradient of carriers to reduce their

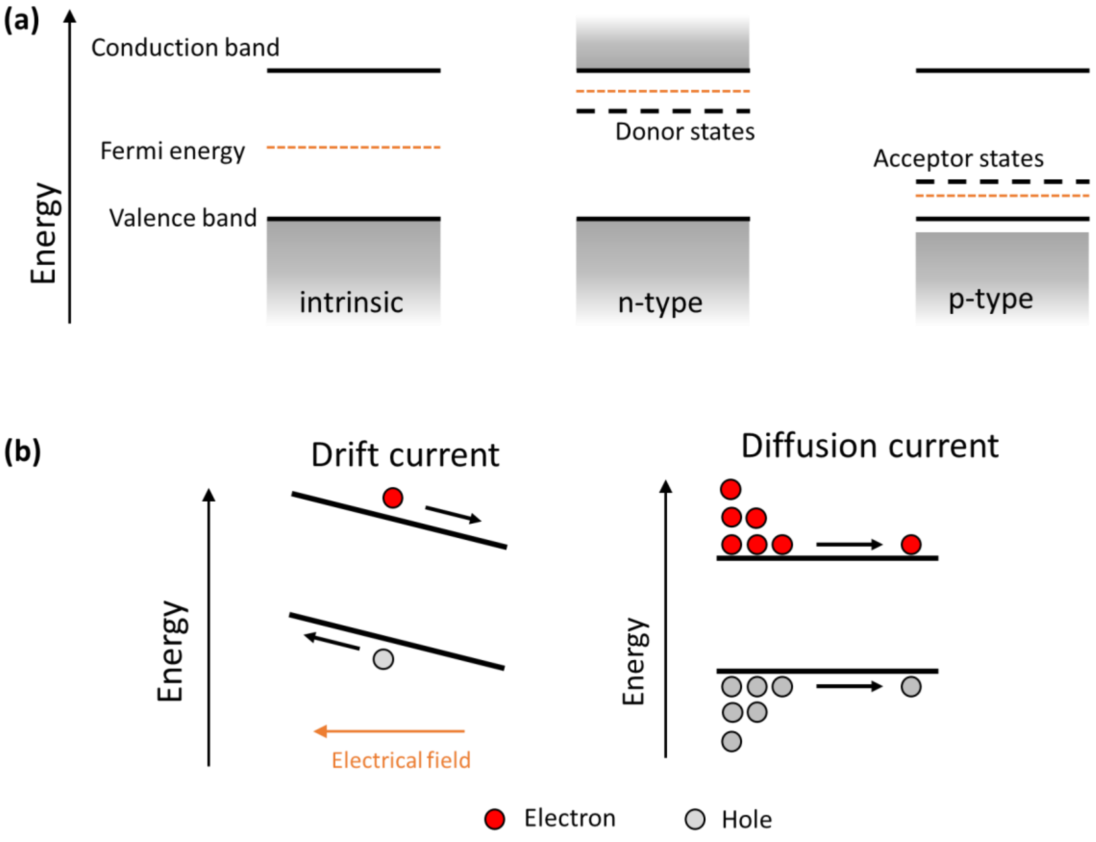

Figure 1.1 Schematic drawing of semiconductor band diagram. **(a)** Band diagram of intrinsic (left), n-type (middle) and p-type (right) semiconductors. **(b)** Formation of drift current and diffusion current in semiconductor.

statistical potential energy, written as

$$J_n = qD_n \nabla \mathrm{n} + qn\mu_n F_n \tag{1.11}$$

$$J_p = qD_p \nabla \mathrm{p} + qn\mu_p F_p \tag{1.12}$$

where D_n and D_p [cm^2 s^{-1}] are charge diffusion coefficient, F_n and F_p are electrostatic field [V cm^{-1}]. Drift and diffusion current are both close correlated to charge transfer/transport in solar cell operation,[6] and are key considerations in modelling of solar cells.[7] They show that net current in a semiconductor originate from gradient of charge density and/or applied electrical field, where both of these quantifies causes a gradient in fermi energy. In real solar cell operation at open circuit or maximum power point, diffusion current is likely dominant as most of the band edges are likely flattened, which is even more likely in the case of perovskite solar cells owing to screening of electrical field by ionic defects.[7]

1.1.2. Recombination

The output of a solar cell is determined by change generation, charge transport and charge recombination. These processes can be all summarised in one equation:

$$\frac{\partial n}{\partial t} = \frac{1}{q} \nabla J_n + G_n - U_n \tag{1.13}$$

where G_n [cm^{-3} s^{-1}] is generation rate and U_n [cm^{-3} s^{-1}] recombination rate. This equation lays the fundamental of the physics of solar cell, highlighting that the variation of charge density in a semiconductor or solar cell is the sum of generation, transport and recombination.

Light Absorption

Charge generation relies on absorption of light by semiconductors. Attenuation of light passing through the material can be described by the Beer-Lambert law[1]

$$I(x) = I(0)\exp(-\alpha x) \tag{1.14}$$

where α is absorption coefficient [cm^{-1}] and is an intrinsic materials property of semiconductors. The equation implies that light intensity is attenuated exponentially inside the semiconductor. The microscopic origin of photon absorption, described with a Fermi's Golden rule,[1] involves promotion of electrons from VB to conduction band. Thus, α is an energy dependent parameter.[1]

Radiative Recombination

Recombination refers to loss of mobile electrons or holes in the semiconductor. Some recombination processes are unavoidable such as radiative recombination and Auger recombination, other processes may be avoided such as trap-mediated recombination.

Radiative recombination involves electrons encountering holes and thus its rate, similar to the rate of chemical reaction, is proportional to density of electrons and holes:

$$U_{rad} = B_{rad}(np - n_i^2) \tag{1.15}$$

where B_{rad} [cm^3 s^{-1}] is the radiative recombination coefficient independent of charge density. More accurately, radiative recombination rate U_{rad} is determined by the density of excess (in case of solar cell, photogenerated) charge carriers, as such in solar cell operation radiative recombination scales non-linearly with light intensity and causes severe charge extraction loss when solar cells operate at elevated light intensities.[8] In case of a doped semiconductor, majority carrier density is regarded as invariant thus U_{rad} is determined by excess minority carrier density:[1]

$$U_{rad} = B_{rad} \Delta n N_a$$

or

$$U_{rad} = B_{rad} \Delta p N_d \tag{1.16}$$

In such case radiative recombination rate is proportional to the density of excess minority carrier, *i.e.* excess electrons in p-type semiconductor or excess holes in n-type semiconductor. The recombination kinetics also takes the form of pseudo first-order as N_a or N_d is typically much greater than Δn or Δp. This can be observed in photoluminescence (PL) decay spectra under very weak excitation, where the decay dynamics takes the form of mono-exponential.[9]

Non-Radiative Recombination

Auger recombination involves an electron and two holes or a hole and two electrons. The energy released by recombination is taken by the third entity and is ultimately lost as heat. Thus Auger recombination is non-radiative. The Auger recombination rate is proportional to the density of all three carriers, thus occurs when carrier densities are high (typically above solar irradiance and charge density > 10^{17} cm^{-3}).[10]

Shockley-Read-Hall (SRH) recombination involves with defects or intra-gap trap states and is non-radiative. The excessive energy that converts to photon emission is now transferred to photon, *i.e.* vibration of lattice.[11] Typically, one type of free carrier is captured by the localised trap states and recombine with the opposite carrier, alternatively a recombination centre can capture both types of carriers. Importantly, when a free carrier is captured by a localised trap state, the carrier can subsequently be released (de-trapping) or recombine with an opposite carrier before it is released – presence of trap states does not necessarily lead to non-radiative recombination, it also depends on availability of opposite charge carrier. SRH recombination rate can be expressed by considering a density of trap states N_t, and the probability that the trap is occupied f_t:[1]

$$U_{nr} = B_{nr} n N_t (1 - f_t) \tag{1.17}$$

Where U_{nr} is the non-radiative recombination rate, B_{nr} the non-radiative recombination coefficient. The SRH recombination coefficient B_n is proportional to the mean thermal velocity of the electron and the capture cross section of the trap for electrons.

Equation 1.18 is key to understanding charge carrier dynamics in photoluminescence spectroscopic measurements. The f_t is a quantity depending on density of photoexcited charge, as both our study[9] and literature studies[12,13] showed that trap-mediated recombination is more significant as excitation density reduces where f_t is higher. This will be further discussed in chapter 2.

Surface recombination is critical as in real materials trap states are preferentially located at the surfaces, or at the interfaces between crystalline domains interfaces in heterostructures. The density of trap states is considered in two dimensions as at the surface rather than in three dimensions as in the bulk, thus the relevant quantity would be recombination flux. A surface recombination velocity [cm s^{-1}], instead of recombination rate [s^{-1}], is defined as:

$$S = \mathrm{B} N_s \tag{1.18}$$

where N_s is surface charge density [cm^{-2}] and B [cm^3 s^{-1}] surface recombination constant.

Trapping versus De-trapping

Presence of trap states in semiconductors does not necessarily lead to trap-mediated recombination. The charge carrier captured by trap states may be released or may recombine non-radiatively with the opposite charge carrier depending on the time of release

$$\tau_{release} = \frac{1}{B_n n_i \exp\,(\frac{E_t - E_i}{K_{\boldsymbol{B}}T})} \qquad (1.19)$$

and

$$\tau_{capture} = \frac{1}{B_p p} \qquad (1.20)$$

where E_t is the energy depth of trap states, $\tau_{release}$ the release time of trapped electrons and $\tau_{capture}$ the time of electrons being captured by trap states. When electron release is faster than capturing a hole the trap states can be considered as an electron trap instead of a recombination centre, which slow down electron transfer but do not annihilate electrons. This occurs when the trap state is energetically shallow, or hole density is low. It is argued that the metal halide perovskites show excellent tolerance to defects, which enables these materials to be solution-processed, is ascribed to the dominant electronic defects being energetically shallow.[14,15]

Simplified Rate Equation

With above consideration the recombination of charge carriers in a semiconductor can be summarized with a simplified rate equation widely used in literature[10,16]

$$-\frac{dn}{dt} = k_1 n + k_1 n^2 + k_1 n^3 \qquad (1.21)$$

where n is density of electron, k_1, k_2 and k_3 are the first-order, second-order and third-order recombination rate constant, respectively. The assumption behind this simplified equation is that the intrinsic charge densities (n_i) and doping densities (N_a or N_d) of the semiconductor are minor compared to typical steady-state charge carrier density under illumination, approximately $10^{14} – 10^{16}$ cm^{-3}. If the recombination is first-order the rate constant can then be determined from fitting the resulting mono-exponential decay, whilst usually the recombination kinetics no longer follow mono-exponential at higher charge densities.

1.1.3. Junctions

In an attempt to achieve photovoltaic energy conversion electrons and holes must be driven in opposite directions. Separation of electrons and holes requires some sort of driving force built into photovoltaic devices, which can be realised by a junction formed between two electronically different materials, where the electrostatic force between the two materials provide the essential driving force.

The electric field that exists at equilibrium condition is called "built-in" field. It is typically established at the interfaces between two materials of different work functions. Alternatively, it is created due to the difference in electron affinity, band gap or effective band density of sates. An electric field is always effective in charge separation at it drives electrons and holes to the opposite directions. Gradients in charge carrier density, on the other hand, can be created by difference in their generation or removal rate. It typically occurs in an asymmetric environmental where electrons or holes are selectively removed, for example, due to a contact or a charged region that has low resistance for electrons but high resistance for holes.

The work function (WF) of a material is the potential required to remove an least tightly bond electron, defined as the difference between Fermi energy and vacuum energy[17]

$$\emptyset = E_{vac} - E_F \tag{1.22}$$

where E_{vac} is vacuum energy level. The work function of a metal is equal to the electron affinity, whereas in semiconductors it is controlled by doping. As a junction forms between two contacted materials, the electrostatic potential energy difference across the junction interface is determined by the difference of work functions.

A junction can be formed between two materials with different WF (called "heterojunction"), or between two regions of the same materials with different doping levels (called "homojunction"). The electric field *(F)* formed across the junction is determined by WF difference

$$q\int_{-x}^{x} F\,dx = \Delta\emptyset \qquad (1.23)$$

Metal-Semiconductor Junction

A junction can be formed when a metal and a semiconductor are brought into electronic contact – this occurs at charge transport layer/electrode interfaces in perovskite solar cells. As their Fermi levels must line up it causes a shift of the vacuum level between the metal and the semiconductor, creating a variation of electrostatic potential energy at the interface. This is achieved by exchange of charge carriers between the two materials, until a gradient of charge density is established to prevent further diffusion.

Because metals are much poorer at storing charge, virtually all net charges reside in the semiconductor and the potential difference drops in the semiconductor, too. The region where the material carries net charges and E_{vac} drops is called space charge region or space charge layer. However, the net charge acquired in this region is due mainly to fixed ionized atoms, such that space charge region is regarded as depletion of carriers and is also called as a depletion region. As the energetics of conduction band and valence band in a semiconductor must stay parallel with E_{vac}, the band edges bend within the space change region. The magnitude of band bending is determined by qV_{bi} where V_{bi} is the built-in bias.

By joining an n-type semiconductor to a metal with higher work function, an electric field is established that drives electrons to the semiconductor side and holes to the metal side (**Figure 1.2 a**). From semiconductor to metal such a contact presents a lower resistance for holes than electrons, which is a typical example of Schottky barrier. It is obvious that the junction exemplified above exhibit an asymmetric current-voltage behaviour, that the junction allows current flow only in forward direction. Such

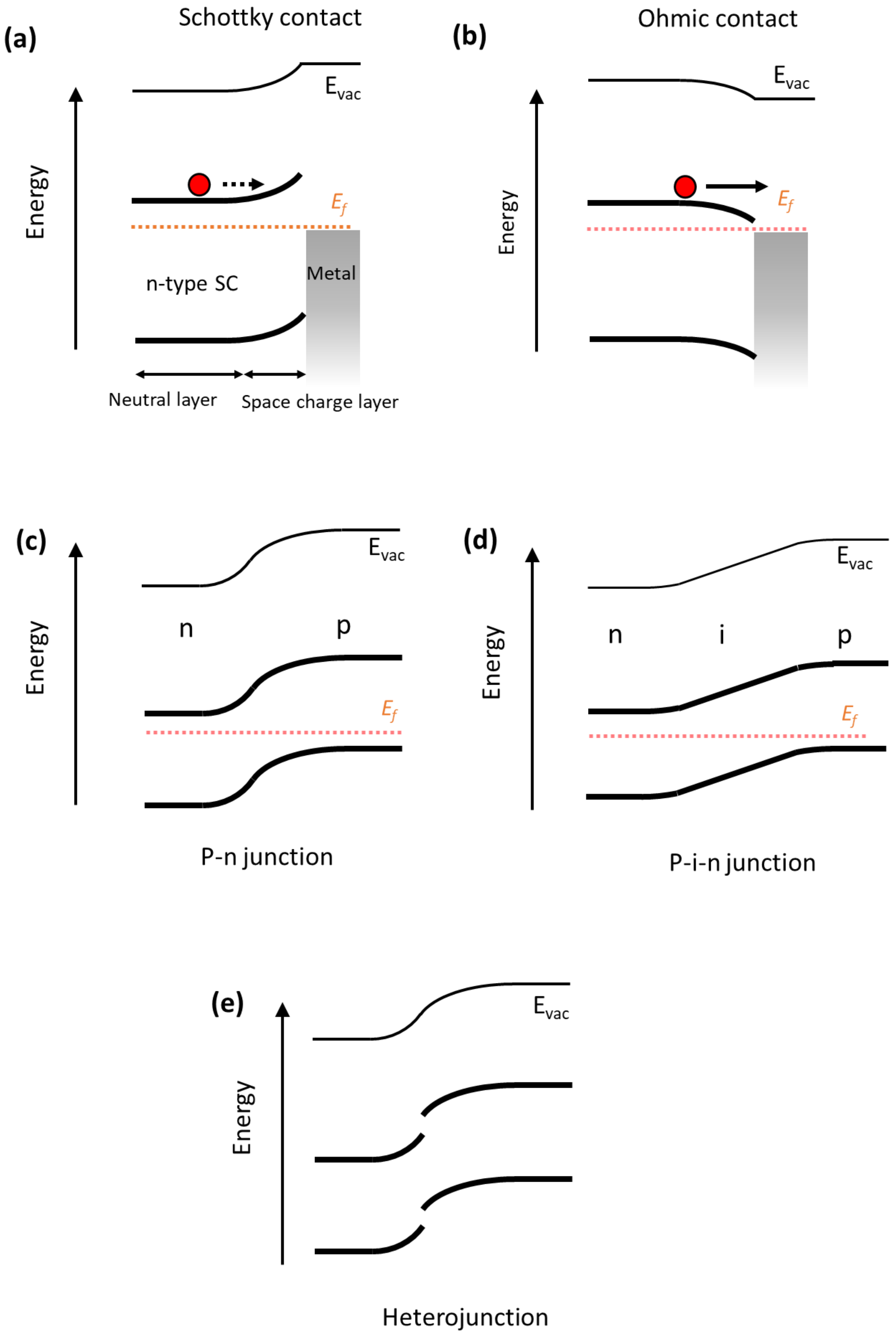

Figure 1.2 Band diagram of metal-semiconductor interface forming **(a)** a Schottky contact and **(b)** an Ohmic contact. Semiconductor- semiconductor interface forming **(c)** a p-n junction, **(d)** a p-i-n junction and **(e)** a heterojunction.

asymmetric behaviour is a feature of most of the photovoltaic devices.

A different scenario to be considered is that an n-type semiconductor is electrically contacted with a metal of lower work function (**Figure 1.2 b**). In this case there is a downward band bending in the semiconductor that encourage majority carrier passing through the junction. This is typically called Ohmic contact, where the resistance for majority carrier is low and the current can pass easily in either direction. The photovoltage under illumination is negligible in this junction. The formation of an Ohmic contact at electron transport layer (ETL)/metal is essential for efficient charge extraction and prevent "S-shape" in J-V curve, as such an interfacial dipole layer is used between our ETL/metal interface to effectively reduce WF of metal and convert Schottky contact into Ohmic contact.

Semiconductor-Semiconductor Junction

The p-n junction is a typical semiconductor-semiconductor junction and the classical model of a photovoltaic device (**Figure 1.2 c**). It consists of an interface between an n type region and a p type region of the same material. An electric field is established at the interface driving electrons to the n-side and holes to the p-side. The junction is depleted of both carriers and provide a barrier to the majority carriers from both sides.

A p-i-n junction can be formed by sandwiching an intrinsic semiconductor with an n-type semiconductor and a p-type semiconductor (**Figure 1.2 d**). The p-i-n model is important as it is most resembles the structure of perovskite solar cells. Similar with a p-n junction, the built-in potential is determined by the work function difference between the n-type and p-type semiconductors, except that the electrostatic potential difference drops across a wider region in the intrinsic layer, so is the extension of electric field. The design of p-i-n junction is preferred if the lifetimes of both majority carriers in the doped layers are short, in such case photocurrent is contributed by charge carriers excited from the intrinsic layer that are driven to different contacts by the electric field.

The p-n or p-i-n junction can be alternatively presented as a heterojunction if different materials are used (**Figure 1.2 e**). In such case there could be a discontinuity of band edge at the junction interfaces due to the change of material energetics. Although the step in electrostatic potential change at the interfaces usually assist charge separation, it also enhances charge recombination at the interfacial regions.

As most organic semiconductors are amorphous and thus intra molecular force dominates, light absorption generates tightly bound electron-hole pairs (called exciton) that only dissociate at a junction interface.[18] However, the excitons can only diffuse a few tens of nm before they recombine, thus distributed interface is used by blending two materials on a scale similar to exciton diffusion length. By using this bulk heterojunction design charge separation can be effectively achieved throughout a layer of optical absorption.

1.1.4. p-n Junction

At Equilibrium

The built-in bias, V_{bi}, in a p-n junction at equilibrium is determined by the work function difference between the n layer and the p layer. Using equation 1.5 and 1.6 the work function of a semiconductor can be correlated to the doping density, and thus V_{bi} [V] can be expressed as

$$V_{bi} = \frac{K_B T}{q} \ln \left(\frac{N_d N_a}{n_i^2}\right) \tag{1.24}$$

This equation highlights that a stronger electrical field can be formed between two semiconductors with higher doping level. We assume in the junction region is completely free of majority carriers for a depth of w_p in the p layer and w_n in the n layer, and the depleted layer is charged of immobile ions. The change of electrostatic potential in this region is related to permittivity and concentration of dopants, which can be described by Poisson's equation:

$$\frac{d^2\emptyset}{dx^2} = \frac{q}{\varepsilon_s}N \tag{1.25}$$

where $\emptyset$ is potential [V], N is doping density [cm^{-3}] in either p or n side of the junction and ε_s is permittivity of the semiconductor [F m^{-1}]. Poisson's equation suggests that electric field across the depletion region is determined by gradient of electrostatic potential, while gradient of electric field is determined by density of immobile charge.

Using equation (1.25) we can then qualitatively describe the variation of junction parameters: i) the depletion width in the junction increases with reduced doping of either p payer or n layer; ii) division of V_{bi} drop is inversely related doping level: most of the potential drops in the layer with lower doping density resulting in larger depletion width – this is a key factor to be considered at the interfaces of perovskite/charge transport layer, whereas more complex scenarios of electrostatic potential variation are seen when mobile ions considered in perovskite films.[7,19]

Under Bias

Similar to the scenario in the Schottky junction, a positive bias applied to the n-side reduces V_{bi} and the barrier height allowing for majority carriers to diffuse across the junction, resulting in a net current. In addition to this majority carrier injection, the quasi Fermi levels in the junction are split by applied bias, giving rise to recombination in that region that adds to the net current.

The dark current J_{dark} include a minority carrier diffusion current, a recombination current in depletion region and a radiative recombination current J_{rad} that can be significant in direct band gap semiconductor. J_{dark} can be expressed as

$$J_{dark} = J_0[\exp\left(\frac{\mathrm{qV}}{mK_BT}\right) - 1] \qquad (1.26)$$

where J_0 is a constant and m is the ideality factor depending on the dominant recombination mechanism. m = 1 if the semiconductor has direct band gap with relatively long carrier diffusion length, recombination occurs mainly in the bulk layer, m = 2 if recombination within the depleted region dominates.[1]

1.2 Working Principle of Photovoltaic Devices

Solar cells convert solar energy to electrical energy. In this section we focus on the nature of solar irradiance and the general physical parameters of a working solar cell and compares the designs of major types of solar cells developed in recent years.

1.2.1. Solar Irradiance

The sun emits light with a range of wavelengths from ultraviolet to infrared region of the electromagnetic spectrum. Spectral solar irradiance, F [W m^{-2} μm^{-1}], describes the amount of energy received from the sun per unit area and per unit time as a function of wavelength, which can be expressed as[1]

$$F(\lambda) = \frac{\phi E}{\Delta\lambda} \qquad (1.27)$$

where ϕ is photon flux and E is photon energy.

The extra-terrestrial spectrum of solar irradiance, *i.e.* the spectrum just outside the Earth's atmosphere, is similar to the spectrum of a *black body* at 5760 K. The irradiance is greatest at visible-wavelength range peaking between the blue and green.[20] On passing through the Earth's atmosphere, the irradiance is attenuated and the spectrum

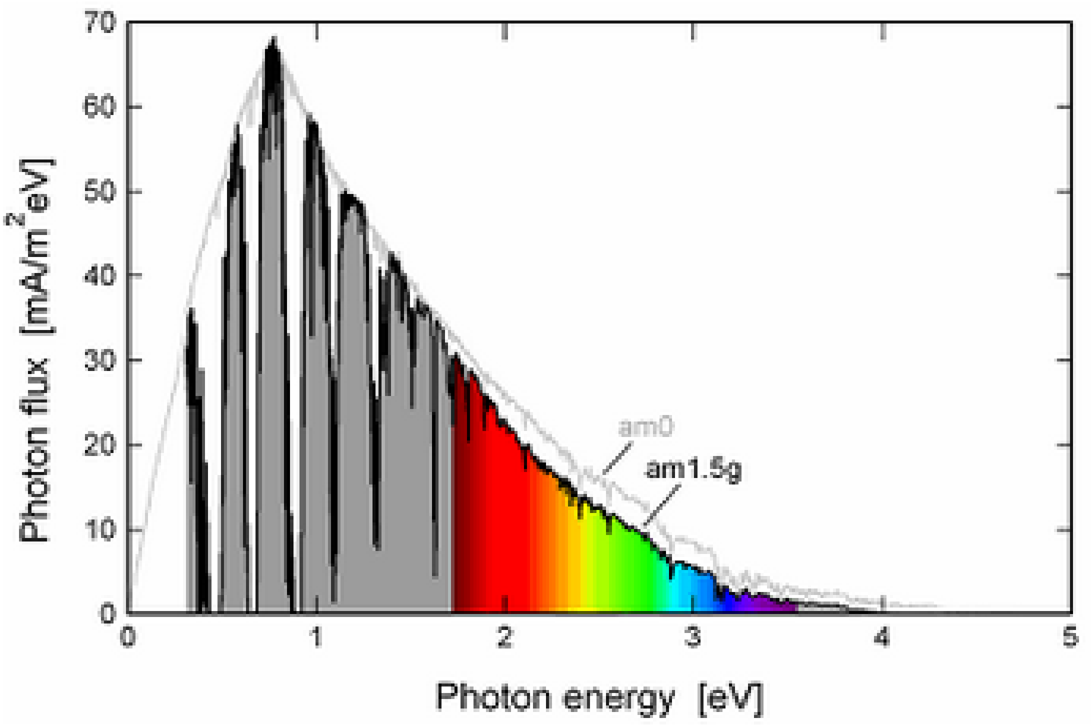

Figure 1.3 Extra-terrestrial (AM 0) and standard terrestrial (AM 1.5) solar spectrum. (https://www2.pvlighthouse.com.au/)

shape is changed. Attenuation by the atmosphere is quantified by the "Air Mass" factor. The standard spectrum for temperature latitudes is *Air Mass 1.5* or AM1.5. For convenience, the terrestrial solar spectrum is defined as AM 1.5 spectra with integrated irradiance of 1000 W m^{-2}.[21] The solar spectrum of AM 0 and AM 1.5 are shown in **Figure 1.3**.

The actual irradiance, however, varies depending on seasonal or daily variation in the position of the sun and on variation of the weather.[22,23] The average solar irradiance varies from less than 100 W m^{-2} in high-latitude areas to over 300 W m^{-2} in the sunniest areas. In addition, diffuse light owing to scattering by the atmosphere presents challenges for photovoltaic energy conversion in cloudy weather.[24]

1.2.2. Solar Cell Parameters

A solar cell converts solar energy to electrical energy. This process is fundamentally built upon The Photoelectric Effect explained by Einstein in 1905. However, instead of waiting for the excited electrons to relax to ground states, the solar cell needs to have some asymmetry to drive the photogenerated charge carriers. This is usually achieved with a p-n junction or a heterojunction that creates an electrical field, or potential difference, to drive charge carriers to external circuit.[1]

The behaviour of most of the solar cells in the dark resembles a diode, exhibiting a "rectifying behaviour" that admits current flow only under forward bias (V > 0). For an ideal solar cell, this forms the dark current given by

$$J_{dark} = J_0\,[\exp\left(\frac{qV}{mkT}\right) - 1] \tag{1.28}$$

where J_0 is the saturation current that approximately equals to the J_{dark} under high reverse bias (V << 0), *k* is Boltzmann's constant and *T* is temperature in degrees Kelvin.

The photocurrent generated under illumination at short circuit, J_{SC}, depends on the incident light flux density and the quantum efficiency (QE) of the solar. The overall current-voltage characteristics of a solar cell is approximated as the superimposing of J_{SC} and J_{dark}

$$J_{ph} = J_{SC} - J_{dark} \tag{1.29}$$

which becomes

$$J_{ph} = J_{SC} - J_0\,[\exp\left(\frac{qV}{mkT}\right) - 1] \tag{1.30}$$

at a certain applied voltage the J_{ph} becomes zero, corresponding to the open circuit condition and the maximum potential can be achieved in the solar cell, open circuit voltage V_{OC}

$$V_{OC} = \frac{kT}{q} \ln\left(\frac{J_{SC}}{J_0} + 1\right) \qquad 1.31$$

As in ideal solar cell J_{SC} scales linearity with light intensity, the V_{OC} of a solar cell increases logarithmically with light intensity.

Figure 1.4 shows the current-voltage (J-V) characteristics of a typical perovskite solar cell, where J_{SC} and V_{OC} are marked. The solar cell operates under forward bias between 0 and V_{OC}, where the cell outputs power density of P = JV plot on the figure. At the cell's maximum power point (MPP) *P* reaches maximum, corresponding to a V_{max} and J_{max}, and a fill factor (FF) is defined as

$$FF = \frac{J_{max} V_{max}}{J_{SC} V_{OC}} \qquad 1.32$$

which describes the "squareness" of the J-V curve. The power conversion efficiency, η,

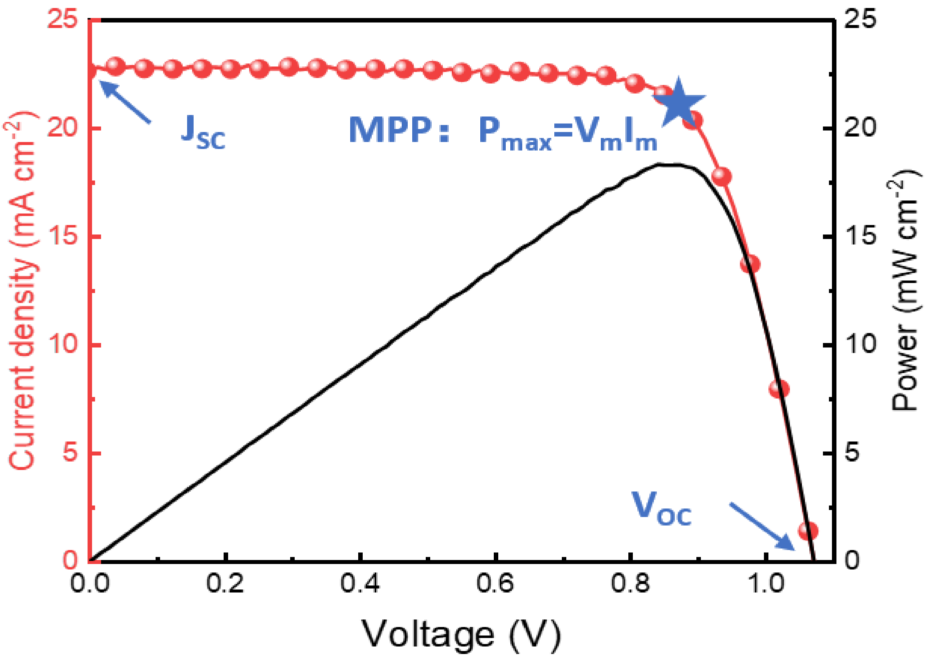

Figure 1.4 Typical current-voltage (J-V) curve (red symbolled line) of a perovskite solar cell and the corresponding power output (black solid line). The J_{SC}, V_{OC} and maximum power point (MPP) are indicated.

can be calculated as

$$\eta = \frac{J_{SC} V_{OC} FF}{P_{in}} \quad 1.33$$

where P_{in} is the incident light power density. The light intensity under Standard Test Condition (STC) with AM1.5 spectrum is 1000 W m^{-2}, although in real-word condition the illumination intensity can be far less than 1000 W m^{-2}.[25] The J_{SC}, V_{OC} and FF are key parameters determining η of a solar cell. The J_{SC} and V_{OC} are determined by the E_g the semiconductor but in contracting trend: normally a wider band-gap semiconductor yields higher V_{OC} but lower J_{SC}, as increased band-gap energy leads to higher potential energy of charge carrier but narrower absorption spectrum. The highest efficiency can be achieved in a single-junction solar cell as given by the Shockley–Queisser limit,[26] which shows the theoretical limit of η as a function of E_g. It is suggested that in the optimum E_g between 1 eV to 1.5 eV.

1.2.3. Designs of Solar Cells

Monocrystalline Solar Cells

Monocrystalline silicon solar cells are typically based on a p-n junction, consisting of a thick (300 – 500 μm), lightly doped ($N_a \sim 10^{16}$ cm^{-3}) p-type layer and a thin (0.2 – 0.3 μm), heavily doped ($N_d \sim 10^{19}$ cm^{-3}) n-type layer.[1] The junction is formed by diffusion of n-type dopant onto the p-type wafer. **Figure 1.5 a** shows the energy band diagram of a p-n junction in a monocrystalline Si solar cell. The p-type layer needs to be thick as light absorption is poor for Si as an indirect semiconductor, as such light penetration is deep into p-type layer and recombination in the p-type region is the most important process. In addition, a heavily doped, back contact is formed to drive electrons away from the rear surface. The PCE single-junction Si solar cell is reaching theoretical maximum of 29% and the key change is to reduce the production cost.[27]

Some III – V semiconductors such as gallium arsenide (GaAs) has direct band gap with suitable band-gap energy shows more effective photon absorption than Si. The design of GaAs solar cell is similar with that of Si solar cell, **Figure 1.5 b**, comprising a heavily doped (usually p-type) emitter and a lightly doped but much thinner n-type base (2 – 4 μm). Doping of GaAs is achieved through replacing atoms with different valence, such as Al, Si. Owing to stronger photon absorption the recombination at front surface becomes dominant, thus similar to the design in Si solar cell a heavily doped or a high-band-gap layer is formed at front surface to mitigate surface recombination.[28]

GaAs solar cells suffer stronger SRH recombination in space charge region owing to high density of both electrons and holes than the Si solar cells where most photogeneration takes place in the neutral p-type layer. As such the ideality factor m derived from dark current is greater than 1. This, to some extent, might be similar in perovskite solar cells where the halide perovskite film also exhibit strong absorption coefficient greater than 10^4 cm^{-1}.[28,29]

Inorganic Thin-film Solar Cells

Thin-film solar cells are based on polycrystalline or amorphous materials manufactured with lower cost than monocrystalline materials.[30] A well-developed material is amorphous silicon (a-Si),[31] other materials are direct band gap semiconductors with high optical absorption including cadmium telluride (CdTe)[32] and copper indium gallium diselenide ($CuInGaSe_2$).[33] Owing to intrinsic defects, charge diffusion length is shorter in these polycrystalline or amorphous materials such that the thickness of active layer is limited as well as that these materials are difficult to dope.[31]

The design of a a-Si solar cell is a p-i-n heterojunction, a structure very similar to perovskite solar cells used in this study. In **Figure 1.5 c** a schematic drawing of band profile is shown, where electrical field drop across the intrinsic region. Owing to charged defects the electric field is screened thus i-region becomes neutral – this emerges as a prominent issue in perovskite solar cells as well due to considerable intrinsic defects associated with these solution-processed thin films. It is worth noting that without charge defects high charge density can also minimise electrostatic potential in the i-region.[31]

Both $CuInGaSe_2$ and CdTe are direct band gap semiconductors and can be doped into n- or p-type.[30] The design of solar cells is a p-type CuInGaSe or CdTe layer deposited onto transparent conductive oxides (TCO), on top of which an n-type CdS is deposited and a zinc oxide (ZnO) layer as anti-reflection layer.

Dye-sensitized and Organic Solar Cells

Dye-sensitized solar cells (DSSCs) and organic solar cells (OSCs) are both based on photo-absorption by molecular materials while charge separation takes places at the interface of a different charge accepting material. Compared to inorganic semiconductors the fabrication cost of these molecular materials is readily reduced.

The structure of DSSCs, schematically drawn in **Figure 1.5 d**, is based on a mesoporous titanium dioxide (TiO_2) film composed of nanocrystalline TiO_2 with a monolayer of photoactive dye molecules attached to surface.[34] Photoexcited electrons are injected into the CB of TiO_2 while remaining holes are extracted to counter electrode by electrolyte containing iodide/triiodide redox system. The voltage generated corresponds to difference of Fermi level between electrons in TiO_2 and redox potential of the electrolyte.[35]

The active layer of organic solar cells typically adopts a bulk heterojunction (BHJ) structure comprising a photo-absorbing material (donor) blended in nanoscale with a charge accepting material (acceptor), **Figure 1.5 e**.[36] Typical size of donor or acceptor domains in the blending is no greater than 20 nm, as such bonded electro-hole pairs

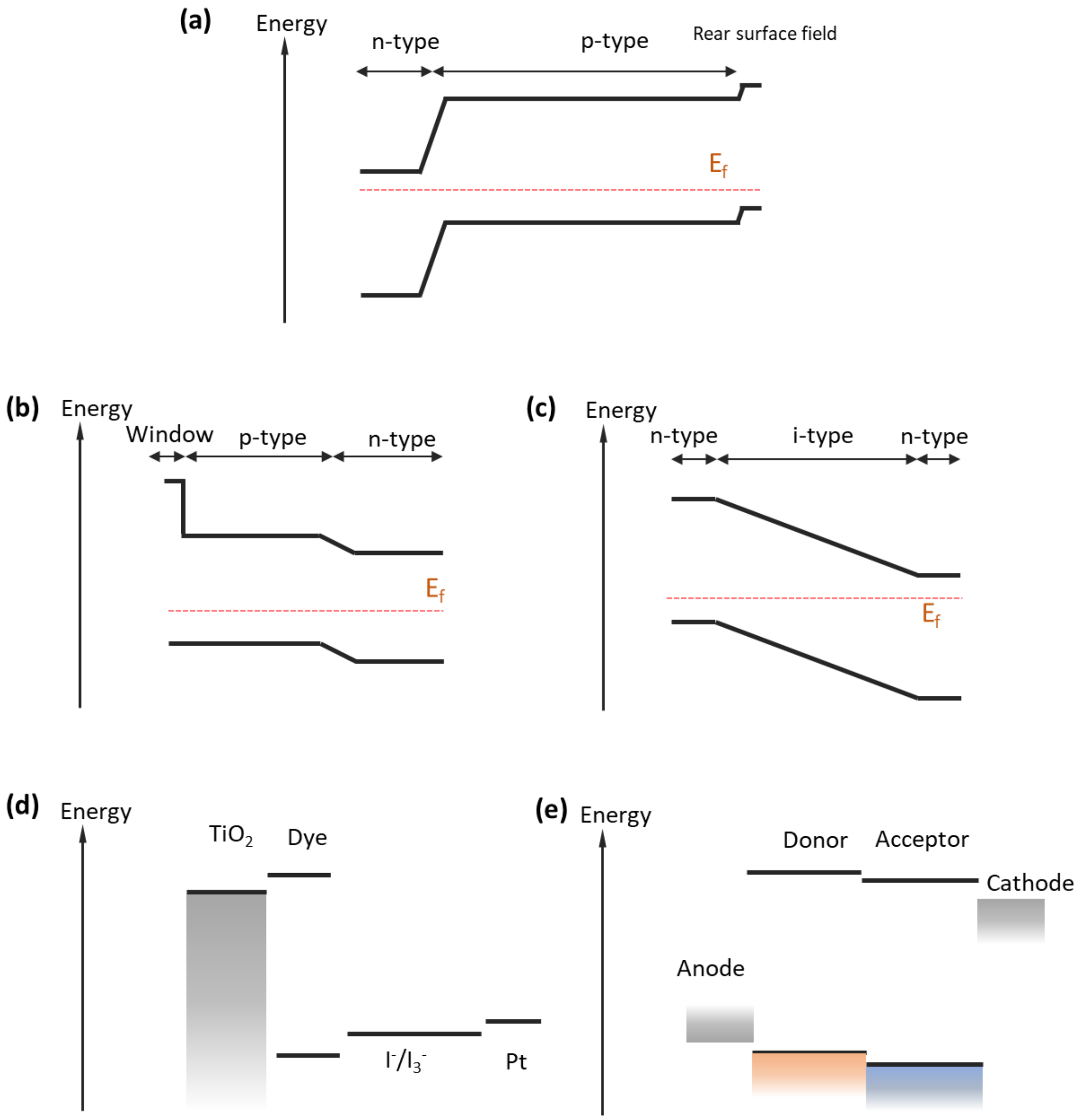

Figure 1.5 Schematic drawing of band profile of **(a)** monocrystalline Si solar cell, **(b)** monocrystalline GaAs solar cell, **(c)** polycrystalline Si solar cell, **(d)** dye-sensitized solar cell and **(e)** organic solar cell.

(excitons) generated in donor diffuse to and dissociate at donor/acceptor interfaces. Such process is essential to generating free charge carriers in organic solar cell but inevitably causes potential energy loss. The V_{OC} of OSCs is limited by the HOMO (highest occupied molecular orbital) level of donor and LUMO (lowest unoccupied

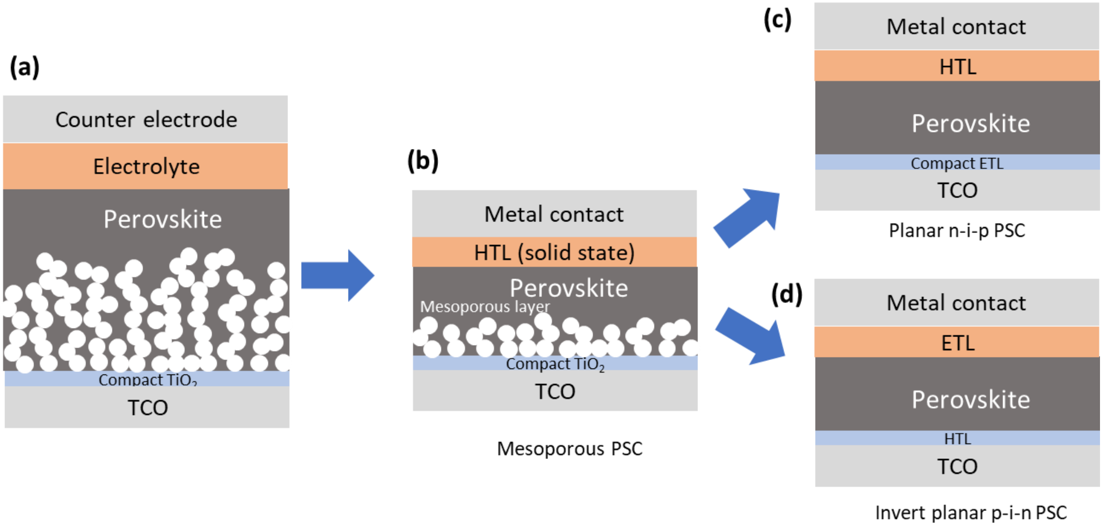

Figure 1.6 Schematic drawing of structure evolution of perovskite solar cell (PSC). **(a)** "perovskite-sensitized" solar cell, **(b)** mesoporous PSC, **(c)** planar n-i-p PSC and **(d)** invert planar p-i-n PSC.

molecular orbital) level of acceptor.[37]

Organic solar cells are widely studied in parallel with perovskite solar cells while these two devices exhibit rather different operational mechanisms in that free charges are generated upon photoexcitation in perovskite with no need for an accepting material. This gives rise to dominance of radiative recombination in perovskite solar cells in contrast to dominance of non-radiative recombination in organic solar cells.[38]

1.2.4. Evolution of Perovskite Solar Cells

In the first attempt to employ metal halide perovskite as photoactive layer in 2009,[39] the device architecture then was basically adopted from dye-sensitized solar cells, *i.e.* with a 6-μm mesoporous TiO_2 layer and liquid electrolyte, and achieved power conversion efficiency (PCE) of 3.8%.[39] It was two years later the same device architecture but with a much thinner TiO_2 were used and PCE of 6.5% was achieved.[40] The PCE was boosted to 9.7% in 2012 by using solid-state hole conductor.[41] From then on perovskite-based solar cells have been intensively investigated and PCE kept roaring up to 19.6% in 2014,[42] and to 23.7% recently.[43]

In parallel to boosting of efficiency the device structure has also evolved. Mesoporous TiO_2 was replaced by insulating Al_2O_3 scaffold[44] and was later removed to form a purely planar structure (**Figure 1.6 c**),[45] with the realisation that the perovskite layer can simultaneously transport charge besides charge generation. The inverted planar structure (**Figure 1.6 d**), adopted from organic solar cells, was then attractive due to of its compatibility with low-temperature processing and negligible current density-voltage (J-V) hysteresis.[46] These devices normally use polymers as hole transport materials and fullerene derivatives as electron transport materials. The relative ease of processability enables these device to be potentially compatible in tandem solar cells.[47]

1.3 Crystallography and chemistry of Perovskite

1.3.1. Crystal Structure

The term "perovskite" refers to a family of materials with the same crystal structure as calcium titanite ($CaTiO_3$).[48] These compounds shared the chemical formula ABX_3, where "X" is an anion and "A" and "B" are cations of different sizes.[49] The crystal structure of a typical ABX_3 perovskite is shown in **Figure 1.7 a**: "A" cation resides at the eight corners of the cubic lattice. The body centre of each face is occupied by an anion "X", forming an octahedron structure. The centre of this latter is occupied by the smaller cation "B".

The possibility of the atoms or ions to assemble ABX_3 perovskite structure depends on the Goldsmidt tolerance factor t:[50]

$$t = \frac{R_X + R_A}{\sqrt{2}(R_X + R_B)} \tag{1.34}$$

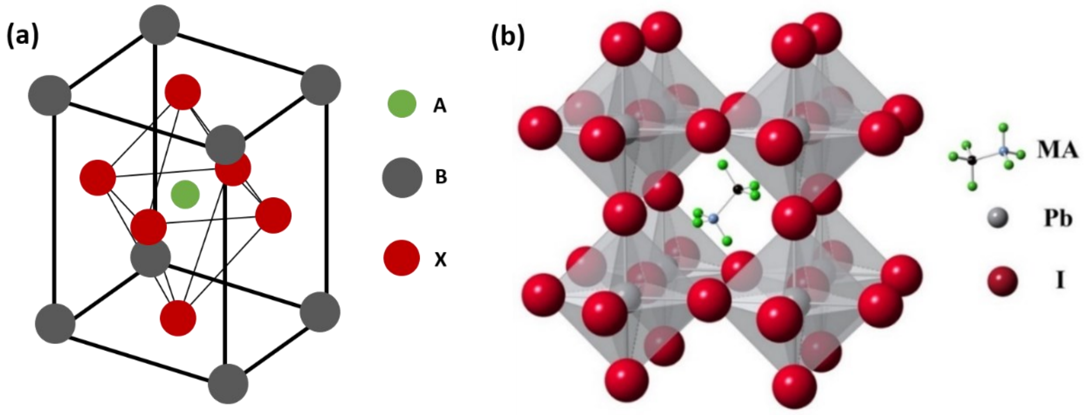

Figure 1.7 (a) Crystal structure of ABX_3 perovskite materials. **(b)** Crystal structure of $CH_3NH_3PbI_3$ perovskite.

where R_X, R_A and R_B are the radius of “X”, “A” and “B”, respectively. A cubic structure can be formed only if $0.9<t<1$. Otherwise low symmetry is formed such as tetragonal, rhombohedral or hexagonal structures.

The organic-inorganic halide perovskites (OHP) initially refers to methylammonium lead halide perovskite ($CH_3NH_3PbX_3$, X=I, Br, Cl or their mixture), although later different cations, such as formamidine (FA), caesium (Cs), rubidium (Rb),[51] or different metal cations, such as Tin were incorporated.[3] **Figure 1.7 b** shows a schematic drawing crystal structure of methylammonium lead tri-iodide perovskite ($CH_3NH_3PbI_3$), one of the most widely used materials among the OHP family.

Most of the perovskite crystals undergo a phase transition upon temperature variation,[52] which, for example, has be studied with calorimetric and infrared spectroscopy for $CH_3NH_3PbI_3$ perovskite.[53] The $CH_3NH_3PbI_3$ remains in tetragonal phase at room temperature, transformed to cubic phase with higher symmetry when $T > 330$ K or to orthorhombic phase as $T < 161$ K. In comparison both $CH_3NH_3PbBr_3$ and $CH_3NH_3PbCl_3$ are cubic at room temperature.[54] The crystal structure is examined by X-ray diffraction, which will be discussed in details in the experimental chapter. The cubic $CH_3NH_3PbI_3$ comprises a body-cantered unit cell with CH_3NH_3 in the centre with (100) planes giving the strongest x-ray diffraction, while tetragonal $CH_3NH_3PbI_3$ has a more complex unit cell with Pb in the centre and (110) planes showing the strongest x-ray diffraction.[55] It is worth noting that phase transition of $CH_3NH_3PbI_3$ during thermal annealing (typically at 100° C or above) and subsequent cooling may be an important cause of defects in the film.

Table 1.1 Phase transition temperature of $CH_3NH_3PbX_3$ perovskite.[54]

Perovskite structure	Orthorhombic	Tetragonal	Cubit
$CH_3NH_3PbI_3$	< 171.5 K	171.5 – 330.4 K	> 330.4 K
$CH_3NH_3PbBr_3$	< 148.8 K	148.8 – 154.0 K	> 154.0 K
$CH_3NH_3PbCl_3$	< 171.5 K	171.5 – 177.2 K	> 177.2 K

1.3.2. Electronic & optical properties

The superior optoelectronic properties of lead halide perovskite stems from the long pair of *s* electrons in Pb cations.[56] Taking $CH_3NH_3PbI_3$ for example, the valence band maximum (VBM) shows strong Pb s and I p antibonding character, whereas the conduction band minimum (CBM) is contributed from Pb p state.[57,58] The organic molecules generate states far from the band edge and thus contribute little in determining the basic electronic structure of the perovskite, whereas they mainly help stabilize the perovskite structure.[56] The electronic structure of lead halide perovskite is inverted to those conventional semiconductor, such as gallium arsenide (GaAs) and cadmium telluride (CdTe) where the CBM is made up of s-orbitals and the VBM p-orbitals.[51]

One impact of the unique electronic structure of lead halide perovskites is their ambipolar conductivity.[59] In some conventional semiconductors, effective mass of electrons is much smaller than the hole effective mass and the electrons transport much faster that the holes the lowest conduction band (CB) is more dispersive than the highest valence band (VB), because the high-energy s orbitals that construct the CB are more dispersive than the low-energy p-orbitals that construct the VB. As a result, the. Owing to the strong s-p coupling, the upper VB of $CH_3NH_3PbI_3$ is as dispersive as the lower CB made up by p-orbitals, resulting in balanced effective mass of electrons and holes.[60]

The other impact of the strong s-p coupling is their high optical absorption,[61] which is extremely important for thin-film absorbers. The optical absorption of semiconductor is fundamentally determined by a combined effect of i) transition matrix elements between valence band and conduction band, which measures the probability of each photoelectric transition, and ii) their joint density of states, which measures the total number of possible photoelectric transitions.[1,62] For silicon absorbers, their indirect bandgap remarkably reduces the transition probability between the band edges. The bandgap of $CH_3NH_3PbI_3$ is direct and thus its transition probability is much higher. Moreover, the density of states of in the lower CB of $CH_3NH_3PbI_3$ perovskite is much higher than that of second-generation absorber, such as GaAs, resulting in higher DOS.[57,58] Besides, the band-edge transition from VBM to CBM comes from the transition between mixed Pb s and I p-orbitals to Pb p-orbitals. The intra-atomic Pb s to Pb p transition has a high probability, which further enhances the VBM-CBM transition.[57]

1.3.3. Defects

Classification of Defects in Solids

While a large volume of literature correlated improvement of perovskite solar cell performance with passivation of defects, it is essential to review the general physics and chemistry of defects in perovskite. In general defects in solids are classified in dimensional hierarchy into zero-dimensional defects (point defects) and other higher dimensional defects (dislocations, surfaces, defect clusters, voids, precipitates, etc.).[63] The point defects in solids can be classified according to their elemental nature into intrinsic defects, which appear in pure materials, and extrinsic defects, which are caused by impurities. A vacancy is formed when an atom is missing from a lattice site that it should occupy (**Figure 1.8 b**), while an interstitial is creased when an atom is forced into a site that is not normally occupied (**Figure 1.8 c**). An anti-site is generated when an A-atom is on the site of a B-atom (**Figure 1.8 d**), or vice versa. A stoichiometric compound mainly contains two types of intrinsic point defects: i) Schottky defects, where a paired anion and cation vacancies are created (**Figure 1.8 e**), and ii) Frenkel

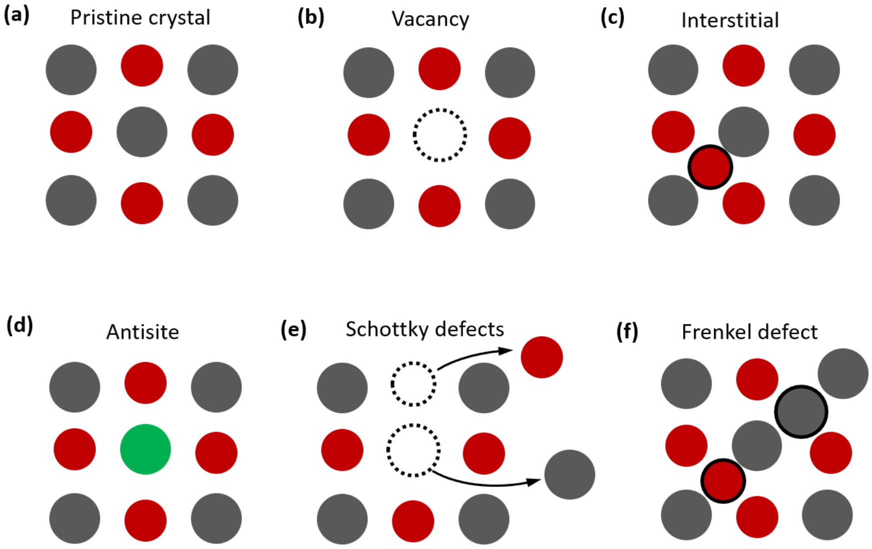

Figure 1.8 Schematic drawing of point defects in solids: **(a)** pristine crystal, **(b)** vacancy, **(c)** interstitial, **(d)** anti-site, **(e)** Schottky defect pair and **(f)** Frenkel defect

defects, a paired vacancy and interstitial. A non-stoichiometric compound might contain other point defects including anti-sites, substitutional impurities or interstitial impurities.[63] Moreover, a point defect is termed native defect when it presents as the crystal is grown. Otherwise it is termed induced defect if it is introduced by post-grown processing, such as annealing, irradiation, etc.

Point defects in semiconductors played a crucial role in determining their electronic and optical properties,[64] and thus have a profound impact on the power conversion efficiency of solar cells.[65] For instance, defects that generate shallow levels, *i.e.* those with energy levels close to respective band edge, can donate or accept electrons to bulk bands and become effective doping methods for the semiconductor, while the defects the create deep levels within the band gap can trap electrons or holes cause Shockley-Read-Hall recombination which is unfavourable to photovoltaic energy conversion.[1,64,66]

Point defects in Metal Halide Perovskites

First-principles calculations showed the superior point defect properties of the lead halide perovskites which is partially accounted for their excellent photovoltaic performance.[14] It is suggested that the dominant defects, *i.e.* with low formation energy, in $CH_3NH_3PbI_3$ are all energetically shallow defects,[14] which gives rise to higher probability of a trapped electrons or holes to be released into band edges. These defects include acceptor-like defects such as I interstitials (I_i), CH_3NH_3 (MA) vacancies (V_{MA}), Pb vacancies (V_{Pb}), as well as the donor-like defects such as MA interstitials (MA_i), I vacancies (V_I) and Pb interstitials (Pb_i).[14] These defects exhibit low transition energy of less than 50 meV, among which I interstitials show the lowest formation energy. However, the defects with high transition energy, *i.e.* energetically deep in the gap, have high formation energy and thus are less likely to exist in perovskite crystals. It is also shown that neither Schottky defects nor Frenkel defects pairs in $CH_3NH_3PbX_3$ generate deep gap states.[67] Considering the thermodynamic equilibrium growth condition of MAPI, there's certain chemical potential for each possible type of chemical defect to be formed. These chemical potential are probed as formation energy of each type of defect. Most likely formed defects are p-type V_{Pb} and n-type MA_i in $CH_3NH_3PbI_3$.[14]

Defect Migration

The migration of point defects, or ions in some description, has drawn broad attention due to its correlation with several important phenomenon including current-voltage hysteresis,[7] switching of photovoltaic behavior[68] and giant dielectric constant,[69] etc. As shown in **Figure 1.9 a**, theoretical calculation suggests the mobile ionic defects are mainly vacancy anions.[70] Photothermal induced resonance microscopy enables direct imaging of MA^+ distribution the perovskite films.[68] The accumulation of MA^+ at cathode after applying a small electrical field experimentally demonstrated the migration of MA^+ in perovskite films. Migration of I^- has been observed by X-ray photoemission spectroscopy (XPS) in a laterally configured perovskite device after applying long-term bias.[71] These findings experimentally confirmed the theoretical calculation of I^- and MA^+ migration in perovskite films, despite that the defect site through which these ions migrate is yet unclear.

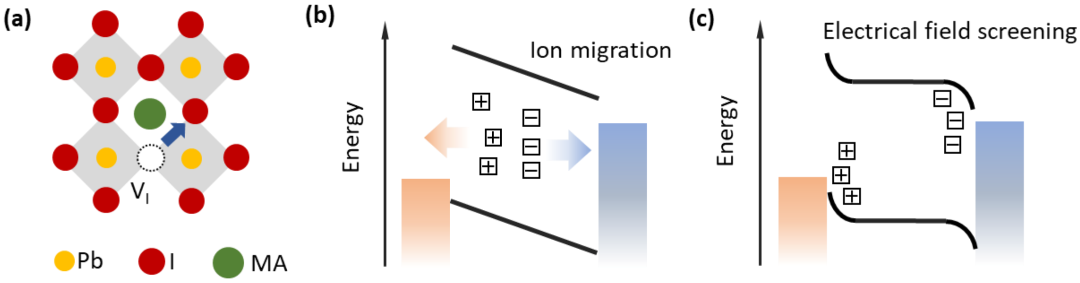

Figure 1.9 (a) Schematic drawing of iodine vacancy migration in perovskite crystal. **(b)** Schematic drawing of ion migration and **(c)** screening of build-in electrical field in a perovskite solar cell.

Migration of defects can be characterized with PL images of perovskite films between to in-plane electrodes with constant biased applied.[72,73] As these ionic defects introduce non-radiative electronic states, their migration results in quenching of local PL on the film. Films with high density of ionic defects show strongly quenched PL near one metal contact after a certain period of applying constant bias.

The activation energy for ionic migration can be derived from first-principle calculation and can be experimentally measured with kinetic data extracted from current-voltage response of a full PSC.[19] A significant consequence of ion migration is screening of built-in electrical field, shown by **Figure 1.9 b** and **1.9 c**. This gives rise to unique phenomenon in device transient measurement, such as invert photocurrent transient,[74] inverted photovoltage transient[7] and slow rise of photovoltaige.[75,76] Direct observation of fiend-screening is made by scanning kelvin probe microscopy on the cross-section of solar cell.[77]

The unusual J-V hysteresis phenomenon in perovskite solar cells[78] have been attributed to ion migration.[71,79,80] The experimentally determined activation energy of J-V hysteresis through temperature-depend photocurrent difference showed agreement of the activation energy of ion migrations.[81] One model of this process was proposed that ion drifting under applied bias forms interfacial energy barrier, leading to shift of work function of respective electrode as well as band bending depending on the direction of applied electrical field.[79] For example, applying reverse bias drives I^- to anode and causes additional upward bending of perovskite valence band which is favourable for charge extraction, while applying forward bias is vice versa. Alternatively, the process might involve a trapping and releasing ions at the perovskite/TiO2 interface upon a voltage change which causes the slow response of the measurement photocurrent, giving rise to the over-estimation or under-estimation of photocurrent.

2. Experimental Methods

In this chapter the experimental methodologies are introduced, starting from how we fabricate inverted-structure perovskite solar cells, the techniques used to characterise properties of materials related to solar cell, correlated to optoelectronic measurements on thin films and on complete solar cells, aiming to correlate the understanding of materials processing, properties and solar cell performance.

2.1. Device Fabrication and Measurement

2.1.1. Planar Perovskite Solar Cells

In my study p-i-n planar-structured perovskite solar cells, *i.e.* no mesoporous layer, are fabricated. In **Figure 2.1 a** the schematic drawing of device structure and layer composition is shown and in **2.1 b** a flat-band diagram of the energy levels are shown. P-i-n herein refers that an intrinsic perovskite layer sandwiched by a p-type hole transport layer (HTL) on the bottom substrate and an n-type electron transport layer (ETL) on the top. In such a device architecture the indium-doped tin oxide (ITO) acts as anode for hole extraction, while the metal contact works as cathode for electron extraction.

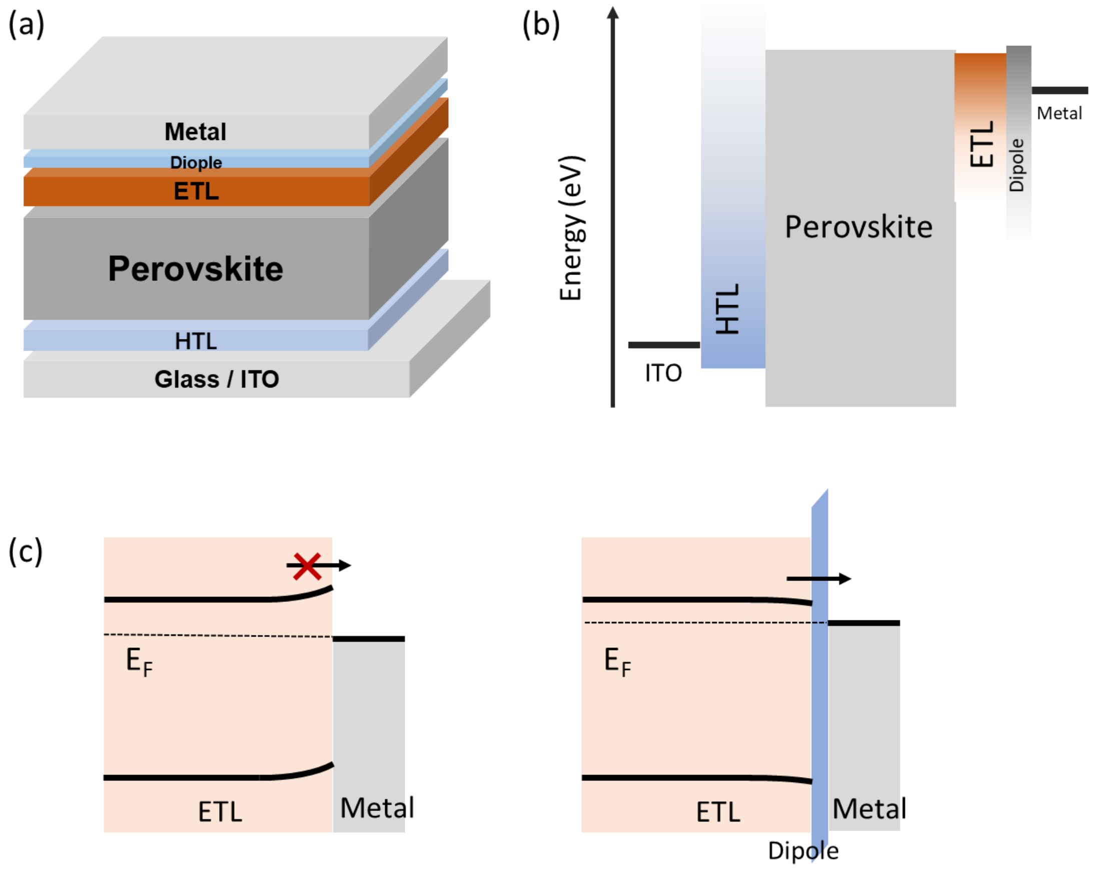

Figure 2.1 Schematic drawing of **(a)** a p-i-n perovskite solar cell, (**b**) the flat-band energy diagram, and **(c)** the ETL/metal interface with and without interfacial dipole layer.

Importantly, an interfacial dipole layer needs to be deposited between ETL and metal electrode, usually an ultra-thin layer of solution-processed bathocuproine (BCP) thermally evaporated lithium fluoride (LiF). This is because the work function of metal electrodes (*e.g.* Ag, Cu) is higher than the work function of ETL, thus a Schottky contact is formed at ETL/metal interface forming electron extraction barrier. This typically leads to "S-shape" in the measured current-voltage (J-V) curve,[82,83] severely reducing obtained efficiency. The dipole layer can reduce the effective work function of metal and thus form an ohmic contact at the interface. In **Figure 2.1 c** and **2.1 d** a schematic drawing of band diagram at ETL/metal interface is shown, highlighting how the dipole layer modifies the interfacial band bending.

2.1.2. Device Fabrication

Substrate and HTL

Prior to device fabrication, all ITO substrates were sequentially cleaned in ultrasonic bath using acetone, isopropanol and deionized water, each for 10 minutes, and finally dried under an argon flow. Immediately before use all substrates were treated by oxygen plasma for 10 minutes to completely remove contaminations.

The HTL employed in this study include Poly(3,4ethylenedioxythiophene)-poly(styrene sulfonate) (PEDOT:PSS, Ossila LTD), poly[bis(4-phenyl)(2,4,6-trimethylphenyl)amine] (PTAA, Ossila LTD) and poly[N,N'-bis(4-butylphenyl)-N,N'-bis(phenyl)benzidine] (PTPD, Ossila LTD). PEDOT:PSS was used as received while PTAA and PTPD were received as powders and were dissolved in chlorobenzene. In **Figure 2.2** the chemical structure of the materials used is shown. The processing conditions for these HTLs are summarised in **Table 2.1**.

The hydrophobic nature of PTAA and PTPD results in poor wettability of perovskite precursor solution. To address this issue an ultrathin layer of Poly [(9,9-bis(3'-(N,N-dimethylamino)propyl)-2,7-fluorene)-alt-2,7-(9,9–dioctylfluorene)] (PFN-Br) polyelectrolyte layer was spun onto PTPD or PTAA. PFN-Br was used as polyelectrolyte for electron extraction in organic solar cells,[84] the mechanism of why PFN shows no detrimental impact on HTL surface remains unknown so far.

Table 2.1 Processing conditions of HTL, ETL, interlayer and electrode.

Layer composition	Materials	Solution	Spin speed	Annealing conditions	Thickness (nm)
HTL	PEDOT:PSS	Dispersion in water, used as received	4000 rpm	150°C, 20 min	40
	PTAA	$0.25\%_{wt}$ in chlorobenzene	5000 rpm	No	20
	PTPD	$0.25\%_{wt}$ in chlorobenzene	5000 rpm	No	20
HTL surface modifier	PFN	$0.25\%_{wt}$ in methanol	5000 rpm	No	< 10
ETL	PCBM	23 mg ml^{-1} in chlorobenzene	2000 rpm	No	40
Interfacial dipole layer	BCP	0.5 mg ml^{-1} in methanol	4000 rpm	No	< 10
	LiF	Thermal evaporation			0.7

Metal contact	Ag or Cu	Thermal evaporation	100

Perovskite Layer

The processing methodologies for perovskite layers are summarised in **Table 2.2**. The $CH_3NH_3PbI_3$ (MAPI) perovskite precursor solution was prepared by co-dissolving equimolar lead iodide (PbI_2, 99.9985%, Alfa Aesar) and methylammonium iodide (MAI, Dyesol) in mixed solvent of gamma-butyrolactone (GBL) and dimethyl sulfoxide (DMSO) with volume ratio of 7:3. The solution was stirred for 1 hour at 60 °C, and was filtered infiltrated with a polytetrafluoroethylene (PTFE, with 0.45 μm pore size) filter before use. The perovskite active layer was formed via a toluene-dripping method.[85] The precursor solution was first spun at 500 rpm for 5 seconds and then 2000 rpm for 20 seconds. 0.5 ml of toluene was instantly dripped onto the film right at the end of second stage of spinning, followed by spinning at 4000 rpm for 20 seconds.

An alternative method to prepare perovskite films is to dissolve equimolar PbI_2 and MAI in a mixture solvent of N,N-Dimethylmethanamide (DMF) and DMSO with volume ratio of 9:1.1. The solution was stirred at 50°C for 1 hour to fully dissolve the precursors and was infiltrated before use. 40 μl precursor solution was dropped onto substrates with hole transport layers and was spun at 4000 rpm for 30s. At the 7th second, 0.5 ml diethyl ether was instantly dripped onto the spinning substrate. The substrates were then annealed on a hot plate at 100°C for 15 minutes.

Spin-coating is one of the cheapest and most widely used fabrication methods of PSCs. It involves evaporation of solvent and convective self-assembly process of the precursors that immediately induce the formation of crystalline perovskite materials. Simple spin coating, however, does not yield homogeneous perovskite film. The remaining pinholes are particularly problematic for planar substrates. Such issue was

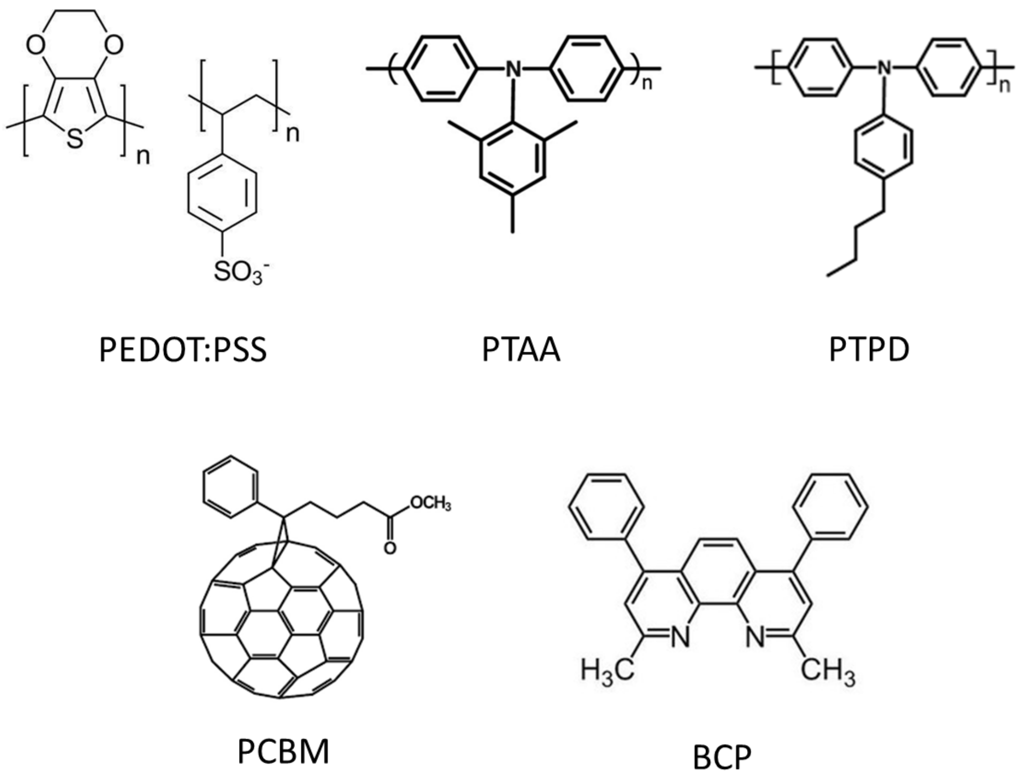

Figure 2.2 Schematic drawing of a of the chemical structures of the organic materials used in PSC fabrication.

overcome dripping anti-solvent (i.e. the solvent that does not dissolvent perovskite such as chlorobenzene, toluene, etc.) onto the spinning substrates during conventional spin coating, resulting in dense film with smooth surface and full coverage on the substrate. In such methods the solution normally comprises two different solvents with different boiling point (usually DMF/DMSO or GBL/DMSO). Dripping of anti-solvents washes off DMF or GBL, leaving an "intermediate phase" of MAI-PbI_2-DMSO complex compound.[86] This because DMSO can coordinate with PbI_2 to form a $PbI_2(DMSO)_2$ complex.[87] Unlike fully crystalline phase, such intermediate phase can fully cover the substrate. Further thermal annealing allows for slow evaporation of remaining DMF and formation of crystalline perovskite films.

ETL, Interfacial Dipole and Metal Contact

A fullerene derivative, Phenyl-C61-butyricacid methylester (C60-PCBM), was used as ETM in chlorobenzene. The solution was stirred at 40 °C for 1h and was infiltrated before use. The PCBM solution was spin-coated on MAPI film at 2000 rpm for 45 seconds. The interfacial dipole layer was prepared by either spin-coating BCP solution or thermally evaporate 0.7 nm of lithium fluoride (LiF) and Finally, the devices were completed by thermally evaporating 100 nm of Ag or Cu at a pressure of 5×10^{-6} mbar.

Table 2.2 Processing conditions of perovskite layer.

	Method 1	Method 2
Precursors	$PbI_2+CH_3NH_3I$ (1:1 mol)	$PbI_2+CH_3NH_3I$ (1:1 mol)
Concentration (mol L^{-1})	1.25	1.5
Solvent	GBL+DMSO (7:3 vol)	DMF+DMSO (9:1.1 vol)
Spin protocol	500 rpm, 5s → 2000rpm, 10s → 4000rpm, 20s	4000 rpm, 30s
Anti-solvent	0.5 ml Toluene, drip at the15th s	0.5 ml Dither ether, drip at the 7th s
Thermal annealing	100°C, 20 min	100°C, 20 min

2.1.3. Device Measurement

Current density-voltage (J-V) characteristics were measured with a Keithley 2400 source meter. Voltage is applied to the device and the current is recorded. The devices were illuminated by an AM 1.5 xenon lamp solar simulator (Oriel Instruments). The intensity was adjusted to 1 Sun by changing the working current, which was calibrated using a Si reference photodiode. All devices were stored in dark prior to measurement and were measured in a nitrogen-filled chamber. External quantum efficiency (EQE) spectra were measured with a PV Measurements QEX10 system. The spectral response was measured between 300 and 850 nm and was calibrated with a silicon reference photodiode.

2.2. Materials Characterisation Methods

To develop a thorough understanding of the processing-structure-performance relationships in the perovskite materials prepared, an insight into the materials characterisation methods routinely used is critical. In this chapter the four main characterisation techniques used are introduced. In brief, scanning electron microscopy (SEM) is widely used in this work to assess the morphology of perovskite thin films, while transmission electron microscopy (TEM) is employed to probe the microstructural defects and compositional homogeneity in the films. The variation of perovskite crystallinity is examined by X-ray diffraction and the work function of both perovskite films and charge transport layers are studied using Kelvin probe measurements.

2.2.1. Scanning Electron Microscopy

The imaging process of a SEM involves bombarding the specimen with a high energy primary electron beam that interacts with the specimen resulting in a number of beam-specimen interactions. Imaging is, in this case, obtained by collecting the low energy secondary electrons (< 50 eV).[88,89] The image is constructed by scanning the electron gun across the specimen surface. In **Figure 2.3 a** the schematic drawing of the imaging process using SEM is shown.

The contrast in a SEM image depends on the yield of secondary electrons (δ), *i.e.* the higher the yield the brighter the area will be. The value of δ is relatively insensitive to the composition of the specimen but is sensitive to the topography of specimen surface. More secondary electrons can escape from the surface it the topography is elevated or from the edge of structures *e.g.* grain boundary regions. As a result, δ and these regions will appear brighter, which is the main mechanism that morphological variation of the specimen can be observed. Owing to the low energy of the secondary electrons, only those generated near to the surface can escape from the specimen, thus this imaging mode is useful for examining the surface morphology.[88,89]

The resolution of SEM image is determined by the volume of the specimen surface where secondary electrons are generated - the smaller the sampling volume the better the resolution Typically, the highest resolution for SEM image is around 10 nm. There are two secondary electron detectors available in the SEM used in this work, the position and proximity to the sample of which vary allowing improved image quality under near-identical imaging conditions, although this improvement is at the expense of depth of field. In addition to secondary electrons backscattered electrons, *i.e.* incident electrons that escape from the spacemen inelastic scattering, can also be collected to construct images. Notably, the yield of backscattered electrons depends strongly on atomic number – the areas with heavier elements appear brighter, and this signal can be used to probe sub-surface inclusions and is excellent for elemental contrast, however resolution is poor. Another useful signal generated in the SEM are characteristic X-rays that are generated from the specimen when the primary electron beam interacts, as these are characteristic they can be collected as a function of their energy giving rise to energy-dispersive X-ray spectroscopy (EDX/S) which can be used to provide spatially resolved elemental composition information.[90]

Figure 2.3 b shows a typical surface image of $CH_3NH_3PbI_3$ films prepared with method 1 described in section 2.1. The polycrystalline structure is evident with well-defined grains and grain boundaries, both highlighted. It is worth noting that no compositional information can be directly obtained image without complementary characterisation techniques.

2.2.2. Transmission Electron Microscopy

While SEM utilises secondary electrons generated from the specimen surface, transmission electron microscopy (TEM) constructs the image with electrons that are transmitted through the specimen. The fundamental principle of TEM is the diffraction of an electron beam when passing through the specimen. The angle of electron diffraction is usually very small according to Bragg’s law (see next section),[91] as the electrons have rather small wavelengths (~ $1x10^{-12}$ m), about 1000 times smaller than the wavelength of X-rays (~ $1x10^{-9}$ m). TEM shows exceptional resolution down to approximately 0.1 nm.[89,92]

Figure 2.3 c shows schematically the imaging mechanism of a TEM. Using a parallel electron beam to illuminate the specimen and placing an objective aperture below, diffraction patterns can be observed.[93] The diffraction pattern of a single crystalline area is a regular array of spots, while that of a polycrystalline area is typically concentric rings. By selectively passing through the diffraction pattern using an aperture, different mode of images can be formed. Bright-field (BF) image is formed by selecting the beam comprising all transmitted, undiffracted electrons,[94] as such the area that has less interaction with incident beam, such as voids, grain boundaries, polymers, etc, will appear brighter. In contrast, dark-field (DF) image is formed using only one of the diffracted beams. In this case the area that more strongly diffract incident electron beams will appear brighter.

The contrast of TEM, *i.e.* the magnitude by which variation in the microstructure can be identified, depends on *i)* the amplitude changes of the electron beam and *ii)* the phase changes of the electron bean as it passes through the sample. The former, termed amplitude contrast, is determined by the mass or thickness of specimen and by the diffraction that occurs to electron beam in the specimen.[89,92,94] For example, the relatively thick and/or high-Z (where Z is atomic number) region more strongly diffract the electron beam and thus appear darker in a BF image but brighter in a DF image; some specific regions of the specimen can also diffract differently from the nonboring region, such as crystalline defects or bending areas. The later, phase contrast, arises from the differences in the phase of electron waves, which interfere with one another as they are scattered. Importantly, the phase contrast can be detected down to the atomic scale resulting in high-resolution images.

Scanning transmission electron microscopy (STEM) is designed specifically to optimize the formation and detection of a focused, scanned beam. The configuration of STEM is similar to that of a conventional TEM except that there is no lens below the specimen. However, in STEM configuration the convergent beam can scan across the sample using the scanning coils.[95] The BF and DF imaging mode of STEM are both analogous to that of conventional TEM, while the use of annular dark-field (ADF) detector and high-angle annular detector enables higher resolution and improved image contrast to be achieved by STEM than TEM.[96] Moreover, as STEM uses reduced dose of electron beam than TEM, beam damage to the specimen can be controlled.

In **Figure 2.3 d** a typical cross-sectional TEM image of complete device is shown with bright-field mode. The Spiro-OMeTAD and glass layer that weakly diffract incident

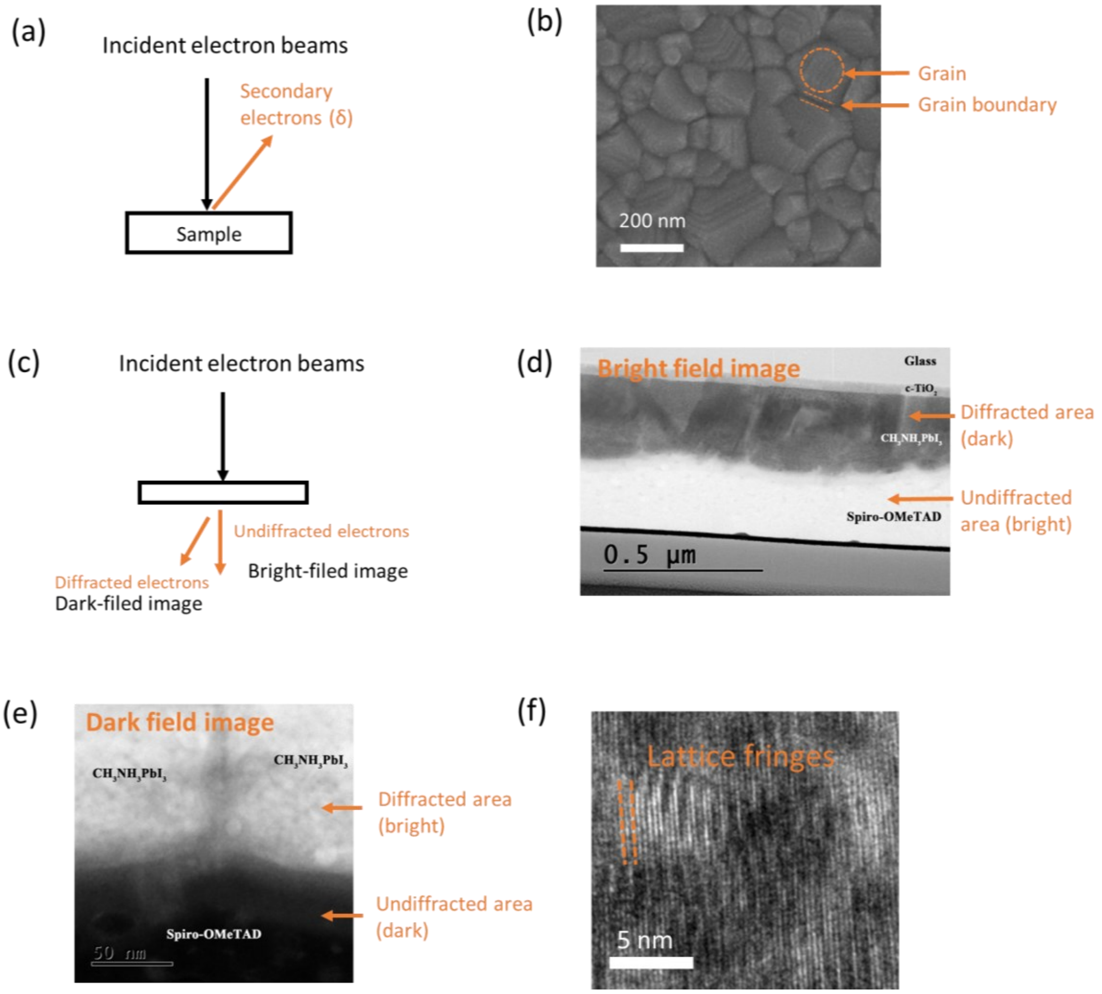

Figure 2.3 (a) Schematic drawing of the imaging mechanism of scanning electron microscopy (SEM). **(b)** A typical surface SEM image of $CH_3NH_3PbI_3$, where the morphological contrast between a grain and grain boundaries is marked. **(c)** Schematic drawing of the imaging mechanism of transmission electron microscopy (TEM). **(d)** A typical bright-field image of the cross-section of a perovskite solar cell. **(e)** A typical dark-field image (with higher resolution) of the cross-section of a perovskite solar cell. **(f)** Lattice fringes of perovskite crystal.

beams appears brighter than the perovskite and TiO_2 layer that shows stronger diffraction to incident beams. It is also observed that the grain boundaries appear brighter that the grains, as electron beam can pass through the grain boundaries. **Figure 2.3 e** shows a dark field image constructed by diffracted beams, where the bright and dark regions are inverted – the grains appear brighter than polymer layer and grain boundaries. **Figure 2.3 f** shows a typical HRTEM images with lattice fringes of

$CH_3NH_3PbI_3$ that are typically exhibit as the alignment of atoms. However, the periodicity observed here is due to phase contrast, the bright spots are interference maxima instead of real atom columns.

Because TEM requires transmission of electron beam, the thickness of specimen is controlled between 10 nm – 300 nm. This makes sample preparation in TEM much more complex than in SEM. The thinning of electron-transparent specimen is prepared by polish with chemical agents or ion beams. In particular, the cross-sectional samples of perovskite solar cells used in the studies shown in Chapter 4 are prepared with focused ion beam (FIB) milling.[97] This method involves with milling the bulk specimen with FIB, creating an electron-transparent "H-bar" structure and lifting out the thin strip with micro-manipulator.

2.2.3. X-ray Diffraction

X-rays can be diffracted by a plane of atoms resembling specular reflection of light by a mirror, which arises from constructive interference of all scattered X-rays by individual atoms. If there are multiple planes, reflection from each plane can add constructively in specific directions according to Bragg's law:[98]

$$2dsin\theta = \mathrm{k}\lambda \tag{2.1}$$

where d is the spacing between adjacent plane, θ is the incident angle, λ is the wavelength of incident X-ray and n is an integer. An X-ray diffraction (XRD) pattern is a plot of X-ray diffraction intensity at different angles. In this work a commercial powder diffractometer is used (which?). A monochromatic X-ray source scans through sample surface and the diffraction intensity is recorded, ending up with a plot of diffraction intensity versus θ (or d).[99]

Each "phase" in the studied material will produce a unique diffraction of pattern. The

XRD pattern from is a superimposition of all individual phase that exists in the sample. For the pattern of a phase, parameters obtained include the peak position, peak intensity and peak shape. The absolute intensity of diffraction peak is determined by complex factors, including electron density distribution of the atoms and the geometry of the unit cell. While understanding the origin of absolute intensity of each diffraction peak is beyond this study, variation of peak intensity, in combined with variation of peak position and the full width at half maximum (FWHM), is scrutinized to probe any change in thin-film crystallinity or orientation.[91]

The experimental XRD data are typically compared to reference patterns to determine what phases are present.[100] **Table 2.3** lists the selected peak parameters of tetragonal $CH_3NH_3PbI_3$.[55] The peak frequently referred to as characteristics of $CH_3NH_3PbI_3$ is the (110) peak, the corresponding {110} planes traverses the PbI_6 octahedron along I-Pb-I axis. A fingerprint of tetragonal structure is (002) peak appearing at slightly lower angle compared to (110) peak, as *c*-axis is longer than *a*-axis. In the meanwhile high-index peaks such as (211) and (310) emerge. The cubic structure of $CH_3NH_3PbI_3$ has a simpler structure of unit cell thus exhibits fewer diffraction peaks, including (100), (110), (111), (200). (210), etc. **Figure 2.4 a** shows a typical X-ray diffraction (XRD) pattern of $CH_3NH_3PbI_3$ thin films deposited on an ITO substrate of two thickness: 250 nm and 750 nm. Note that (110) and (002) peaks are not discerned in the measured pattern, due possibly to instrumental broadening of each peak.

Table 2.3 Calculated X-ray diffraction parameters of a tetragonal $CH_3NH_3PbI_3$.[55]

Peak index	2θ (°)	d-spacing (Å)	Relative intensity (%)
002	13.9513	6.3425	60
110	14.2216	6.2225	100

112	19.9730	4.4418	7
211	23.6509	3.7587	27
202	24.6041	3.6152	17
220	28.6684	3.1113	66
310	32.1387	2.7828	49

In **Figure 2.4 b** a magnified view of the (110) peak is shown, which shows the strongest intensity and is used as a characteristic diffraction peak for $CH_3NH_3PbI_3$ in most of the literature.[55] The two-dimensional view of a $CH_3NH_3PbI_3$ tetragonal crystal structure is shown in **Figure 2.4 c**, where the unit cell is highlighted and the {110} planes transverse the centre of PbI_6 octahedral. **Table 2.4** listed the measured parameters of (110) peak. There is a slight increase of d-spacing and decrease of crystallite size as film thickness increases. However, intensity of (110) clearly scales with film thickness, which is anticipated as the volume of crystalline materials increases that gives rise to stronger diffraction to incident X-ray.[91,99] It is also noted that diffraction of x-ray is dominated primarily by heavy atoms and thus is relatively insensitive to the organic cations.

The orientation of a thin film grown on substrate has profound impact on its optoelectronic properties, which can be characterized by probing the relative intensity of the diffraction peaks.[101] Within a polycrystalline film the lattice planes can face any orientation, but only the diffracted X-ray by planes that are parallel to the substrates can be detected. This is because in our standard X-ray diffractometer the X-ray generator and detector rotate synchronously around the sample, shown in **Figure 2.4 d**. In **Figure 2.4 a** relative intensity of (220) peak and (310) peak are also compared in the two films and observed a decrease of ratio of (220) over (310) peak intensity as film thickness increases. It suggests that there is less portion of (110) lattice planes lying parallel with the substrates in the thicker film. **Figure 2.4 d** also points out the limitation of conventional diffractometer, that is, only the lattice planes parallel to the substrate is probed, while those facing other directions remained unexplored. To address this issue Grazing-Incidence Wide-Angle X-ray Scattering (GIWAX) that is capable of probing the thin-film crystallinity in a large range of directions with respect to the substrate.[102–104]

Table 2.4 Measured parameters of (110) peak of two perovskite film.

Perovskite thickness (nm)	2θ(°)	Intensity (counts)	d-spacing (Å)	FWHM (°)
250	14.1569	9338	6.25	0.0708
750	14.1451	11971	6.26	0.0866

2.2.4. Kelvin Probe Analysis

Kelvin probe measures the contact potential difference established between a sample with respect to a reference electrode, from which the average work function (WF) can be determined if the WF of reference electrode is known. A Kelvin probe force microscopy (KPFM), more used in characterizing thin-film samples, can map the surface potential or WF of the sample with high spatial resolution.[105]

KPFM is established on the instrumentation of atomic force microscopy system (AFM). The contact potential difference (CPD) between the tip (reference electrode) and the sample surface is defined as

$$CPD = \frac{\varphi_{tip} - \varphi_{sample}}{-q} \tag{2.2}$$

where φ is WF of sample and tip. A more negative CPD indicates lower WF of the sample surface. The absolute WF of the tip is obtained by measuring the CPD with respect to a known sample, from which the WF of investigated sample can be measured. Typical calibration sample is the highly oriented pyrolytic graphite (HOPG) that has a known WF of 4.6 eV after fresh cleavge.[106] Kelvin probe measurement is usually complemented by photoemission spectroscopy to quantify E_F, ionization potential (IE) and electron affinity (EA).[17]

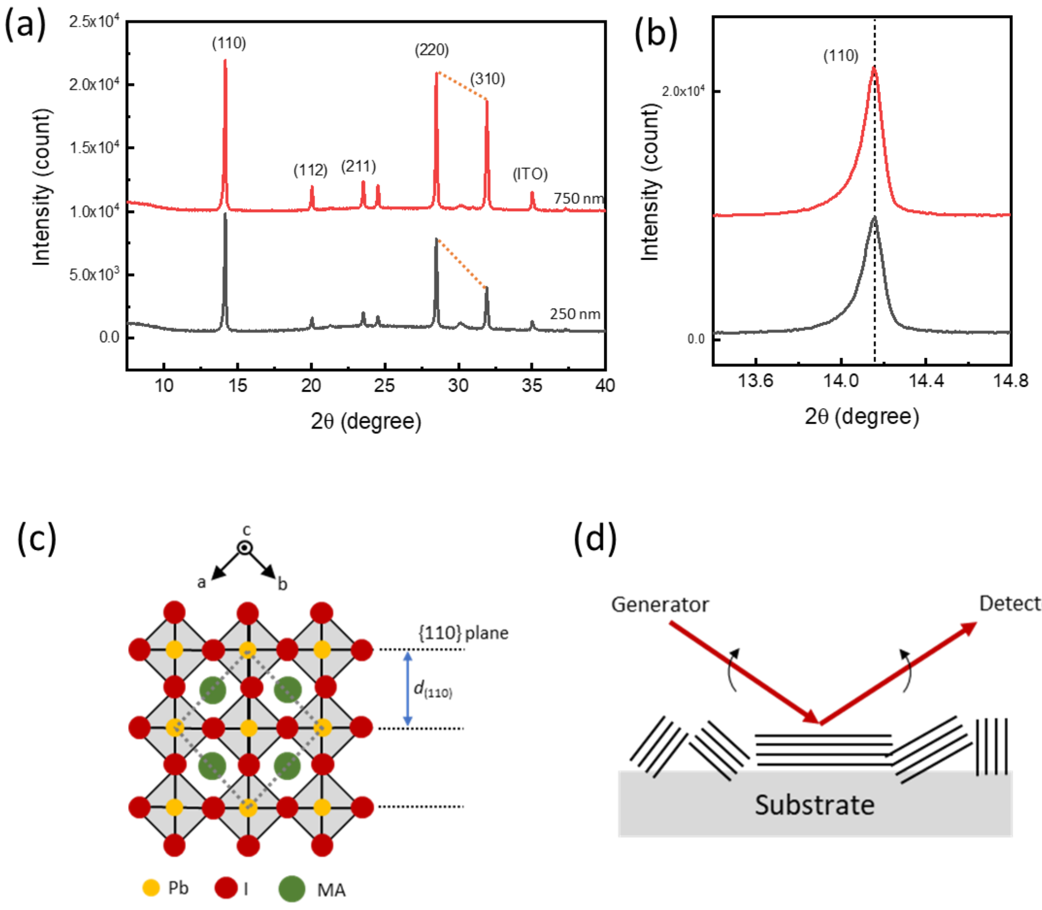

Figure 2.4 (a) X-ray diffraction pattern of thin-film $CH_3NH_3PbI_3$ (250 nm and 750 nm) deposited on ITO substrates. **(b)** Zoom-in figure of (110) diffraction peak. **(c)** 2-D schematic drawing of $CH_3NH_3PbI_3$ crystal, where the unit cell and {110} planes are indicated. **(d)** Schematic drawing of the alignment of diffractometry and substrate.

2.3 Spectroscopic Characterisation

The charge carrier dynamics in perovskite films are probed with a combination of spectroscopic techniques including steady-state photoluminescence, time-resolved single photon counting and transient absorption spectroscopy. These techniques measure charge recombination or charge transfer on different time scales. The multiple channels of charge recombination in a solar cell are summarised in **Figure 2.5 a**: photon absorption by perovskite generates free charge carriers; A free electron and a free hole can recombine band-to-band radiatively (channel I), alternatively a free electron can be captured by a trap states (deep or shallow) and subsequently recombine with a free holes (channel II); In presence of charge accepting materials, electrons can be transferred to an electron-transport layer (ETL, channel III) and holes to a hole-transport layer (HTL, channel IV), resulting in non-radiative interfacial recombination (channel IV). These processes critically determine the performance of perovskite solar cells.

2.3.1. Photoluminescence Spectroscopy

Photoluminescence (PL) is the emission of photons as the radiative transition of photoexcited carriers from excited states to ground states occurs. This corresponds mainly to the radiative pathways (I).[107] The steady-state PL spectrum are obtained by applying a constant source of photoexcitation, typically monochromatic light, and scanning the emission wavelength and recording the intensity of emitted photons with a photo detector. For a radiative transition, the energy difference between these the two states is emitted as photons. While absorption may involve all states in the semiconductor that normally yields a broad spectrum, emission occurs only between a narrow band of states filled by thermalized electrons.

The energy distribution of the emission peak is correlated to the transition energy of excited states, whereas the intensity of emission peak is determined by the portion of excited carriers recombining through the radiative channels. The intensity of PL can be attenuated due to presence of intra-gap trap states (channel II) or charge accepting materials (channel III and IV) that provide non-radiative recombination pathways. A shift in peak position is mainly associated with variation of band-gap energy. A typical spectrum of $CH_3NH_3PbI_3$ thin film is shown in **Figure 2.5 b**, in combined with an absorbance spectrum of the perovskite. Here the wavelength of excitation light is 635 nm, the emission peak lies at 765 nm corresponding to an approximately 1.55 eV band-gap energy. Note that the emission peak is overlapped with the onset in the absorbance spectra, where the sharp absorption edge is critically correlated to low Urbach tail energy.[61]

The steady-state PL spectroscopy has been widely employed to characterised in semiconducting thin films or quantum dots,[107] where the impact of chemical impurities, nanostructures and doping on the emission spectrum are demonstrated. PL emission intensity is a typical figure-of-merit assess formation of electronic trap states,[108–110] and

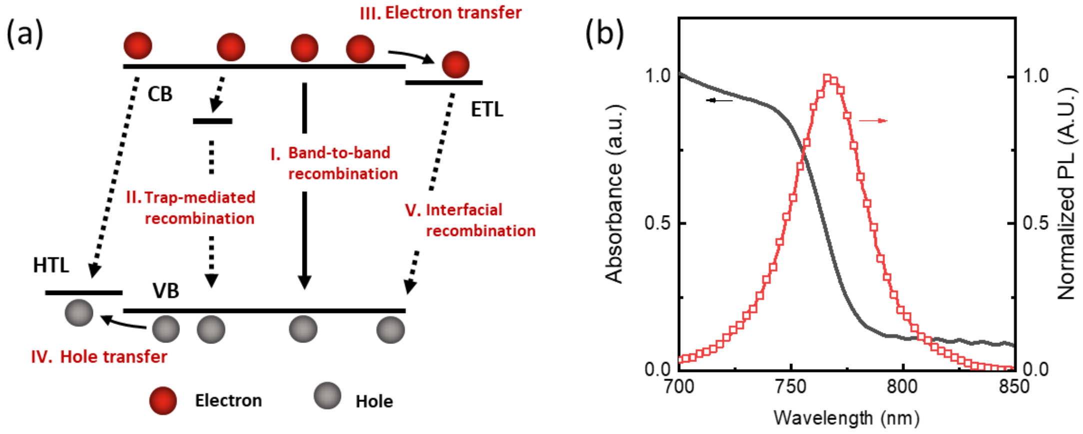

Figure 2.5 (a) Schematic drawing of charge recombination and charge transfer in a PSC. **(b)** Absorbance and photoluminescence (PL) emission spectra of a $CH_3HN_3PbI_3$ film.

thus enhancing PL of perovskite films is a paramount consideration for the optimisation of solar cells performance.[108,111–115] The energetic shift in PL spectrum is also an indication of change of band-gap energy correlated to segregation of halides in mixed perovkite,[116–118] while the shape of PL emission peak is also related to change in perovskite crystal structure.[118–123]

Application of steady-state PL spectroscopy can be extended from films to complete solar cells, where charge carrier dynamics most relevant to solar cell operational conditions are elucidated. Characterisation of CIGS solar cell reveal that *i*) the intensity of PL varies depending on the cell is at open-circuit, short circuit or with external load, and that *ii*) the open-circuit PL intensity is strongly correlated to V_{OC} and PCE,[124] analogous to the trend we found in PSCs (see Chapter 5).[125] Typically PL of the solar cell at open circuit increases exponentially with V_{OC}, as according to Planck's law both quantities are determined by the separation of quasi-Fermi levels.[126] It is also shown that a complete solar cell yields stronger PL emission than a neat film, highlighting the role of contact layers on suppressing non-radiative recombination.[127] Plot of PL intensity across the J-V curve quantifies the impact of series on solar cell performance.[128] More recently, PL of PSCs reveals the dominant recombination mechanism to be bimolecular recombination of free carriers, as a significant PL quenching can be observed when in direct contrast to that in OPVs.[38]

2.3.2. Time-resolved Single Photon Counting

Time-correlated single photon counting (TCSPC) technique is used to probe time-resolved photoluminescence (PL) decay.[129] In contrast to steady-state PL spectroscopy, time-resolved (TR) PL spectroscopy records the time-dependent profile of emitted light intensity upon excitation. This technique is based on detection of single photons of a periodic light signal, measurement of photon arrival time and reconstruction of the waveform from the individual measurements. It makes use of the fact that the probability of detecting one photon in one signal period is below one due to high repetition plus low intensity of the signals, the detection probability of a single photon at a certain time after excitation is proportional to the luminescence intensity at that time. In principle, the detection of multiple photons can be neglected. The measurement involves successive excitation-collection cycles recording the arrival times of single photons with respect to a reference, ends up with building up a histogram of photon arrival times.

The decay of PL signals manifests the disappearance of radiative species in the perovskite films. In **Figure 2.6 a** two spectra of typical PL decay dynamics of a solution-processed $MAPbI_3$ films (the thickness is around 500 nm) are shown, excited with a 435-nm laser pulse of varied intensity. Under the lowest excitation density (0.15 nj cm^{-2}), the decay dynamics exhibit a clear bi-exponential behaviour: a fast-decay phase in the first few nanoseconds (τ_1 = 1.9 ns), followed with a slow-decay phase in the time scale of hundreds of nanoseconds (τ_2 = 210 ns). These features are assigned to two recombination processes: The fast-decay phase is normally attributed to charge trapping,[130] shown in **Figure 2.6 c**, that photoexcited carriers rapidly relax into sub-gap traps. The slow-decay phase is attributed to bimolecular recombination (denoted as “BR” in the figure) of photoexcited electrons and holes. Herein the bimolecular recombination takes a pseudo-first-order form, where an approximate mono-exponential form is shown and a lifetime can be obtained, as the density of photoexcited charge carriers is small compared to the density of intrinsic charge carriers in perovskite film. Note that under such weak excitation density, the fast-decay phase quenches approximate 85% of total PL emission intensity. The trapping process rapidly reduces charge density remaining in the film, resulting in reduced radiative recombination rate seen in the slow-decay phase, which does not necessarily indicate that all photo-generated charge charges are long-lived.

Figure 2.6 a also shows that the PL decay dynamics can be altered as excitation intensity is increased. Under an excitation density of 0.34 μj cm^{-2}, the magnitude of fast-decay phase is reduced. This is ascribed to filling of trap states as density photoexcited carriers increases,[9] schematically shown in **Figure 2.6 c**. The slow-decay phase deviates significantly from mono-exponential and becomes more like a power-law decay.[13] This is owing to bimolecular recombination as photoexcited charge density is comparable with background charge density. In such case the recombination is much faster owing to increase of photoexcited charge density.[16] It is noted that these analyses haven't considered Auger recombination, which is typically observed when charge density exceeds 10^{17} cm^{-3}, or photon recycling that occurs to rather thick film.

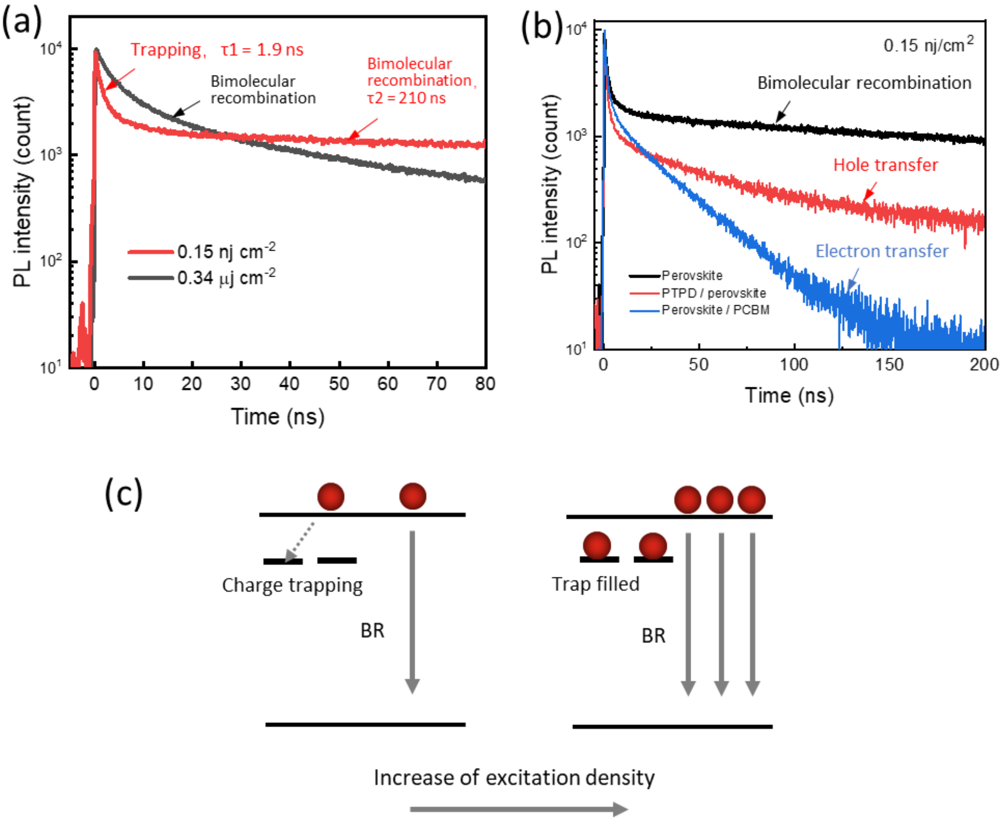

Figure 2.6 (a) TRPL spectroscopy of a typical $CH_3HN_3PbI_3$ films measured with different excitation densities. **(b)** TRPL spectroscopy of a neat $CH_3HN_3PbI_3$ film and a $CH_3HN_3PbI_3$ film with CTLs. **(c)** Schematic drawing of band diagram showing the evolution of recombination mechanisms as excitation density increases.

In neat perovskite film it is a general trend that long PL decay lifetime is correlated to high V_{OC} and high PCE,[110,131–133] consistent with previous analyses of inorganic solar cells.[124,134] When charge transport layers, *i.e.* electron transport layer and hole transport layer, are in contact with the perovskite layer, PL emission can be greatly reduced, often referred as PL quenching, due to charge transfer to CTLs.[135] The red and blue lines in **Figure 2.6 b** shows the PL decay dynamics when $CH_3NH_3PbI_3$ is contacted with PTPD or PCBM. It remains, however, unclear so far whether there is a simple correlation between PL lifetime in contacted films with V_{OC} or PCE. This is because that PL decay dynamics cannot be exclusively assigned to charge transfer or interfacial recombination followed with charge transfer, unless supplementary probe on the contact layer is provided.[136]

Limitation in Data Interpretation

While a large volume of literature has assigned quenching of PL signal to the desirable charge extraction when perovskite films are contacted with CTLs, such simple interpretation remains problematic or even erroneous.[137] Instead, PL quenching in these samples are interpreted as interfacial (or surface) recombination, and was shown by literature[38,138] and our study presented in Chapter 5[125] that higher PL quenching efficiency correlates to greater V_{OC} loss. Such misinterpretation may come from classically ascribing PL quenching in OSCs to charge separation at the donor-acceptor interfaces. Interestingly, also in OSC quenching of PL leads to partially loss of charge carrier potential energy due to formation of charge transfer states at the donor-acceptor interface.[139]

2.3.3. Transient Absorption Spectroscopy

The ultrafast transient absorption spectroscopy (TAS) probes photophysical and photochemical reactions taking place on timescales ranging from tens of femtoseconds (fs) to a few nanoseconds (ns) upon light absorption. It makes use of an ultrafast laser system that produced pulsed excitation signals with femtosecond (10^{-12} s) duration.[140] As shown in the schematic drawing in **Figure 2.7 a**, the samples are electronically excited with pulsed signals, followed with a probe pulse that passes through the sample with a delay time with respect to pump pulse. As the sample is excited with the pump pulse, it will not absorb the probe pulse as much as the pump pulse. Then a difference of absorption spectrum can be calculated, ΔA, corresponding to the absorption spectra of excited sample (by probe pulse) minus the absorption spectra of the sample in ground state (by pump pulse). By altering the delay time between pump and probe pulse, a time-resolved profile of ΔA can be obtained comprising the dynamics processes of excited species in the sample.

In general the difference in absorption ΔA contains contribution from i) ground-state bleaching that arises from reduced ground state population after excitation, ii) stimulated emission from excited states and iii) absorption of the excited states.[140] **Figure 2.7 b** shows a typical femtosecond (fs) absorption spectra of a thin-film $CH_3NH_3PbI_3$ (500 nm) deposited on glass substrate. The spectrum is featured with two photobleaching peak at 480 nm and 755 nm. While the latter unambiguously assigned to transition from valence band (-5.4 eV) to conduction (-3.9 eV), the later is thought to be related to the transition between a deeper "valence band ii" (-6.5 eV).[141] Probing the transients of the photobleaches provide insight into the dynamics of charge carriers.

Compared with TRPL spectra, the advantage of TA spectra is that it can ubiquitously determine the dynamics of photogenerated species (free carriers or weakly bounded excitions). The observation of PL decay matching TA decay confirms that the decay of radiative species monitored with PL are indeed the dynamics of photoexcited charge carriers.[142] Similarly, the observation of photovoltage (TPV) decay overlapping TA decay indicates that the TPV dynamics are indeed generated by free charge recombination (see discussion in next section).[143]

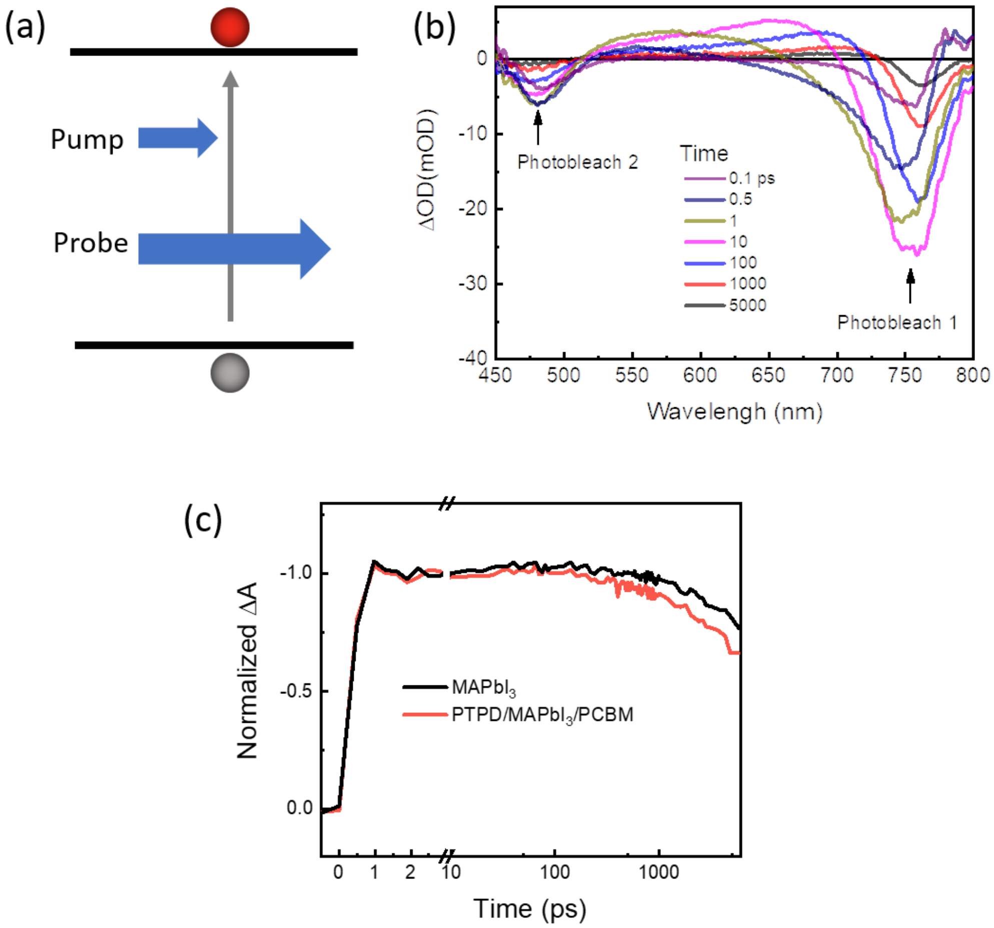

Figure 2.7 (a) Schematic drawing of "pump-probe" measurement of transient absorption (TA) spectroscopy. **(b)** TA spectra of a $CH_3NH_3PbI_3$ film deposited on glass substrate. **(c)** Decay dynamics of TA bleaching peak at 755 nm of a $CH_3NH_3PbI_3$ film and a contacted $CH_3NH_3PbI_3$ film.

Figure 2.7 c shows the decay dynamics of the bleach signal at 755 nm up to 6 ns. Our previous study shows that a sub-picosecond decay can be observed when the excitation density is low, assigned to ultrafast charge trapping or relaxation that otherwise saturates at higher laser intensities.[9] The slower decay in a few ns is assigned to bimolecular recombination between electrons and holes.[144] When contact layers are added, a faster decay can be observed suggesting increased bimolecular recombination. This is assigned to electron and hole transfer from perovskite to contact layers.

2.3.4. Limitation and Perspective

PL spectroscopy probes only the disappearance of radiative species inside perovskite layer, while the subsequent dynamics, such as the recombination lifetime of transferred charge, is unknown. While TAS can probe non-radiative species, our current experimentation focuses only on perovskite layer. Charge transfer and interfacial recombination, as is shown in previous investigation on DSSCs, can be elucidated by probing the TA spectra of ETL or HTL,[136]

2.4 Optoelectronic Characterisation

Critical to understanding the dominant recombination mechanism in a solar cell is to probe the density and recombination lifetime of photoexcited change carriers. In this section we move on to a couple of optoelectronic characterisations of complete solar cells. The methods are based mainly on small-perturbation assumption, where we combine transient photovoltage (TPV) and transient photocurrent (TPC) measurement to probe the charge density and charge lifetime in a working solar cell.

2.4.1. Transient Photovoltage Measurement

Transient photovoltage (TPV) is a small-perturbation measurement, where a photovoltage deflection (ΔV, approximately between 0.01 to 0.03 V) is induced by an optical perturbation while the solar cell is held at open circuit against constant background light. Under small perturbation condition, the amplitude of TPV is much smaller than the steady-state quantity, *i.e.* $\Delta V \ll V_{OC}$. This allows for straightforward interpretation of the transient data as background condition remains relatively constant. To ensure open circuit condition in our experimentation, the device connects with a $1 M\Omega$ resistor and is illuminated continuous white light. The device can be held at different V_{OC} by tuning light intensity. A pulsed laser source with wavelength of 635 nm provides the optical perturbation. The experimental set up is shown in **Figure 2.8 a**. Following an excitation pulse the change in concentration of electrons and holes can be measured indirectly by monitoring the TPV transients. The critical part of TPV transients to analyse is its decay kinetics.

Given that small-perturbation condition is satisfied, the decay of TPV takes the form of single exponential correlating with a pseudo first-order recombination process,[145] *i.e.* the decay rate is determined by density of excess carrier density induced by perturbation

$$\Delta V \propto \exp\left(-\frac{t}{\tau_{\Delta n}}\right) \tag{2.3}$$

In such condition a lifetime can be extracted from the pseudo-first-order rate constant $k_{\Delta n}$ [s^{-1}] ($\tau_{\Delta n}$=1/$k_{\Delta n}$) by fitting the decay with mono-exponential, quantifying the recombination rate of excess electrons in the PSC:

$$\frac{d\Delta V}{dt} \propto \frac{d\Delta n}{dt} = -\frac{\Delta n}{\tau_{\Delta n}} = -k_{\Delta n}\Delta n \tag{2.4}$$

Figure 2.8 b shows the log-log plot of TPV transients over a range of background light intensities – it shows that not only the amplitude of initial voltage-rise but also the lifetime of TPV decay is reduced as light intensity increases. A key issue relevant to this equation is that the TPV decay transients indeed measure the depopulation of photoexcited charge carriers, rather than alternative process such as dielectric relaxation. This has been proved by the overlapping of TPV signals and TAS signals when measured against the same background light.[143] However, owing to the higher opaqueness of PSCs compared to OPV devices, such comparison is not able to be carried out in PSC in this study.

Fitting the TPV transients under varied background light arrives in the observation that $\tau_{\Delta n}$ decreases mono-exponentially with device V_{OC} at higher light intensities:

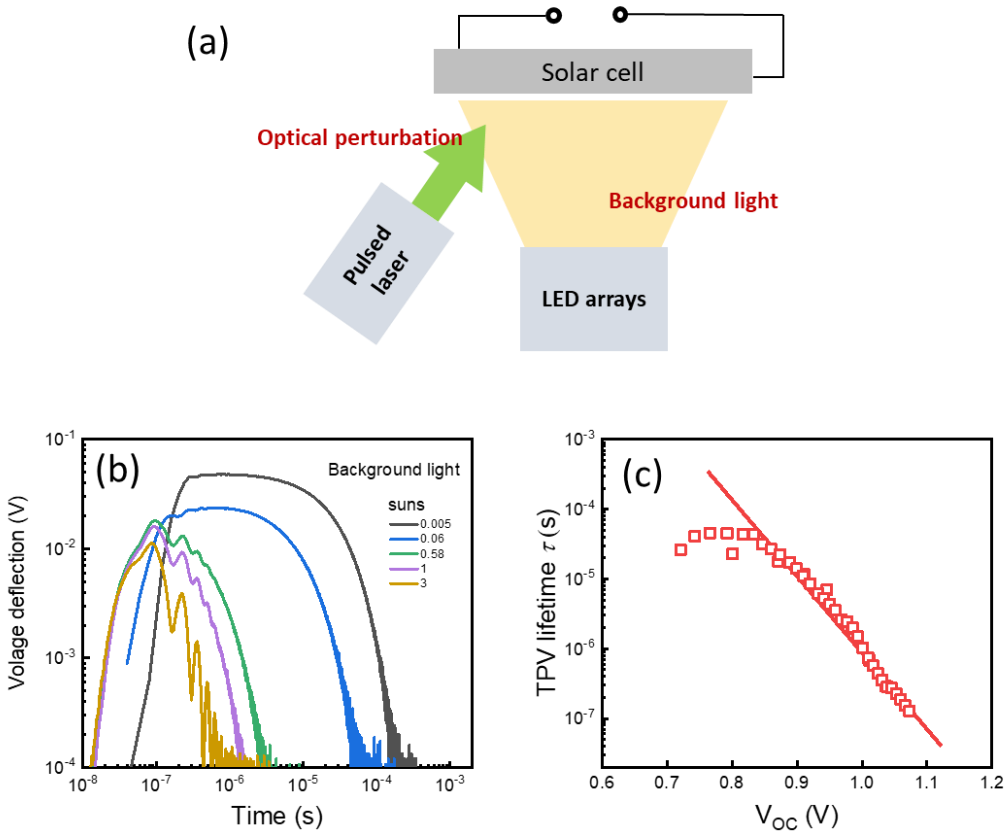

Figure 2.8 (a) Schematic drawing of the experimental set up. **(b)** Transient photovoltage (TPV) decay of a perovskite solar cells under varied light intensities. **(c)** TPV lifetime as a function of V_{OC}.

$$\tau_{\Delta n} = \tau_{\Delta n_0} exp\,(\frac{qV_{oc}}{\vartheta k_B T}) \tag{2.5}$$

shown in **Figure 2.8 c**. This is anticipated for a recombination process with a power law dependence on charge density. These data suggest that $\tau_{\Delta n}$ is determined mainly by the background charge density that is determined by active layer quasi-Fermi level splitting (V_{OC}) -- higher charge density results in shorter lifetime.

Interestingly, it is observed that TPV lifetime of monocrystalline Si (m-Si) solar cells decreases exponentially with V_{OC} at lower light intensities but is independent of V_{OC} at higher light intensities. The former is assigned to capacitive discharge lifetime while the latter is assigned the "sought-after" bulk recombination lifetime.[146] Such interpretation is likely due to the quasi-Fermi level splitting occurs only in the junction region in a m-Si solar cell, as described in Chapter 1. whereas the bulk (i.e. thick p-type region) remains neutral and thus its hole density is unchanged. However, this is unlikely to not mean the observed exponential $\tau_{\Delta n}$-V_{OC} in PSCs are determined by capacitive discharging.

2.4.2. Differential Charging

Differential Capacitance

Figure 2.9 a schematically draws a band diagram at open circuit: a dynamics equilibrium is established between charge generation and charge recombination, giving rise to a certain amount of "excessive" charge carriers "stored" in the device. These photogenerated charges are excessive with respect to the intrinsic (dark) charge in the device, resulting in splitting of electron and hole quasi-Fermi levels that equals to device V_{OC}. The density of excessive charge n can be directly measured by charge extraction (CE) technique. It involves with a device at steady state being switched from open circuit (OC) to short circuit (SC) and probing the current transient to obtain charge density. However, O'Regan *et al*[147] and Wheeler *et al*[148] have shown that CE technique yields exaggerated n in $MAPbI_3$ solar cells owing to migration of ionic defects. Alternatively, differential charging technique is used to measure capacitance and thus charge density in perovskite solar cells. Differential charging only requires the device to be held at open circuit, thus migration of ionic defects can be avoided. Indeed, differential charging is found to give essentially the same charge density as the charge extraction in DSSCs and in organic solar cells.

The capacitance of the solar cell can be if the amount of excess charge (ΔQ) and the resulting voltage deflection (ΔV) induced by optical perturbation is known

$$\frac{\Delta Q}{\Delta V} = C_{DC}(\mathrm{V}) \tag{2.6}$$

Here ΔV is determined from the extrapolated maximum value of voltage deflection by fitting the TPV decay with mono-exponential. Then the charge density can be calculated by integrating C_{DC} with respect to V_{OC}

$$n = \frac{1}{Aqd}\int_{0}^{V_{oc}} C_{DC}\, dV \tag{2.7}$$

describing the amount of excess, which refers to photogenerated herein, charge carriers "stored" in the device at open circuit. ΔQ is the amount of charge generated by laser pulse and can be measured separately by a transient photocurrent (TPC) technique (described in the next section).

Figure 2.9 b shows the capacitance *vs* V_{OC} for a typical PSC with ITO/PTAA/perovskite/PCBM/Ag structure. Apparently, two regimes can be observed depending on the magnitude of V_{OC} (controlled by light intensity). At low light levels C_{DC} is relatively invariant with voltage, suggesting that the solar cell works close to a parallel-plate capacitor and that a considerable fraction of photoexcited charge carriers is stored in the metal electrodes and/or charge transport layers (CTLs). The measured capacitance, 65 nF cm^{-2}, is assigned to the electrode capacitance of the PSC. At higher light levels C_{DC} starts to increase with voltage, assigned to the chemical capacitance of perovskite active layer. This corresponds to the charge stored in the electronic states of perovskite active layer as quasi-Fermi levels approach the band edges of perovskite. The outstanding observation here is that the capacitance does not show rigid exponential increase with V_{OC} up to 0.5 Sun, showing a small "tails" in the capacitance-V_{OC} plot, in contrast to the data of DSSCs[145] and OPVs.[143] This is possibly correlated to charge accumulation in the contact layers (*i.e.* metal electrodes and charge transport layers). **Figure 2.9 c** shows total excess charge density (n) as a function of V_{OC} by fitting the capacitance at higher light levels (> 0.5 Sun) that are most relevant to solar cell operation. As the spatial disruption of n in the solar cell remains unknow, we herein only plot two-dimensional charge density. It shows that n increases exponentially with V_{OC}

$$n = n_0 \exp\left(\frac{qV_{oc}}{mk_BT}\right) \tag{2.8}$$

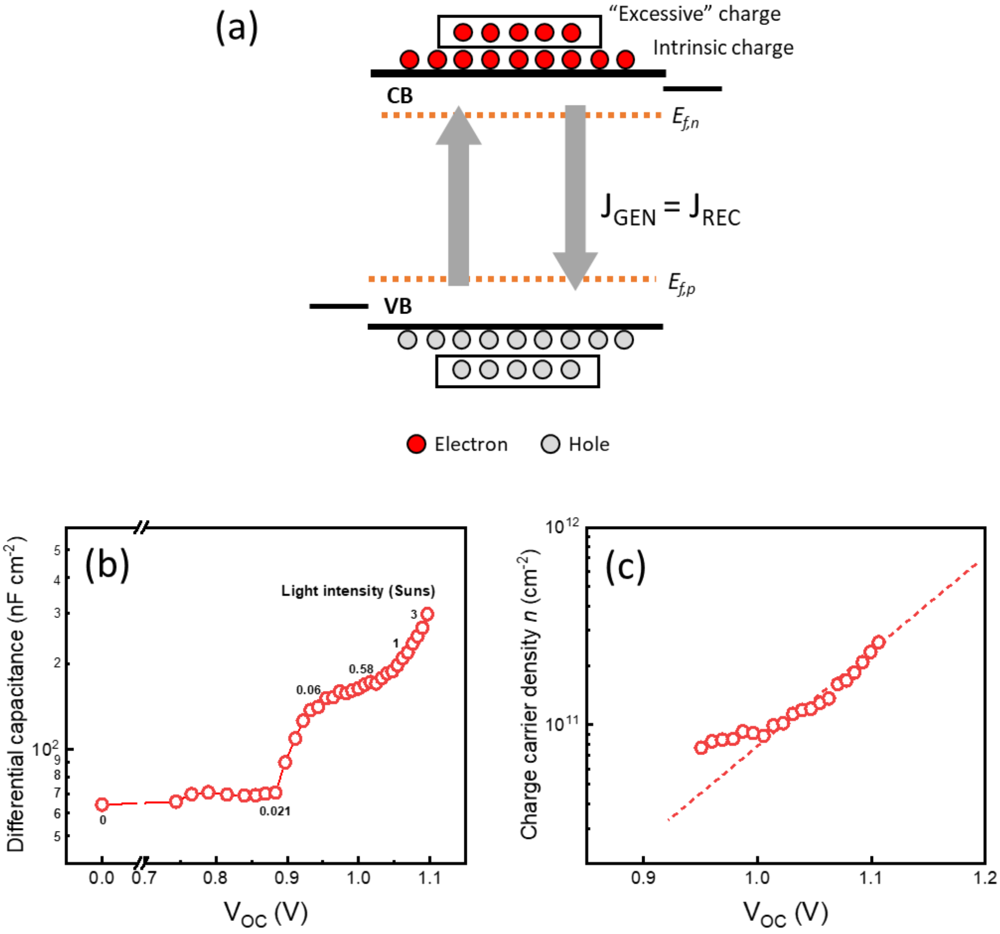

Figure 2.9 **(a)** Schematic drawing of a band diagram at open circuit, showing a dynamics equilibrium between charge generation and charge recombination and a certain amount of "excessive" charge carriers "stored" in the device. **(b)** Differential capacitance as a function of V_{OC} for a typical PSC. **(c)** Total excess charge density (n) as a function of V_{OC} by fitting the capacitance at higher light levels.

The slope of n-V$_{OC}$, describing how charge density scales with quasi-Fermi level splitting, is affected by distribution of tail states, device thickness and surface recombination. In principle Herein m = 3.5 suggests that multiple trapping process is involved in the recombination mechanism of perovskite solar cells.[149]

Transient Photocurrent Measurement

Transient photocurrent (TPC) measurement is a complementary technique to TPV measurement. With the solar cell held at short circuit, the small amount of excess charge induced by layer pulse is extracted resulting in a photocurrent transient. Integration of the transients arrives in the value of ΔQ. This method assumes negligible recombination loss at short circuit, *i.e.* all generated charge is extracted. Experimental data show negligible loss of ΔQ as the background light intensity is sufficient low.[148] Thus to charge recombination loss the TPC measurement is carried out under approximately 0.1 – 0.25 Sun background light intensity.

2.4.3. Recombination Order

The TPV measures the lifetime of the excess charge carriers generated by laser pulse, whereas the lifetime of the total charge carriers is more relevant to device performance. The total lifetime can be determined by knowing the overall recombination order (δ) of the device:

$$\tau_n = \delta\tau_{\Delta n} \tag{2.9}$$

The deduction of equation is shown below, which arrives in the correlation of δ, m and ϑ expressed as

$$\delta = \frac{m}{\vartheta} + 1 \tag{2.10}$$

In broader context, δ describes the power-law dependence of recombination rate (R) on charge density (n)

$$R = k_0 n^{\delta} \tag{2.11}$$

which describes how many species are involved in the charge recombination. The recombination rate of total charge density, which is typically of higher order, can be expressed in a pseudo-first-order form:

$$\frac{dn}{dt} = -k_0 n^{\delta} = -k_n n \tag{2.12}$$

Where k_0 is a density-independent constant while k_n is a density-dependent constant, as such the total recombination rate including small perturbation charge is

$$\frac{d(n + \Delta n)}{dt} = k_0 (n + \Delta n)^{\delta} \tag{2.13}$$

This equation can correlate small-perturbation recombination rate to total recombination rate:

$$\frac{d\Delta n}{dt} = -\frac{dn}{dt} - k_0 (n + \Delta n)^{\delta} \tag{2.14}$$

Then

$$\frac{d\Delta n}{dt} = k_0 n^{\delta} [1 - \left(1 + \frac{\Delta n}{n}\right)^{\delta}] \tag{2.15}$$

When Δn << n, a Taylor expansion will give

$$\left(1 + \frac{\Delta n}{n}\right)^{\delta} = 1 + \delta \frac{\Delta n}{n} \tag{2.16}$$

Thus equation 2.13 can be written as

$$\frac{d\Delta n}{dt} = -\delta k_0 n^{\delta-1}\Delta n \tag{2.17}$$

Thus

$$k_{\Delta n} = \delta k_0 n^{\delta-1} = \delta k_n \tag{2.18}$$

This arrives in equation (2.9) as such the overall lifetime of total charge can be derived from the measured small perturbation lifetime if the reaction order is known.

A straightforward interpretation is that $\delta = 1$ indicates the recombination between free and deeply trapped charges, where only the population of one of the carriers determines the recombination rate. We have $\delta = 2$ the recombination between two free charges while $\delta > 2$ the recombination involves multiple trapping processes. However, the interpretation of δ is more complicated as it is parallelly affected by the spatial distribution of charge, an issue strongly influenced by solar cell thickness, and doping of photoactive material that is normally controlled by material synthesis methodology.[149]

It is observed in our previous study[110,148] that perovskite solar cells typically exhibit δ greater than 2, which is consistent with the general acknowledgement of trap-mediated recombination in these solution processed solar cells.

2.4.4. V_{OC} Reconstruction

If we've correctly estimated charge density and charge recombination lifetime, we should be able to calculate the recombination flux

$$J_{Rec} = \frac{Q}{\tau_n} \tag{2.19}$$

where Q is the total charge [C]. At open circuit condition a dynamic equilibrium is reached by charge generation and charge recombination, and charge generation flux can be estimated by short circuit current J_{SC}. Q and τ_n are correlated with V_{OC} according to equation 2.5, 2.8 and 2.9, where a combination of these equations arrives in reconstructed V_{OC}

$$V_{oc}^{Rec} = \frac{mk_BT}{q\delta}\ln\left(\frac{\tau_{n,0}J_{SC}}{qn_0}\right) \tag{2.20}$$

it shows that V_{oc}^{Rec} is determined by the fitting parameters m, δ $\tau_{n,0}$ and n_0 [cm^{-2}] and measured J_{SC}. Therefore, a good match of calculated V_{OC} with measured V_{OC} relies on correct estimation of the charge density and recombination of lifetime.

2.4.5. Light Intensity-Dependent V_{OC} and J_{SC}

V_{OC} versus light

The open circuit voltage (V_{OC}) equals the splitting of quasi-Fermi level and measures the charge density in a solar, thus is a light intensity (lnt)-dependent quantity.

$$V_{OC} \propto \frac{n_{id}kT}{q}\ln\left(\mathrm{lnt}\right) \tag{2.21}$$

V_{OC} increases approximately linearly with ln(lnt) as is shown in **Figure 2.10 a**. Closely related to the recombination mechanism is the value of ideality factor, n_{id}, that can be derived from the slope of V_{OC}-lnt. Herein the n_{id} derived from V_{OC}-lnt is completely free from the influence of series resistance compared with n_{id} derived dark current.[150] As shown in **Figure 2.10 b**, sufficient data point achieved by power-tunable LED illumination source allows n_{id} to be calculated differentially.

Theoretically n_{id} describes how recombination varies exponentially with quasi-Fermi level splitting

$$R = R_0 \exp\left(\frac{\Delta E_f}{n_{id} kT}\right) \tag{2.22}$$

The value of n_{id} thus provide information on the recombination mechanism in the solar cell. Typical n_{id} = 1 when quasi-Fermi level of one carrier is fixed due to heavy doping of the semiconductor. This occurs in the so-called quasi-neutral region for a Schottky junction or a p-n junction, or in vicinity to the contacts where dark charge density is high. n_{id} = 2 is observed when recombination occurs in depletion region, or between a free carrier and a deep-trapped carrier. In contrast, $n_{\mathrm{id}} < 1$ is indicative of surface recombination.[151]

The observed value of n_{id} ranges from 0.9 – 1.7 in both my studies and in previous reports, depending on perovskite crystallinity, perovskite bandgap and hole transport layers. Owing that multiple processes, such as charge trapping or surface recombination, are involved in the recombination process, a simple correlation between the value of n_{id} and the charge recombination mechanism is difficult. The understanding of n_{id} in our study is supplemented by data of device performance or recombination dynamics. Interesting, we have observed that the device with higher V_{OC} and higher PCE exhibit n_{id} greater than 1, while strong surface recombination occurs at PEDOT:PSS/perovskite interface usually leads to n_{id} close to or below 1 (discussed in details in chapter 4 and 5). Such trend has also be reported by Tress *et al* in n-i-p perovskite solar cells.[152]

J_{SC} versus Light

In an ideal solar cell, short circuit current density (J_{SC}) equals to photogeneration flux, and scales linearly with light intensity. Deviation from linearity is usually observed owing to recombination losses. Instead, a power-law relationship is found given by

$$J_{SC} \propto lnt^{\alpha} \tag{2.23}$$

where α describes the linearity of J_{SC}. In previous studies on organic solar cells, α was typically found to be below 1 arising mainly from bimolecular recombination, which stems from a variety of factors including limited carrier lifetime/diffusion distance,[153154] formation of space-charge region[155] or high charge density at the electrode.[156] It was shown that, within the same device, α approaches to 1 as an external reverse bias is applied, owing that electrical field facilitates charge extraction and suppresses charge recombination.

Figure 2.10 c shows a typical logarithm plot of J_{SC}-lnt in p-i-n perovskite solar cells. While a general liner fitting over a certain range of light intensities was carried out in most of the literature, the variation of α with light intensity is neglected. Instead, similar

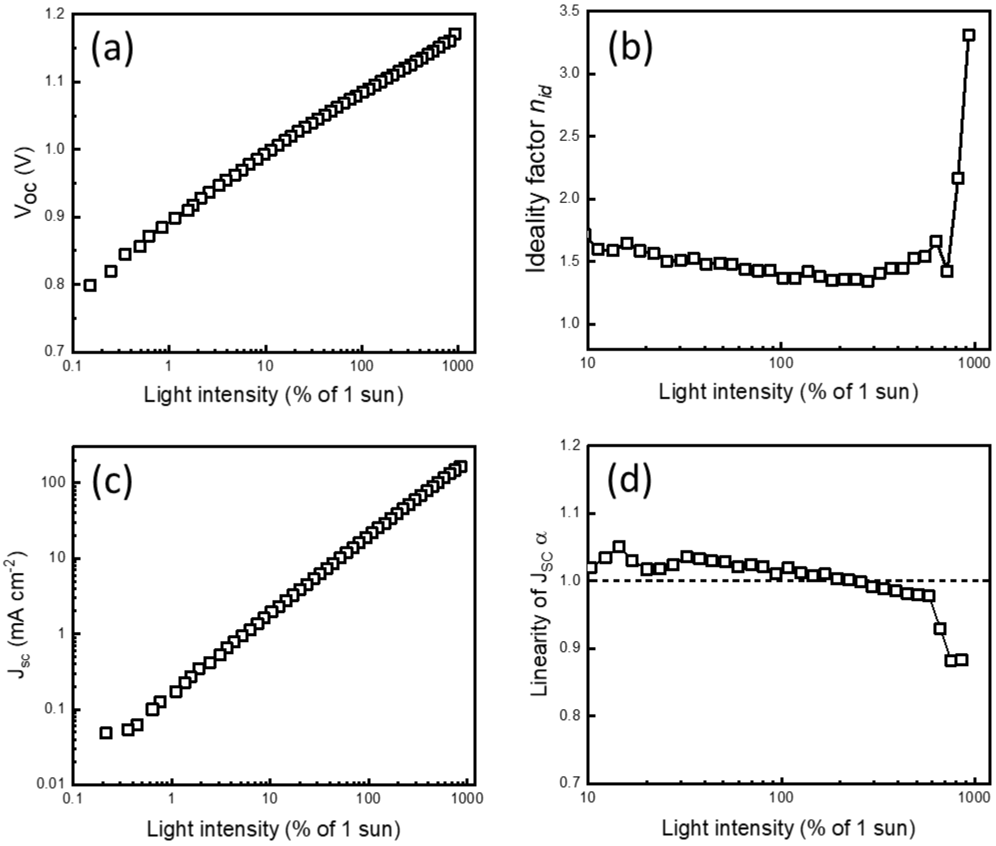

Figure 2.10 (a) V_{OC}, **(b)** ideality factor, **(c)** J_{SC} and **(d)** J_{SC} linearity as a function of light intensity.

with calculating n_{id} from V_{OC}-lnt, α is calculated by differentiating J_{SC} and is plot against lnt in **Figure 2.10 d**. The plot shows clearly that α varies with lnt: α is close to one under low light intensities and starts to drop below 1 as light intensity increases. This is expected as bimolecular recombination scales with photogeneration, leading to enhanced charge extraction loss at higher light intensities.

2.4.6. Limitation and Perspective

While DC indirectly measures charge density, an alternative *in-situ* approach is charge extraction (CE) that directly extracts and measures the density of photoexcited charge and has been widely carried out in dye sensitized solar cells (DSSC) and organic solar cells (OSC). In these literature DC and CE give essentially comparable charge density on the same device, while this doesn't hold for perovskite solar cells with $CH_3NH_3PbI_3$ absorber. Both O'regan *et al* and Wheeler *et al* found that CE yields significantly higher charge density than DC. The exaggerated charge density is thought to be the displacement current caused by ion migration when switching the device from open circuit to short circuit. In the solar cells based on "mix-cation" perovskite, however, the discrepancy of obtained charge density between appear to be negligible in our recent measurement, possibly owing that ion migration is considerably low in the mix-cation perovskite than in the MAPI perovskite.

3. Correlation of Thin-film Crystallinity, Sub-gap Tail States and Open-circuit Voltage

3.1. Declaration of Contributions

The results presented in this chapter formed the basis of reference [110]

Jinhyun Kim aided most of the photoluminescence spectroscopic measurement.

Jonathan Ngiam carried out the secondary ion mass spectroscopy (SIMS) measurement.

Shengda Xu took the SEM images.

.

3.2. Abstract

Recombination via sub-gap trap states is considered a limiting factor in the development of organometal halide perovskite solar cells. In this chapter, the impact of active layer crystallinity on the accumulated charge and open-circuit voltage (V_{OC}) is demonstrated in solar cells based on methylammonium lead triiodide ($CH_3NH_3PbI_3$, MAPI). The crystallinity of MAPI can be systematically tailored by modulating the stoichiometry of the precursor mix, where small quantities of excess methylammonium iodide (MAI) improves crystallinity increasing device V_{OC} by ~200 mV. Using *in-situ* differential charging and transient photovoltage measurements, charge density and charge carrier recombination lifetime are determined under operational conditions. Increased V_{OC} is correlated to improved active layer crystallinity and a reduction in the density of trap states. Photoluminescence spectroscopy shows that an increase in trap states correlates with faster carrier trapping and more non-radiative recombination pathways. The work in this chapter provide insights into the origin of V_{OC} in perovskite photovoltaics and demonstrate why highly crystalline perovskite films are paramount for high-performance devices.

3.3. Introduction

The progress power conversion efficiencies (PCEs) of state-of-the-art solar cells based on organometal halide perovskite solar cells (PSCs)[157] is closely associated with improvement of their open-circuit voltage (V_{OC}).[158] To date, impressive device V_{OC} values ,exceeding 1.2 V, have been achieved for PSCs with an optical band gap (E_g) of 1.6 eV.[159] However the photovoltages demonstrated do not yet reach the radiative efficiency limit.[160] Further reducing non-radiative photovoltage loss, either in the bulk active layer or at interfaces within the cell are key strategies to breaking the current efficiency record.[161]

Most of the high-efficiency, and therefore high V_{OC} (> 1 V), PSCs are fabricated with the conventional n-i-p structure, normally with planar or planar/mesoporous TiO_2 as an electron transport layer (ETL) deposited on a transparent electrode.[162] The loss of V_{oc} has been discussed in terms of interfacial recombination induced by top hole transport layers (HTLs),[159] or by bottom ETL.[163] Inverted devices *i.e.* p-i-n architectures, comprising poly(3,4-ethylenedioxythiophene) polystyrene sulfonate (PEDOT:PSS) as bottom HTLs are associated with greater losses in photovoltage and their V_{OC} is usually more than 100 mV lower than the V_{OC} achieved with n-i-p devices.[164] Despite these observed performance limitations, such devices are attractive due to their inherent compatibility with low temperature processing and reduced current-voltage (J-V) hysteresis,[165] which have been associated with low interfacial recombination rates.[7] In direct contradiction to this, significant V_{OC} losses have been attributed to strong recombination at the PEDOT:PSS/perovskite interface, and are shown to be suppressed by surface modification of PEDOT:PSS.[166] Higher V_{OC} values, *i.e.* > 1 V, have been achieved in devices where PEDOT:PSS is replaced with polymeric HTLs,[167,168] or p-type metal oxides,[169] resulting in PCEs approaching 20%. Similar effects of reducing interfiacial recombination to boost V_{OC} are also observed at perovskite/ETL interface.[170–172]

As photogenerated charge carriers are shown to accumulate in the perovskite active layer as well as the contact layers under open circuit conditions,[148,173] non-radiative losses in the bulk perovskite, *e.g.* recombination via trap states, can also influence device photovoltage in parallel with interfacial losses. For example, passivation of defects in bulk perovskites has resulted in further enhancement of the PCE of inverted architecture cells, where PCEs > 21 % and V_{OC} > 1.1 V are achieved.[174] Spectroscopic studies have revealed that charge carrier trapping processes are significant in solution-processed perovskite thin films,[12,175,176] with these trap states thought to have shallow tail of energies.[177] A continuum of energy levels have been observed with such traps states mediating non-radiative recombination, indicating their possible nature as shallow trap states.[178] Although a general relationship between a reduction in the concentration of shallow trap states and an improvement in device PCEs has been suggested,[179–181] the interplay between bulk perovskite properties, carrier trapping and photovoltage losses in perovskite solar cells remains unclear. In particular an *in-situ* investigation of such solar cells under operational conditions is required to understand how these shallow traps limit the attainable V_{OC} in perovskite solar cells.

Previous studies have shown the V_{OC} to be affectted by active layer morphology and composition [176,182,183] and charge transport layers.[171] This chapter aims to probe the origin of V_{OC} enhancements and examine the correlation between MAPI crystallinity, device V_{OC}, active layer tail states and charge carrier recombination dynamics using inverted architecture perovskite solar cells. It shows that MAPI crystallinity can be tailored by tuning the ratio of precursors in solution and how improvements in the crystallinity of our thin film MAPI layers can reduce V_{OC} losses. Combining differential charging (DC) and transient photovoltage (TPV) measurements of PSCs under operational conditions, we observe accumulation of photogenerated charge carriers with an exponential distribution *vs.* voltage, then the corresponding recombination time constant of this charge is estimated. Up to an 8-fold increase of tail state density is found to correlate with the V_{OC} losses, these trap states appear to be shallow, and accelerate the recombination rate. Photoluminescence (PL) measurements of the films showed rapid relaxation of carriers and an increased fraction of non-radiative recombination in the presence of higher concentration of trap states.

3.4. Experimental Results

3.4.1. Thin-film Processing

Our standard MAPI active layers were prepared from stoichiometric *i.e.* 1:1 molar ratio of PbI_2 and CH_3NH_3I (MAI). MAPI films with modulated crystallinity were prepared with solutions using excess (+2.5, +5 and +10 % $_{mol}$) or reduced (-0.5 % $_{mol}$) MAI. Note that whenever the terms 'MAI excess' or 'MAI deficient' are used in this paper, they refer to the relative stoichiometry of the precursor solution, not necessarily the stoichiometry of the resulting perovskite films which may have a different stoichiometry which was not measured directly. The solution processing of MAPI followed the established "antisolvent dripping" using toluene,[184] described in the experimental chapter.

3.4.2. Improvement of Thin-film Crystallinity

X-ray Diffraction

In **Figure 3.1 a** typical X-ray diffraction (XRD) patterns for the stoichiometric and modified films are shown. All of these data show well-defined diffraction peaks that are assigned to the tetragonal MAPI crystalline phase (and ITO substrate). **Figure 3.1 b** shows the calculated integrated peak areas of the (110), (112) and (211) diffraction peaks as a function of excess MAI content in the precursor solution. The (110) peak area increases significantly from MAI-deficient films to MAI-excess films, accompanied by a modest decrease of (112) and (211) peak area.

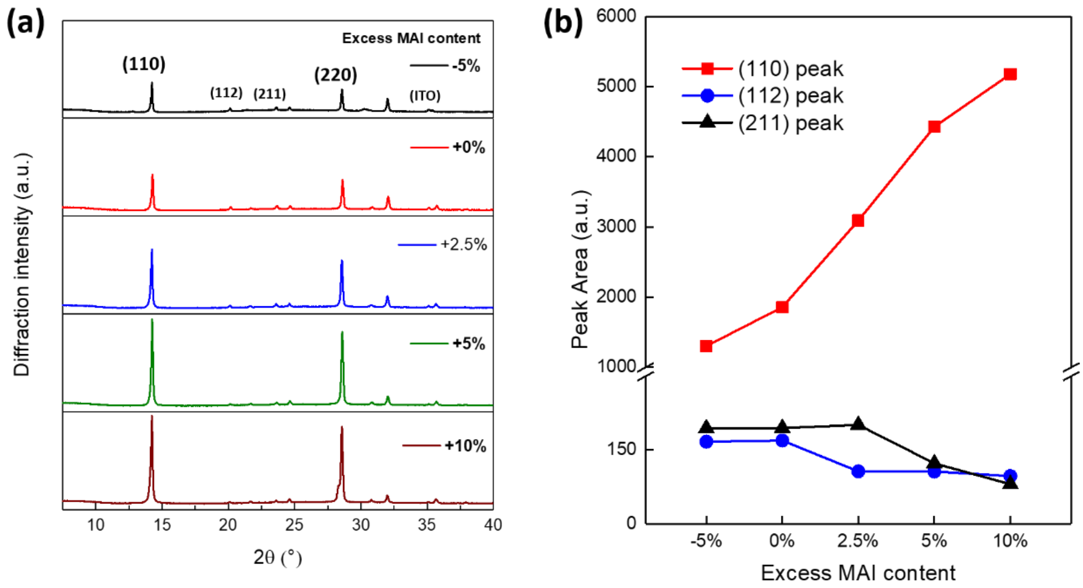

Figure 3.1 (a) X-ray diffraction patterns of $CH_3NH_3PbI_3$ (MAPI) films prepared with solutions containing varying methylammonium iodine (MAI), -5, +0, +2.5, +5 and +10 mol.%. **(b)** Measured integrated area of the (110), (112) and (211) diffraction peaks as a function of excess MAI content.

Scanning Electron Microscopy

Scanning electron microscopy (SEM) images, **Figure 3.2 a - e**, show polycrystalline grains that provide continuous substrate coverage of the MAPI films prepared from all solutions. For films prepared over the range -5 to +5 % excess MAI the SEM images show minimal variation in the thin film morphology, with lateral grain sizes in the region of 150 - 200 nm. A change of morphology in the MAPI film with 10% excess MAPI can be seen in **Figure 3.2 e**, where grains are less defined in comparison with all other compositions studied, a feature attributed to excess MAI accumulating in the grain boundaries and surface of the film. There is no evidence of secondary phase formation *e.g.* PbI_2 or MAI in either the XRD or SEM images.[185] Thus, given the comparable morphologies and grain sizes observed – and the comparable film thicknesses, it is concluded that the increased intensity of the MAPI {110} diffraction peaks as a distinct improvement in crystallinity with the emergence of a preferential orientation (texture) in the [110] direction. Therefore, in this preparation, the impact of adding excess MAI in the precursor solution is to promote the crystallization and oriented growth of the MAPI.

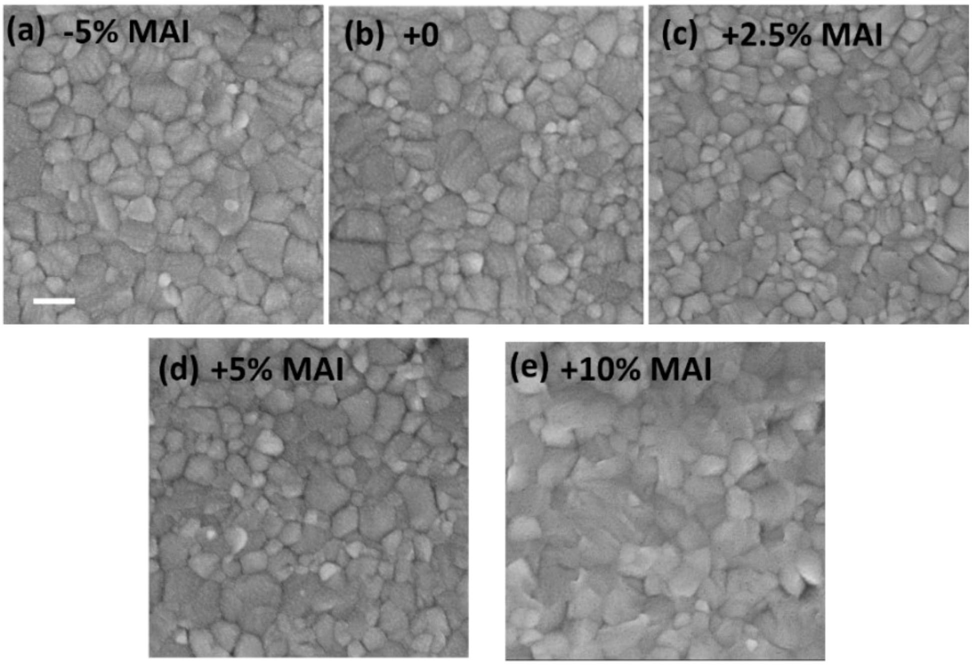

Figure 3.2 Scanning electron microscopy (SEM) images showing the surfaces of the MAPI films prepared with precursor solution containing different amount of excessive MAI. Scale bar in (a) shows 200 nm.

Secondary Ion Mass Spectroscopy

In addition to the change in orientation observed when a MAI excess is introduced, our time-of-flight the secondary ion mass spectroscopy (ToF-SIMS) data, **Figure 3.3**, suggest the MAI excess films are also denser. The data shows the negative ion signals, specifically C_3^- ($PC_{61}BM$), I_2^- and PbI_3^- (MAPI), and S^- (PEDOT:PSS) collected from ITO/PEDOT:PSS/perovskite/$PC_{61}BM$ devices.

The intensity of ion signals at each time point in **Figure 3.3** can be interpreted as indication of sputtering rate of those ionic species. Although the sputtering rates for C_3^-

species are similar for both compositions, the sputtering rate of I_2^- and PbI_3^- species are significantly higher in perovskite layers prepared from the stoichiometric mix of precursors compared with the 5% MAI excess active layer. This suggests that the preferentially orientated crystallites are more densely packed, which reduces the volume of the inter-crystallite regions *i.e.* regions that are either amorphous or disordered. The surfaces and interfaces of crystallites have been suggested to be susceptible areas for trap states in perovskite absorbers.[11]

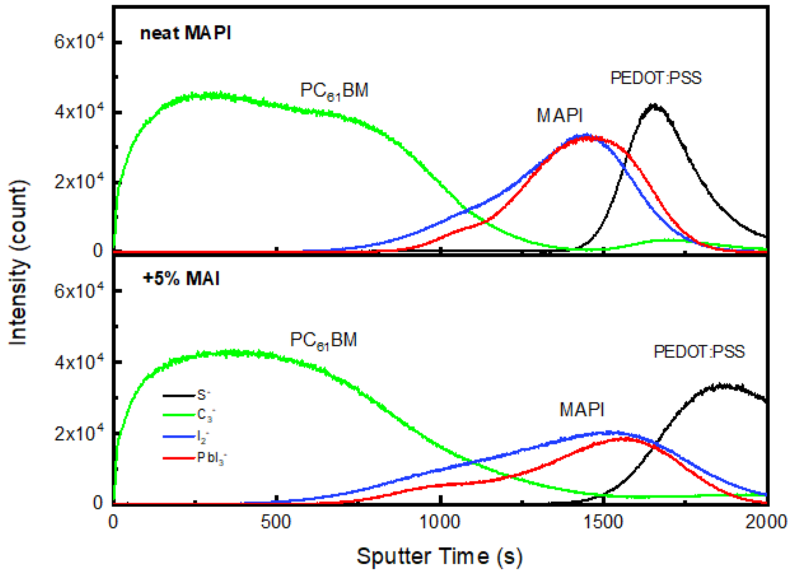

Figure 3.3 Secondary ion mass spectroscopy of neat MAPI film and +5%MAI MAPI film.

Mechanism of Crystallinity Improvement

From the XRD data no discernible change in position is seen with varying the MAI concentration. If the MAI was up taken into the perovskite lattice that the resultant defects would cause changes of lattice parameter, the magnitude of which would be within the detection limits of XRD.[186,187] There is a large increase of measured full

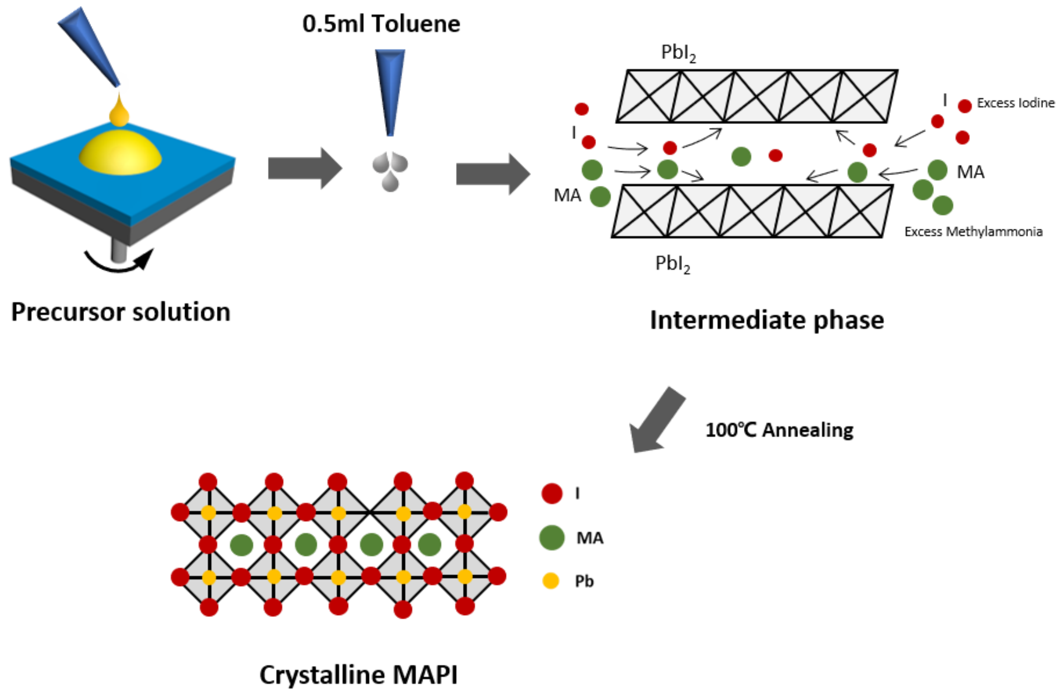

Figure 3.4 Schematic illustration of the fabrication of a MAPI layer and the role of excessive MAI in the precursor solution.

width at half maximum (FWHM) in the 10 % MAI excess film, suggesting a reduction of crystallite size, possibly due to the morphological disruption, shown by the SEM images. In the case where the MAI concentration is sub-stoichiometric the improvements in crystallinity and the emergence of texture are not observed. This may be due to PbI_2 formation prior to MAPI conversion *i.e.* after dripping the anti-solvent,[184] In contrast, an excess of free methylammonium and iodide ions could accelerate their interaction with PbI_2 and facilitate full conversion of PbI_2 into MAPI, schematically shown in **Figure 3.4**.

3.4.3. Device Performance

Figure 3.5 a shows the current density-voltage (J-V) curves of the optimum devices from each processing condition. Poly(3,4-ethylenedioxythiophene) polystyrene sulfonate (PEDOT:PSS) was used as a hole transport layer, [6,6]-Phenyl-C_{61}-butyric acid methyl ester (PCBM) as an electron transport layer with devices deposited onto

ITO coated glass electrodes and completed with a thermally evaporated LiF/Ag cathode. In the inset of **Figure 3.5 b** a schematic illustration of the device structures is shown. Photovoltaic parameters, based on a minimum of 5 devices, are summarized in **Table 1**. For the reference device, *i.e.* 1:1 molar ratio of PbI_2 and MAI, typical V_{OC} and PCE values of 0.89 V and 13.7 % respectively are comparable with literature reports,[188] although in general the performance of such devices is inferior to those prepared in the regular *i.e.* non-inverted architecture.[189] The device performances show a strong dependence on the crystallinity of MAPI layer and the best device, comprising highly crystalline MAPI prepared with 5% MAI-excess, shows a PCE of 16.7% that is comparable with the best efficiencies achieved with this structure in other studies.[190] It is apparent from these results that the improvements in V_{OC}, ~ 200 mV dominate the variation in measured PCE. Importantly, the MAPI films prepared show negligible variation in their optical absorption onset (approximately 784 – 786 nm for all films), as confirmed by the absorption spectra in **Figure 3.5 b**. **Table 3.1** also highlights the poor performance of the devices prepared with 10% MAI-excess, in such devices a reduction in V_{OC}, J_{SC} and FF are observed.[191] Owing to this the 10% MAI-excess films will not be considered in the following discussions.

Table 3.1 Typical device parameters from solar cells with MAPI prepared varying MAI:PbI_2 ratios, measured from a minimum of 5 pixels for each processing condition.

Excess MAI content (%$_{mol}$)	**J_{sc} (mA cm^{-2})**	**V_{oc} (V)**	**FF**	**PCE (%)**
-5	20.3 ± 0.5	0.844 ± 0.009	0.69 ± 0.01	11.6 ± 0.5
+ 0	20.5 ± 0.4	0.892 ± 0.006	0.75 ± 0.01	13.7 ± 0.3
+ 2.5	20.8 ± 0.7	0.960 ± 0.004	0.75 ± 0.01	15.0 ± 0.4
+ 5	20.8 ± 0.5	1.040 ± 0.008	0.77 ± 0.01	16.7 ± 0.3
+ 10	18.5 ± 1.2	0.942 ± 0.007	0.71 ± 0.02	12.3± 0.6

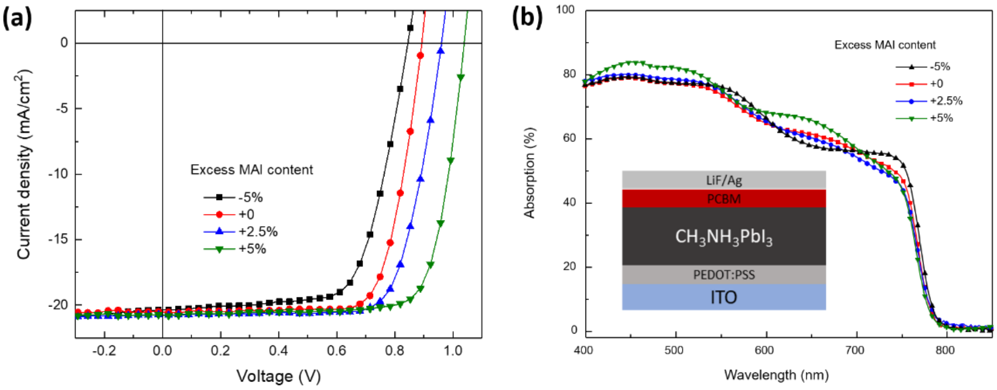

Figure 3.5 (a) Current density – voltage (J-V) curves under AM1.5 1-Sun equivalent illumination of MAPI solar cells prepared with a range of MAI concentrations. **(b)** Absorption spectra of the of MAPI layers, inset figure shows the schematic device structure.

3.4.4. Change of Charge Carrier Dynamics

To understand the relationship between gains in V_{OC} and improved MAPI crystallinity, transient optoelectronic measurements are employed to investigate the impact of charge carrier energetics and carrier recombination kinetics on device performance. These techniques have been used to characterize dye-sensitized solar cells,[145] organic solar cells,[192] and more recently employed to study V_{OC} losses in perovskite solar cells.[147,148]

As illustrated in **Figure 3.6 a**, C_{DC} (V = 0), *i.e.* in the dark, of the measured devices are between 35-41 nF cm^{-2}. This capacitance, as determined with no bias light, is assigned as the electrode capacitance ($C_{electrode}$) where charge carriers are accumulated at the ITO and Ag contacts. In our previous studies, this electrode capacitance has been shown to be independent of the device V_{OC} at very low light intensities (and thus low V_{OC}),[148] corresponding to the horizontal baseline representing $C_{electrode}$ drawn from approximately 0 - 0.7 V in **Figure 3.6 a**. At higher illumination intensities C_{DC} is observed to increase exponentially with V_{OC}, and the exponentially increasing component dominates the overall capacitance for > 0.2 sun equivalent. Previously we assigned this exponential capacitance to the chemical capacitance of MAPI active layer,[148] although it could also be related to the accumulation of charge in states at interface regions between the MAPI and charge transport layers.

Fitting the capacitance distribution with an exponential, the total excess electronic charge, Q [C cm^{-2}], stored in the device at open circuit can be estimated. Q is plotted as a function of V_{OC} corresponding to a range of light intensities in **Figure 3.6 b**. The exponential relationship of Q *vs* V_{OC} observed at higher light intensities, where $m \approx 3$, suggests that at least one charge carrier species may be accumulating in trap states within the MAPI layer or its interfaces since values of $m > 2$ cannot easily be explained by free charge carriers obeying Boltzmann statistics – particularly in devices where internal variations in electrostatic potential are screened by mobile ionic charge. If this is the case, then the density and distribution of these tail states are parameterized by Q_0 and m respectively in equation (2.3).

Table 3.2 Fitting parameters of transient optoelectronic measurement.

Excess MAI content (%$_{mol}$)	m	δ	$\tau_{n,0}$ (s)	Q_0 (C)
-5	3.2	3.1	500	3.5×10^{-14}
+ 0	3.0	2.9	1200	7.1×10^{-15}
+ 2.5	3.3	3.2	3500	4.6×10^{-15}
+ 5	3.0	3.1	4000	3.9×10^{-15}

The significant observation in **Figure 3.6 b** is that there is a parallel upwards shift in the Q *vs.* V_{OC} distribution correlated with reduced MAPI crystallinity, manifest in equation (2.8) as an increase of Q_0 value. Changes in the distribution of accumulated charge as a function of voltage have previously been observed, and were attributed to the change in the perovskite band gap resulting from iodide/bromide exchange,[148] a temporary redistribution of mobile ionic charge in the perovskite layer,[147] or, in organic solar cells, a broadening of density of states.[193–195] As there is negligible change of band gap, minimal hysteresis in our devices under this measurement regime, and only a limited change in the slope of the Q-V_{OC} plot (*m* value), the almost parallel shift in the Q vs V_{OC} relationship could be interpreted either as i) a change in the density of charge stored in sub-gap tail states or interface states for given quasi-Fermi level splitting (V_{OC}), and/or ii) a change in the relative charge carrier energetics, such that for a given amount of accumulated charge there is a change in the quasi-Fermi level (V_{OC}) splitting. For example, in the case of *i*) when V_{OC} = 0.9 V, corresponding to the vertical dashed lines, the electronic charge in the MAPI layer (+5% excess-MAI) will be approximately 4.6×10^{-9} C cm^{-3}, this increases for the same V_{OC} to 1.4×10^{-8} C cm^{-2} (+ 2.5 % MAI), 2.1×10^{-8} C cm^{-2} (+0%) and 3.6×10^{-8} C cm^{-2} (-5 % MAI) *i.e.* a near 8-fold increase in stored charge carriers is required to achieve the same V_{OC} as a result of an increasing density of tail states. It is noted that much of this charge may be re-injected/re-trapped into the valence/conduction bands from these shallow states multiple times before undergoing recombination. Q_0 describes the magnitude of this distribution of charge trapping states. With this tail density interpretation, there appears to be an 8-fold increase of tail state density between +5 % MAI and -5 % MAI cells. Alternatively, in case *ii*), for a fixed value of Q = 2.1×10^{-8} C cm^{-2}, corresponding to the vertical dashed line, the device's V_{OC} shifts from 0.99 V (+5 % MAI), to 0.92 V (+2.5 % MAI), 0.89 V (+0 %) and to 0.86 V (-5 % MAI) which could correspond to the different energetic depths of the tail states where these charge carriers reside.

The change in charge carrier lifetime induced by an increase in sub-gap tail state density is then considered, bearing in mind that charge generation flux is equal but opposite to recombination flux in a working solar cell at open circuit. A relaxation time constant, τ, can be derived from decays of TPV transients that is determined by the recombination rate of the photoexcited charge carriers.[143] Herein the TPV lifetimes describe an overall rate of disappearance of photoexcited carriers through recombination in the whole device. These lifetimes, however, may be governed by multiple processes that dominate electrons meeting holes, such as re-injection of carriers from transport layers at lower light intensities.[146] The small-perturbation lifetime τ needs to be converted to the pseudo-first-order lifetime of total excess charge carriers $\tau_n = \delta\tau$, by a reaction order of δ to estimate recombination flux. The details of this conversion and the comparison of TPV lifetime is detailed in the experimental chapter and are discussed in ref [143]. The dependence of τ_n on Q, shown in **Figure 3.7**, demonstrate an approximate power-law correlation for all devices where $\tau_{n,0}$, δ and Q_0 are fitting constants, following equation 2.8. The results show that, for fixed charge density there is a modest increase (by up to a factor of ~3) in the total carrier lifetime as the crystallinity of the devices increases,

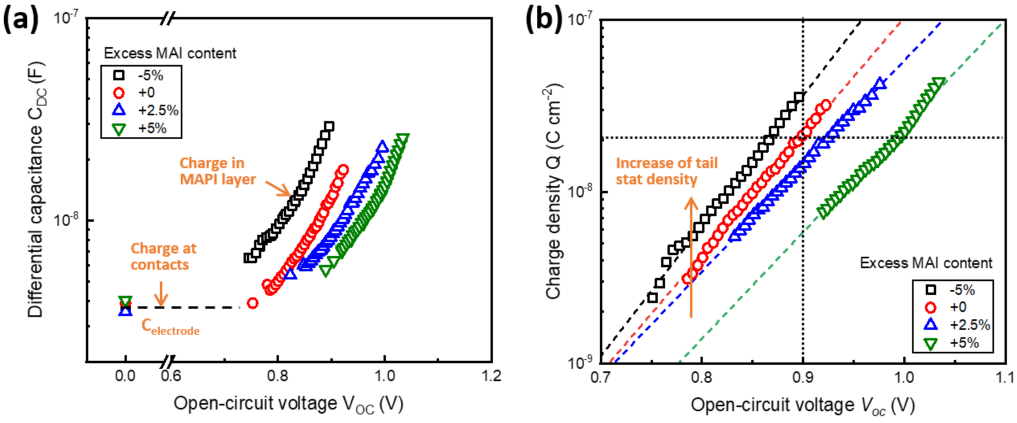

Figure 3.6 (a) Differential capacitance (C_{DC}) as a function of open-circuit voltage V_{oc} of solar cells comprising MAPI layers prepared with excess MAI contents of -5, +0, +0.25 and +0.5 mol % ($C_{electrode}$ is the electrode capacitance). **(b)** Charge density (Q) in the MAPI layers as a function of V_{oc}.

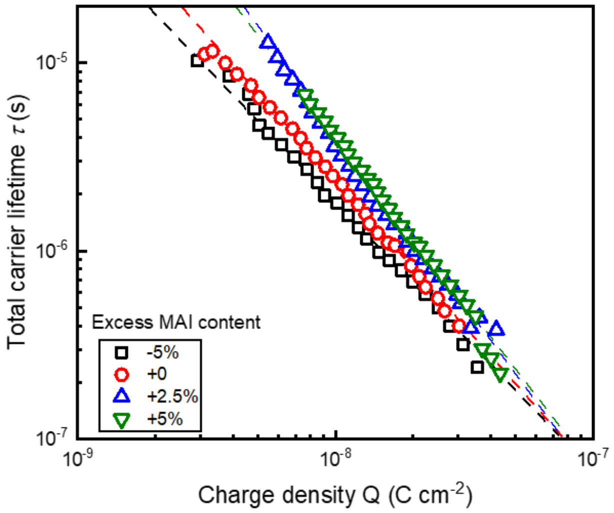

Figure 3.7 Total charge carrier lifetime (τ_n) in the various MAPI devices plotted against Q.

this suggests that less crystalline MAPI not only increases the density trap states, but also accelerates the rate charge carrier recombination via these traps. For example, at $Q = 2.1 \times 10^{-8}$ C cm^{-2}, τ_n for these devices are 1.03 μs (+5% MAI), 0.99 μs (+2.5 % MAI), 0.73 μs (0 %) and 0.63 μs (-5 %). This decrease in lifetime result in minor (~25 %) decrease in the amount of accumulated charged in the device at 1 Sun illumination. However, τ_n *vs* Q correlations show minimal change between +2.5 % MAI and +5 % MAI, indicating the recombination lifetime is no longer increased by further improvement of crystallinity and may be limited by other processes.

A question arising from examination of the measured lifetimes is that given recombination time constants on the order of 1 μs, which is long by solid state standards, why V_{OC} values approaching 1.2 V is not observed.[196] The V_{OC} values observed despite comparatively long lifetimes are likely to be related to the capacitive role of the shallow traps that are present in the device. Although the evidence suggests that recombination via these trap states becomes non-trivial, particularly in the less crystalline examples, the total rate of recombination is still likely to be dominated by

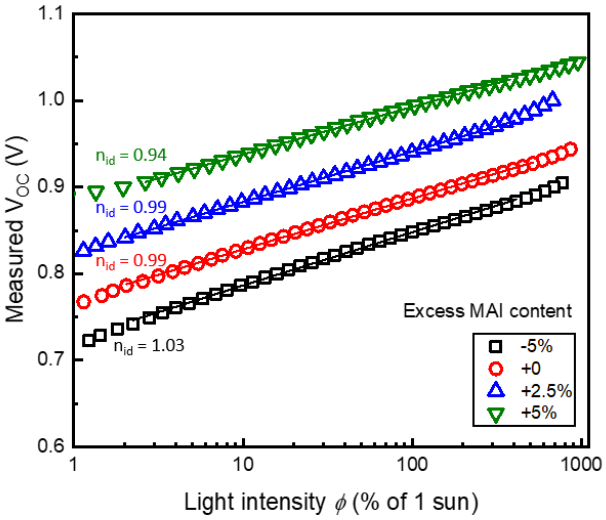

Figure 3.8 Measured V_{OC} as a function of light intensity and ideality factor obtained from a general fitting of V_{OC} vs light intensity.

the interfaces. Thus the exchange of charge between these trap states and the free conduction states can explain the comparatively slow recombination kinetics observed. As well as some direct contribution to recombination, the slow capacitive discharge from the traps (related to the idea highlighted by Kiermasch *et al.*[146] where the capacitive discharge is from the contacts) will also effectively slow the rate that charges reach interfaces of the device where the majority of recombination occurs.

The measured stabilized V_{OC} is plotted against light intensity in **Figure 3.8**, the enhancement in V_{OC} with increasing MAPI crystallinity is evident. The ideality factor n_{id} can thus be obtained by fitting the V_{OC} *vs* light intensity relationship, labelled on the figure, where it is apparent the values are close to unity for all devices. The deviation at higher light intensities is likely to be primarily due to an increase in the cell temperature which was not corrected for. Assuming that the recombination processes observed in this study are primarily mediated by trap states a value of $n_{id} \approx 1$ suggests that trap states either in the bulk or at the interfaces are energetically shallow relative to the conduction/valence bands,[76] it is also consistent with the strong interfacial recombination observed in devices with PEDOT:PSS contacts.[152]

3.4.5. Characterisation of Trap States

To explore further the nature of the electronic states within active layers, the charge carrier recombination in a reference MAPI film (1:1 ratio of MAI and PbI_2) film and the best-performing MAPI film (+5 % MAI) are characterized with PL spectroscopy PL. Steady-state PL spectra of active layer films are plotted in **Figure 3.8 a**, these show that the emission intensity is about 15 times greater in the +5 % MAI film than in the reference. The substantial increase of PL intensity strongly suggests a reduction in non-radiative Shockley-Read-Hall recombination processes, and the density of trap states in the MAPI film is largely reduced. The recombination dynamics of the two films are shown by the time-resolved PL (TRPL) decays in **Figure 3.9 b**, measured with time-correlated single-photon counting (TCSPC) and probed at peak position of PL emission spectra. The decays of both films are clearly biphasic, with a fast (ns) initial decay followed by a slower (circa 100 ns') decay. The biphasic features in PL decay dynamics have been intensively reported and studied for solution-processed perovskite films,[12,13,175,197] where the fast phase is assigned to charge carriers trapping into the non-

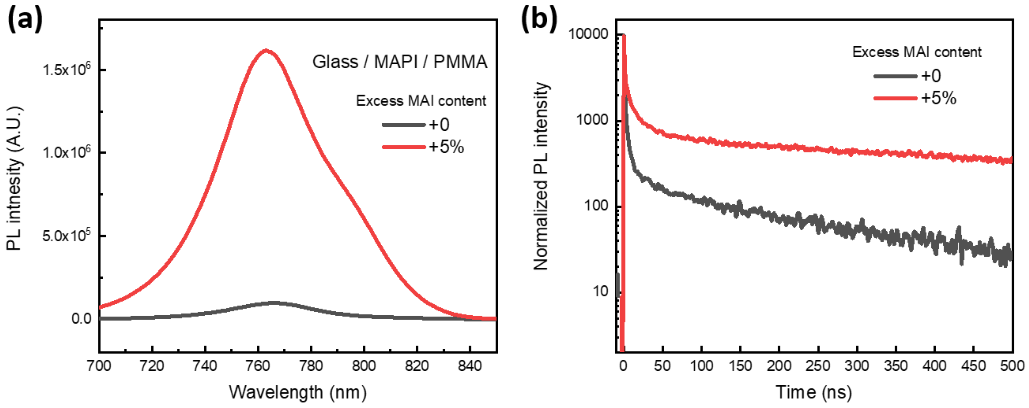

Figure 3.9 (a) Steady state photoluminescence (PL) emission spectra of MAPI films prepared with stoichiometric PBI2:MAI and + 5 mol % MAI. (**b**) Time-resolved PL decay spectra probed at 765nm where the stoichiometric MAPI film shows much larger amplitude of initial fast decay.

radiative trap states, and the slow phase assigned to subsequent recombination processes of the remaining carrier population. Here, decay dynamics for the reference, lower crystallinity film are faster compared to the + 5 %MAI excess film (biexponential decay times of 1.4 and 370 ns compared to 2.7 and 735 ns respectively), these differences in carrier recombination lifetimes are roughly consistent with the relative difference in TPV transients for the devices. More importantly, the lower crystallinity, reference MAPI films show a much larger amplitude of fast decay phase, suggesting a larger fraction of the initial population of photogenerated charge carriers are trapped, consistent with the higher Q_0 derived from the data in Figure 3.6. PL emission spectra of the MAPI films in contact with either the ETL and HTL are shown in **Figure 3.10**. The results show that the addition of a PCBM layer to the 1:1 film only quenches the PL by a factor of ~ 4 compared to > 40 times for the 5% MAI excess film, indicating poor electron collection efficiency by the PCBM in the presence of the trap states. Conversely, holes are collected at the PEDOT:PSS contact with a relatively higher efficiently than the electrons in the 1:1 film ~ 40 times. Thus suggests that electrons are the species primarily affected by shallow trap states.[177] A non-trivial fraction of the recombination will also occur by re-emission of charge back into the active layer or interface states following collection at the contacts.[146] The PL quenching measurements also indicate an overall higher radiative yield from the quenched +5 % MAI films

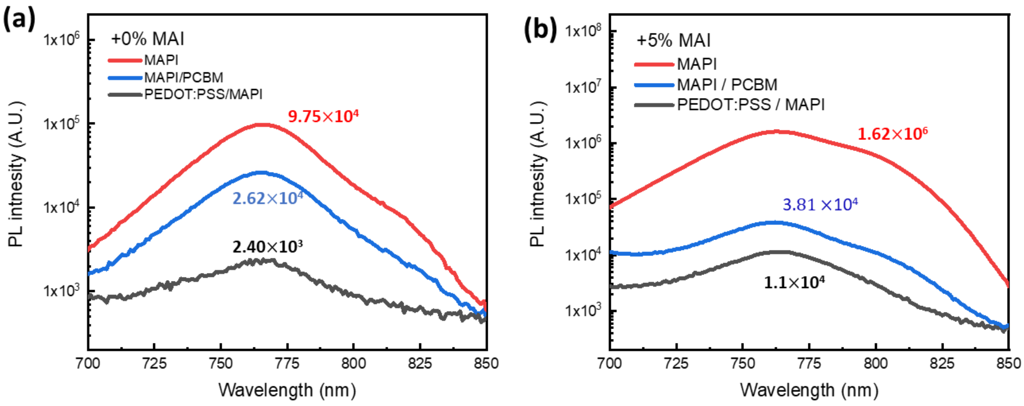

Figure 3.10 PL spectra of neat MAPI films and MAPI/PCBM, PEDOT:PSS/MAPI films.

relative to the quenched 1:1 films (~ 1.5 times for MAPI/PCBM and ~ 5 times for the MAPI/PEDOT:PSS). This indicates an overall higher probability that carriers will recombine radiatively in the low trap density films regardless of whether they can be collected at a contact, showing that reduction in trap-mediated recombination also prevails in the heterojunction interfaces as a substantial process to reduce V_{OC} loss.

3.5. Discussion & Conclusion

Trap-mediated recombination in solution-processed MAPI has been well studied, both with spectroscopy and microscopy.[11,197–199] The results in this chapter provide an insight into how these non-radiative losses in bulk MAPI can limit device Voc. The observation of Q *vs* Voc relationships in **Figure 3.6** implies at least one type of charge carrier is stored in an exponential of sub-gap states in the active layer or its interfaces. **Figure 3.11 a** schematically describes this difference in a flat-band energy diagram. The increase in the trap density in the less crystalline films also mediates recombination somewhat more rapidly at the expense of radiative pathways. Combined with our observation of device ideality close to unit, these electronic traps appear to be energetically shallow, which is consistent with the literature.[197,200] **Figure 3.11 b** schematically depicts the recombination of charge carriers via tail states, where photogenerated charge carriers are first trapped into the tail states, from which they may either de-trap or non-radiatively recombine. The variation in recombination time constant for a given photoinduced charge concentration might also be correlated with a change in the majority species carrier concentration in the MAPI. For some MAPI preparations, excess MAI, as well as improved crystallinity through annealing, has been shown to result in a reduction in the free electron concentration making the material more intrinsic,[201,202] which is expected to increase the free carrier lifetime. However, if this were the only effect induced by MAI then the PL efficiency is not expected to be as sensitive to MAI fraction as observed in **Figure 3.10**.

Recently Kiermasch *et al*. have reminded the community that the release of capacitively accumulated free charges can prolong the time-constants observed in TPV measurements.[146] Their study raises the possibility that the charge distribution observed in these devices is not accumulated within traps but simply corresponds to free charge within the active layer or contacts. It is noted that TPV time constants may also be prolonged by the same mechanism by the capacitive storage and released of charge from with trap states – an effect well documented for dye sensitized solar cells,[145] and also suggested to explain recombination rates in organic bulk heterojunction films without electrical contacts.[203] Although our results cannot definitively rule out the possibility that the Q vs V_{OC} distribution measured arise from a capacitive accumulation of free charges, the following factors make it an unlikely explanation for the observations. Our data show Q vs V_{OC} slopes of $m \approx 3$ but a steady state ideality factor of $n_{id} = 1$. In a perovskite device if only free charges were present it would expect $m = n_{id}$ when measured at steady state if no trapped charge is present.[76] A value of $m > 2$ cannot easily be explained by free charge carriers obeying Boltzmann statistics, particularly in devices where internal variations in electrostatic potential are screened by mobile ionic charge. Thus the value of $m \approx 3$, coupled with our PL observations, appears consistent with a shallow distribution of trap states.

This chapter addresses non-radiative losses which are likely to originate in the bulk of the perovskite, the V_{OC} (1.04V) and PCE (16.6%) achieved with our best cells are lower than the best reported device performances using similar perovskite absorbers *c.f.* $V_{OC} > 1.1$ V, PCE ~ 20 %. This is mainly attributed to our use of PEDOT:PSS as the HTL, which is associated with significant interfacial recombination,[152,166] compared with TiO_2-based conventional cells or inverted cells employing alternative HTLs.[188,189] It is observed that the total charge carrier lifetime as a function of charge concentration is not significantly altered with a change in MAPI crystallinity of +2.5% to +5% MAI, which may imply that interfacial recombination, either at PEDOT:PSS/MAPI or MAPI/PCBM interfaces became the limiting factor of carrier lifetime and thus the recombination flux in the whole device. Further increases of V_{OC} and PCE can be achieved by suppressing the interfacial recombination.[159,204] Thus, it is theorized that reducing non-radiative losses in bulk perovskite and at interfaces are two parallel methods towards high V_{OC} of perovskite solar cells.

It is shown that an increased density of tail states and increased non-radiative recombination are associated with reduced crystallinity of MAPI. Trap states are likely to be localised at crystallite surfaces or interfaces due to a break of bulk crystallite symmetry,[11] but additionally PL quenching is correlated with the presence of lattice defects *e.g.* halide vacancies.[116,205] The observed increase of X-ray diffraction intensity of MAPI films should describe an extension of order in the MAPI, and/or filling of lattice vacancies, which is schematically shown in **Figure 3.11 c**. In this study, improved MAPI crystallinity was achieved using the MAI-rich precursor solutions during processing, although MAI excess appears to increase trap densities using different fabrication protocols.[206] Mixed-cation lead mixed-halide perovskites have now surpassed conventional MAPI perovskites with reported PCE exceeding 20%,[162,174] the optoelectronic properties and phase stability of these materials is also highly dependent on crystallinity.[13,207] This is entirely consistent with our detailed studies that conclude that improving perovskite crystallinity is a crucial strategy to eliminating trap states.

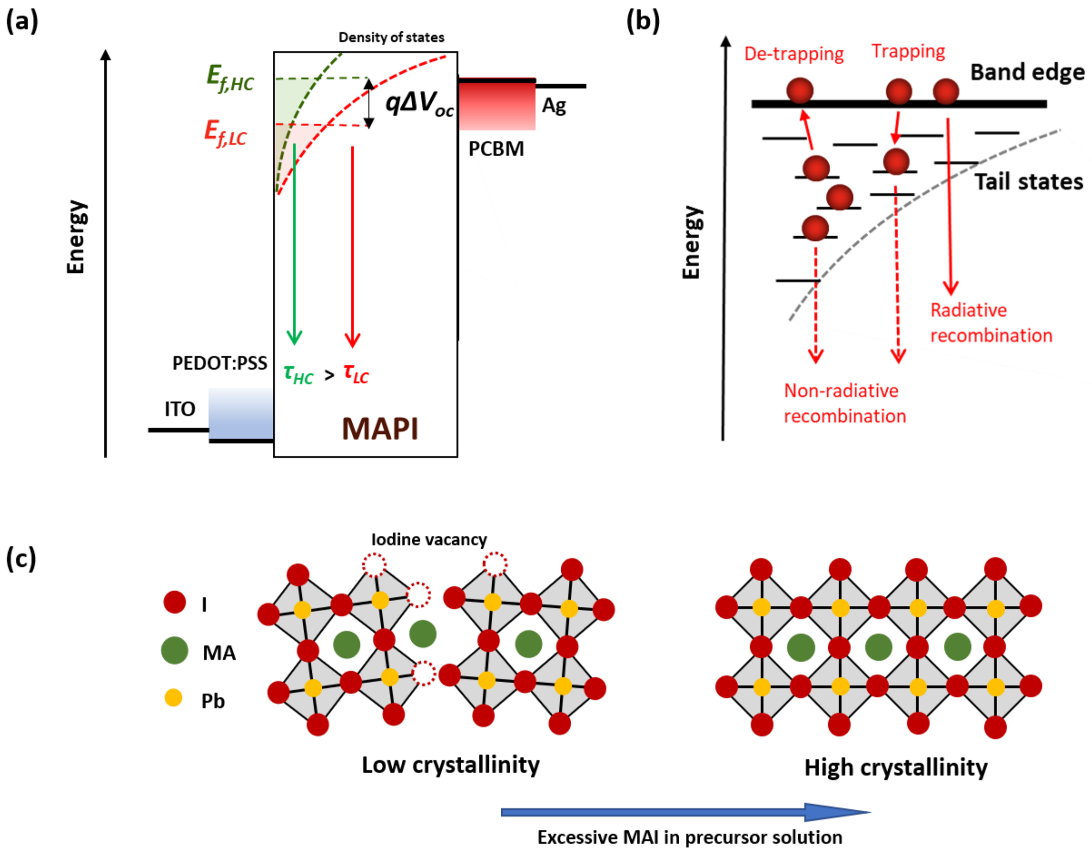

Figure 3.11 **(a)** Schematic illustration of band-tail broadening in a flat-band energy diagram of a perovskite solar cell, with high- and low-crystallinity MAPI, and with their corresponding electron quasi-Fermi levels, $E_{f,HC}$ and $E_{f,LC}$, and charge carrier recombination lifetimes, τ_{HC} and τ_{LC}. ΔV_{OC} is the V_{OC} loss due to increased tail state density. **(b)** Schematic depiction of charge carrier recombination via tail states, including charge trapping (also with de-trapping), non-radiative recombination from the tail states a radiative recombination from band edges. **(c)** Schematic illustration indicating the improvement in MAPI crystallinity.

4. Probing and Controlling Microstructural Defects in Thin-film Perovskites and Its Impact on Solar Cell Performance

4.1 Declaration of Contributions

The results presented in this chapter formed the basis of reference [208]

Claire Burgess carried out all the transmission electron microscope measurements.

Chieh-Ting Lin aided with solar cell optimization.

Flurin Eisner aided with external quantum efficiency (EQE) measurement.

Jinhyun Kim and Shengda Xu aided spectroscopic measurement.

Hongkyu Kang aided with data processing and analysis.

4.2 Abstract

In this chapter, previously unobserved nanoscale defects residing within individual grains of solution-processed MAPI thin films is identified. Using scanning transmission electron microscopy (STEM) I identify these defects to be inherently associated with the established solution-processing methodology and introduce a facile processing modification to eliminate these defects. Specifically, defect elimination is achieved by co-annealing the as-deposited MAPI layer with the electron transport layer (PCBM) resulting in devices that significantly outperform devices prepared using the established methodology – with power conversion efficiencies increasing from 13.6 % to 17.4 % for devices with PEDOT:PSS as hole transport layers. The use of TEM correlates the performance enhancements to improved intra-grain crystallinity and show that highly coherent crystallographic orientation results within individual grains when processing is modified. Detailed optoelectronic characterisation reveals that the improved intra-grain crystallinity drives an improvement of charge collection and a reduction of PEDOT:PSS/perovskite interfacial recombination. The results of this chapter suggest that the microstructural defects in MAPI, owing to a lack of structural coherence throughout the thickness of thin film are a significant cause of interfacial recombination.

4.3 Introduction

Photovoltaic cells reliant on metal-halide perovskite active layers, the so-called perovskite solar cells (PSCs), have had a tremendous impact on emerging photovoltaic technologies since their first introduction.[44] The remarkable power conversion efficiencies (PCEs) demonstrated,[209] combined with the relative ease of fabrication and low materials costs,[210] have fuelled intensive research of these emerging renewable energy platforms. As the community moves towards developing a better understanding of the key operational and lifetime issues of PSCs, and ultimately to commercial deployment, it is necessary to derive a deeper understanding of the fundamental material properties that play a critical role in determining device performance and lifetime. These factors include phenomena occurring at the grain boundary regions,[199] chemical defects,[2] trap state,[11,198] crystallinity,[211] and the presence of secondary phases.[179,185]

When considering the rapid evolution of PCE that has been demonstrated in PSCs it is apparent that improvements in fabrication techniques and the development of standard growth procedures have played key roles. However, the engineering of controlled device architectures is also critical.[212] To date three main device architectures have been proposed, namely the i) mesoporous systems,[213] ii) conventional (n-i-p) planar[45,214] and iii) inverted (p-i-n) planar structures.[169,215] The best performing devices reported thus far have been demonstrated using both mesoporous and planar n-i-p structures.[157] In both cases the mandatory high temperature processing of metal oxide electron transport layers renders such architectures incompatible with future flexible devices.[216] As an alternative, inverted architecture (p-i-n) devices that rely on low-temperature solution processable charge transport layers, and are thus compatible with flexible substrates, are attractive - more so owing to the negligible J-V hysteresis observed.[217,218] Poly(3,4-ethylenedioxythiophene) polystyrene sulfonate (PEDOT:PSS) is commonly used as a hole transport layer (HTL), due to its charge selective nature, high optical transparency and low temperature (< 150 °C) processability.[189,219] On the opposite side of the device fullerene derivatives such as [6,6]-phenyl C_{61} butyric acid methyl ester (PCBM) are commonly incorporated as electron transport layers (ETL). Despite the relative ease of processing afforded by inverted devices, the attainable PCEs are somewhat lower than both mesoporous and planar n-i-p analogues.[190] In particular the maximum attainable open-circuit voltage (V_{OC}) with PEDOT:PSS, normally no greater than 1 V,[220] is a key performance barrier, although the loss of V_{OC} can be partially overcome by either inserting or replacing PEDOT:PSS with other polymeric hole transport layers.[218]

Interestingly, the development of solvent engineering methods has allowed pinhole-free, uniform and continuous perovskite thin films to be prepared - which is a crucial step to achieve high PCE with inverted planar devices. Typically, these methods involve introducing a stream of antisolvent (*e.g.* toluene,[184] diethyl ether,[84] or chlorobenzene[221]) which is dripped onto the spinning substrates with precursor solution, forming an intermediate film containing a complex perovskite/solvent molecular mixture. The final steps of film formation involve a simple thermal anneal, typically at around 100 °C, to remove the remaining solvent and fully crystalize the perovskite films. Such annealing may also be used to controllably induce the formation of secondary phases that may be beneficial to device performance.[185] The established method for device fabrication involves sequential processing of the individual layers in the device. Following deposition of the perovskite active layer and annealing,[169,184] the charge selective interlayer *e.g.* the fullerene layer is subsequently processed. In this chapter modifications of this protocol are considered, specifically depositing the PCBM layer onto non-annealed MAPI films and then co-annealing. This simple modification of the processing has resulted in an enhancement of the resultant device performance, with measured average PCEs increasing from 13.6 % in conventionally processed PSCs to 17.4 % using the modified processing.

Whilst previous research has addressed the *inter-grain* optoelectronic homogeneity in the lateral dimension, *i.e.* parallel to the substrate,[197,199] this chapter focuses on the *intra-gain* crystallographic continuity along the charge-transport direction, *i.e.* vertical to the substrate. The origin of the investigations stems from highly disordered regions observed by high-resolution transmission electron microscopy (HRTEM) near the top (MAPI-air) interface in conventionally processed active layers. In contrast, when the modified fabrication route is employed, highly ordered MAPI domains that extend from the HTL to the ETL are observed. Such modifications effectively eliminate microstructural defects in MAPI film, leading to reduced interfacial recombination and improved V_{OC} (by approximately 200 mV). The results of this chapter highlight the critical role of MAPI thin film quality along the charge-transport direction, *i.e.* perpendicular to the substrates.

4.4 Experimental Results

4.4.1. Modification on Thin-film Processing

Figure 4.1 shows a schematic illustration of the conventional and modified deposition processes. In both cases toluene is added to the as-deposited perovskite as an anti-solvent, forming intermediate films containing a mixture of perovskite precursors and solvent molecules. Conventionally, crystallinity is induced by thermally annealing these intermediate films prior to depositing the fullerene layer. Here PCBM layer is processed directly onto the intermediate film, and thermally anneal the bi-layer structure - thus MAPI is crystallized beneath the PCBM over layer.

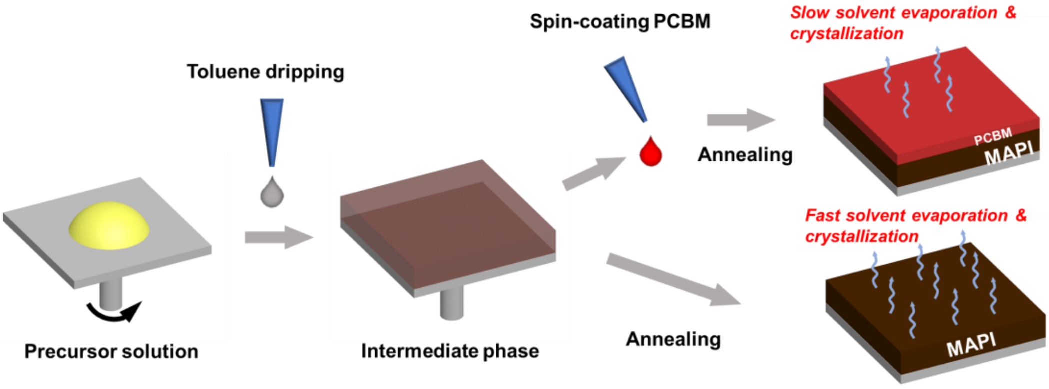

Figure 4.1 Schematic illustration of conventional fabrication route and modified fabrication route of MAPI/PCBM bi-layers.

4.4.2. Characterisation of Microstructural Defects

Scanning Transmission Electron Microscopy

Initially scanning transmission electron microscopy (STEM) is used to image the cross-section of the ITO/PEDOT:PSS/MAPI/PCBM structures prepared using focused ion beam (FIB) milling.[222] The sample preparation, imaging mode and beam damage are discussed in the experimental chapter. Whilst beam damage in STEM is minimal some damage can be observed in conventional TEM when extended beam exposure occurs, thus affording control of the imaging and the collection of high-quality, artefact free

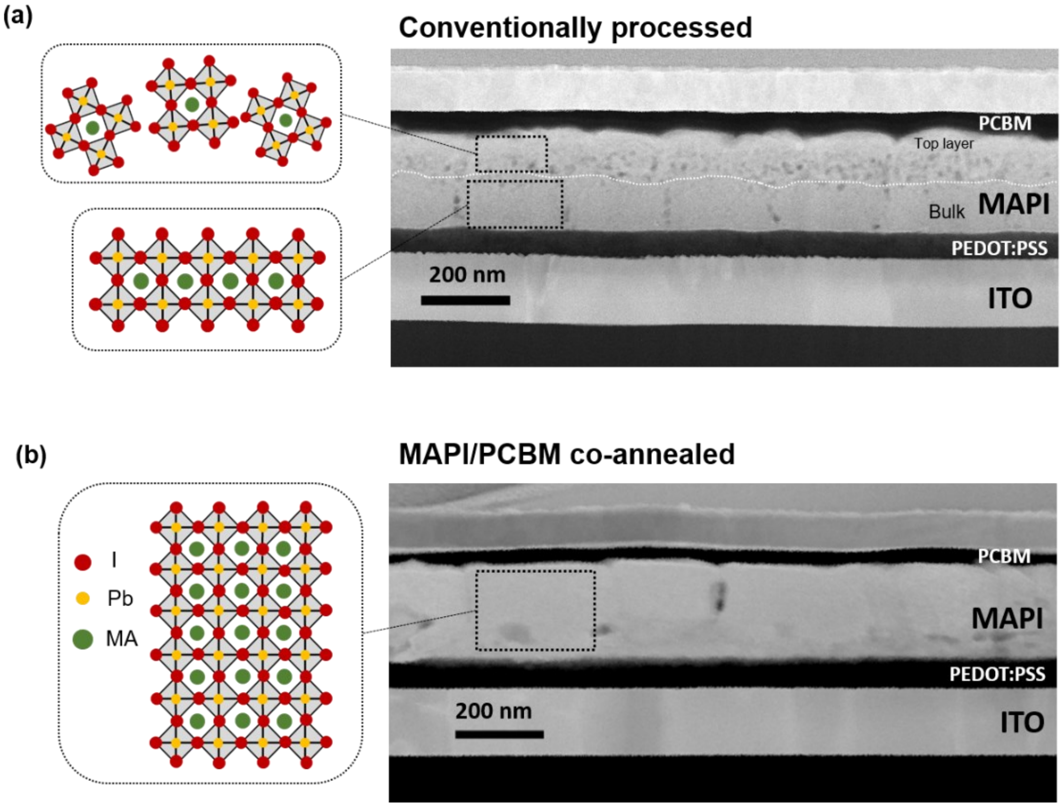

Figure 4.2 Scanning transmission electron microscopy (STEM) images (right) and schematic demonstration of the MAPI microstructure (left) in the bulk and top layer of **(a)** the conventionally processed device, and **(b)** the co-annealing processed device.

images. The dark-field STEM images of complete stacks of conventional and co-annealed devices are shown in **Figures 4.2 a** and **4.2 b**. In general, the MAPI films prepared by both routes are polycrystalline, with single grains extended vertically *i.e.* between the ETL and HTL separated by lateral grain boundaries as reported previously[185]. Owing to the excellent image contrast provided by STEM a disordered region beneath the PCBM interface is clearly observed in the MAPI layer, where dispersed dark regions approximately 5 nm in diameter, indicative of reduced material density *i.e.* voids, are seen concentrated near the MAPI/PCBM interface in the conventionally processed devices (**Figure 4.2 a**). In contrast, such features are absent in the co-annealed films (**Figure 4.2 b**).

Selected Area Bright-Field Image

To investigate the structure of the MAPI grains in more detail high-resolution conventional transmission electron microscopy (HRTEM) is employed. In **Figures 4.3 a - b** low-magnification images showing cross-sections of the conventional and modified processing device stacks are present. Due to the nature of HRTEM imaging *i.e.* the image is formed with both non-diffracted and diffracted electrons that pass through the sample, image contrast is reduced and thus the dark features observed by STEM cannot be discerned.[223] Selected area electron diffraction (SAED) patterns of both cross sections are shown in **Figures 4.3 c - e**. These patterns are comparable to reported MAPI single crystal SAED patterns,[224] with the elongation of the individual diffraction spots indicating a preferential orientation of crystallites with a slight *intra-grain* misalignment. To image the associated crystalline regions in the cross section, the objective aperture is placed around one of these diffraction spots, giving rise to the dark-field images identical in location to the HRTEM images, shown in **Figure 4.3 f** for conventionally processed device and **Figure 4.3 g - h** for two adjacent grains for a co-annealed device. Importantly, the bright areas shown here pinpoint the exact location where the single-crystal diffraction patterns are generated, identifying coherent crystallographic orientation through the grain structure. Hence, the crystallographic coherence inside single MAPI grains can be examined. In both processing methods the lateral extension crystallinity is limited by the grain boundaries and adjacent grains tend to show subtly modified orientations. However significant differences in the vertical crystallinity can be readily observed. From **Figure 4.3 f** it is apparent that the extended region of crystalline coherence extends only partially through the film thickness and the area near MAPI/PCBM interface where the voids were observed in STEM (**Figure**

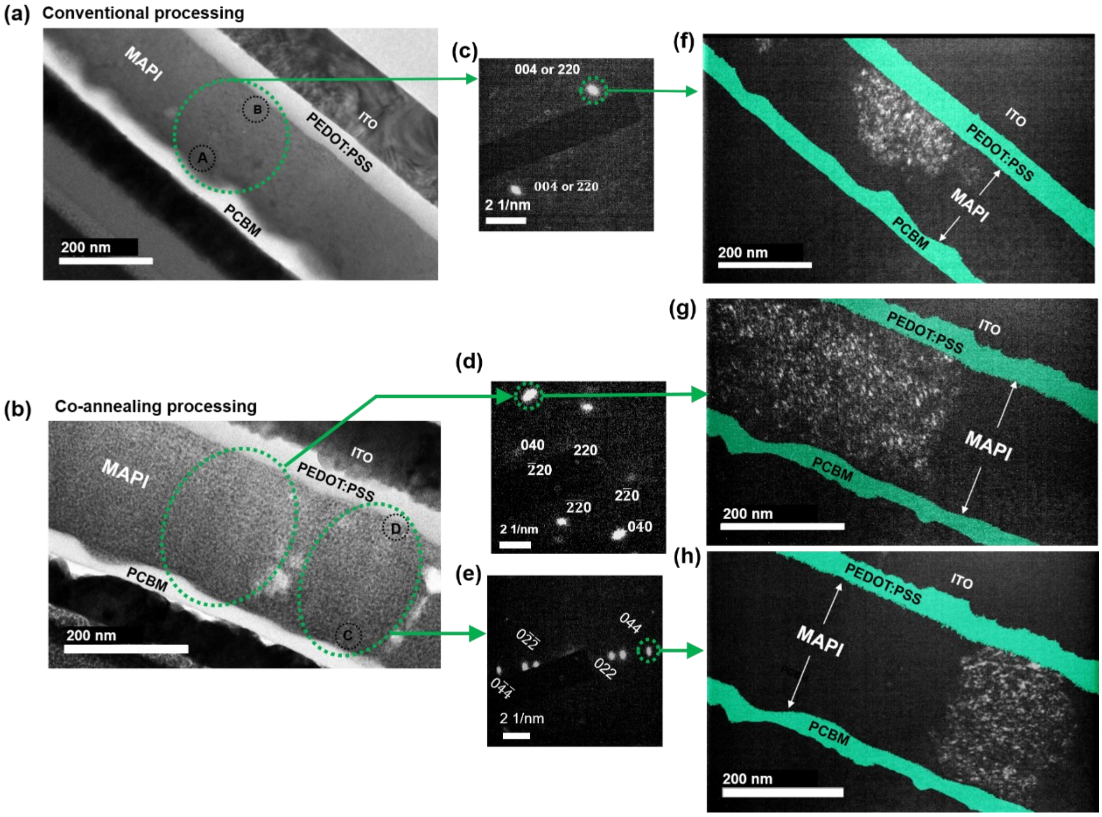

Figure 4.3 (a), (b) Transmission electron microscopy (TEM) images of device prepared through conventional processing (a) and through co-annealing processing device (b). **(c) – (e)** Selected area electron diffraction (SAED) patterns of MAPI in the circulated areas in figure a and b. **(f) – (h)** Localized dark-field images formed with one of the diffraction dot, marked in figure c – e, for conventional processed device (f) and co-annealing processed device (g and h). The green colour is added to indicate the location of charge selective interlayers.

4.2 a) appears dark and obviously has no such order. Between **Figures 4.3 g - h** there is a grain boundary running perpendicular between the charge selective interlayers, separating the two adjacent MAPI grains. However, in both grains there is a clear orientational alignment that spans the entire active layer thickness, which means along the charge transport direction MAPI is either single crystal, or the crystallites are aligned in unified direction. This is consistent with the observed cross-sectional uniformity seen in the STEM image (**Figure 4.2 b**).

High-Resolution TEM

The HRTEM images, **Figures 4.4 a - d**, all show clear lattice fringes in the MAPI films

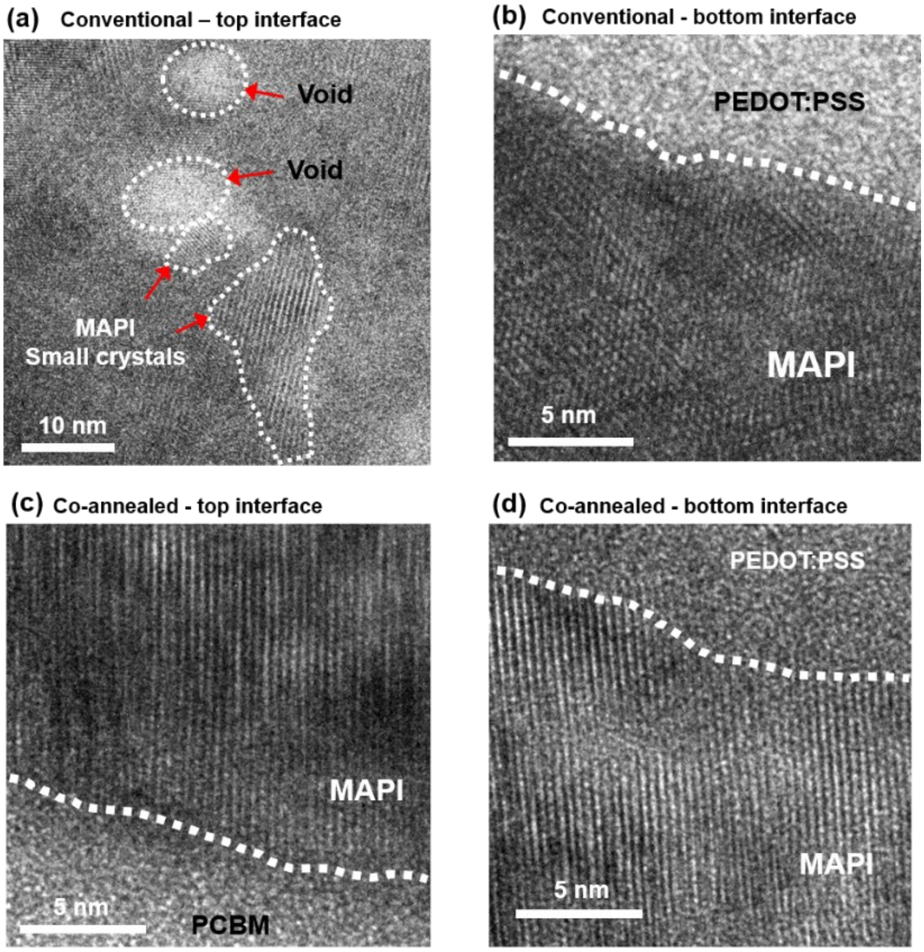

Figure 4.4 HRTEM images of lattice fringes at **(a)** top (MAPI/PCBM) and **(b)** bottom (PEDOT:PSS/MAPI) interfaces of the conventionally processed device, and at **(c)** top and **(d)** bottom interfaces of the co-annealed devices. These areas are marked as A-D in figure 4.3a and 4.3b, respectively.

both at top (MAPI/PCBM) and bottom (PEDOT:PSS/MAPI) interfaces. However, there is a distinct difference between the devices with the two processing routes. In **Figure 4.4 a**, obtained from the top interface of conventionally processed device (marked A in **Figure 4.3 a**), a disruption in ordering of the crystalline regions is seen, featuring small-size MAPI crystals with short lattice fringes amongst the voids. Within the same MAPI film, however, **Figure 4.4 b** (region B in **Figure 4.3 a**) shows long-range order at the bottom interface, which is consistent with the observation in the corresponding dark-field image (**Figure 4.3 f**) that lower portion of conventionally processed MAPI films consists of a single-oriented grain. In contrast, the images of co-annealed device, **Figures 4.4 c - d**, show excellent crystallinity of MAPI film across the film thickness, manifested by the regular, long-range lattice fringes at both top and bottom interfaces corresponding to areas marked C and D in **Figure 4.3 b**.

X-ray Diffraction

Using X-ray diffraction (XRD) to investigate the phase and structure of the MAPI films prepared by the two processing routes, again an obvious difference between the crystallinity of the films is found, **Figure 4.5 a**. Here the intensity of the {110} peaks significantly increases in the co-annealed films, indicating a preferential orientation (texture). From these data it is evident that the overall crystallinity of MAPI has been enhanced in the process of co-annealed films. Shown in **Figure 4.5 b** the position of the {110} diffraction peaks shifts from 14.17°(2θ) for conventionally processed film to 14.24°(2θ) for co-annealed film showing a decrease of lattice plane spacings, which may be related with restoration of long-range orders of MAPI crystals leading to removal of lattice defects or release of lattice strains. Additionally, the full width at half-maximum (FWHM) values for the (001) diffraction peaks are measured to be 0.10°(2θ) and 0.21°(2θ) for the co-annealed and conventionally processed films respectively. Such a reduced FWHM qualitatively indicates an increase in crystallite size.

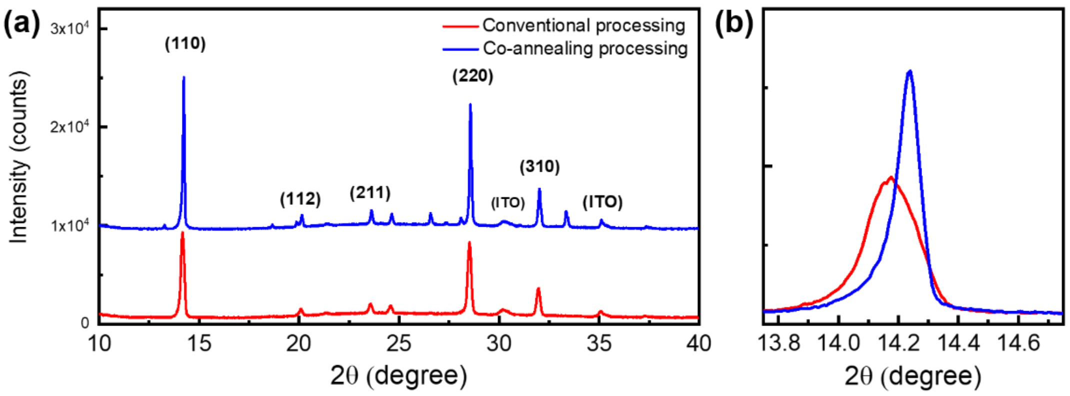

Figure 4.5 (a) X-ray diffraction patterns of MAPI film in conventionally processed device and co-annealing processed device. **(b)** Magnified (110) diffraction peaks for conventionally processed and co-annealed MAPI films.

The above observations highlight an issue of microstructural inhomogeneity in MAPI films processed using the conventional methodology, where polycrystalline grains consist of a highly-ordered region in proximity to the PEDOT:PSS interface and a highly disordered region (approximately 30-40 % of the film thickness) near the PCBM interface. In the co-annealed devices, the orientation coherence extends throughout the entire film thickness, thus it is observing either single crystalline grains or highly orientated smaller crystallites inside what appears macroscopically to be a single grain. Such a difference is schematically illustrated in **Figure 4.2 a** and **4.2 b**. The defects that appear in the conventionally processed films have a profound influence on the measured device performances and the introduction of these features may be considered as a hindrance to charge transport in the MAPI films. It is believed that these structural inhomogeneities arise owing to non-uniform solvent evaporation rates, where evaporation of solvent near the MAPI-air interface in conventionally processed cells occurs rapidly, inducing the observed defects. For the co-annealed films, the PCBM layer may be slowing down but homogenizing solvent evaporation rate between top and bottom of the as-cast MAPI film, and subsequently reducing the rate of MAPI crystallization allowing time for more controlled crystal growth and improved interaction between neighbouring crystallites. It is noteworthy that the voids in MAPI film observed using STEM imaging (**Figure 4.2 a**) cannot be discerned in conventional TEM imaging (**Figure 4.3 a**), and thus are unlikely to be observed in the established cross-sectional SEM images typically used in literature to show device structures; It is however believed that their occurrence may be a general feature of films prepared using the established anti-solvent dripping method and normal hot-plate thermal annealing.

Control of Beam Damage

Investigation was done on a separate cross-sectional sample to confirm perovskite is stable and does not greatly change under scanning TEM (STEM) mode within an imaging session. Between **Figure 4.6 a-b** the sample was exposed to the STEM electron beam for 30 minutes but does not show obvious change in overall morphology. The dark linear feature indicated is a perovskite grain boundary (appears darker due to the lower density at grain boundaries), which can be still clearly seen in the post-exposure image. The same location was then exposed in conventional TEM mode for 30 minutes, and in this situation the electron beam gradually affected the appearance of the MAPI cross section. The location was re-imaged in STEM mode (**Figure 4.6 c)** and, for example, the grain boundary is no longer clear. However, even after prolonged conventional TEM exposure, using the same dark field imaging protocol used in figure 2 in the main text remains a valid and valuable method to investigate perovskite grain locations. **Figure 4.6 d** shows the high resolution conventional TEM image of the same MAPI grain in Figure S1 c, i.e. the MAPI grain after 30 minutes exposure to TEM electron beam. The corresponding selected area electron diffraction pattern in **Figure 4.6 e** shows a clear single-crystal-like pattern and when the objective aperture is used to select a diffraction spot (corresponding to 220 or 004 diffraction, marked by green circle), the dark field TEM image in **Figure 4.6 f** is formed. This clearly shows a bright area i.e. the perovskite grain giving rise to the diffraction pattern, which is bordered by the same location as the originally visible grain boundary. Therefore, despite changes in microscopic appearance, the overall crystal structure of the perovskite remains unchanged during these investigations.

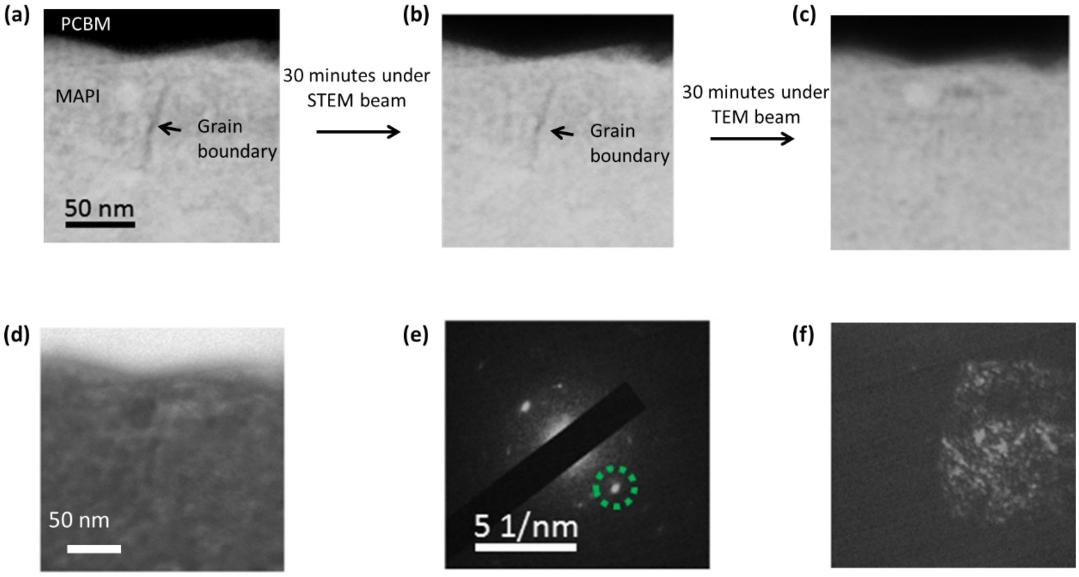

Figure 4.6 Dark field STEM image of a specific area of perovskite film **(a)** taken immediately, **(b)** after 30 minutes under STEM beam and **(c)** after a further 30 minutes under conventional TEM beam. **(d)** High resolution TEM image of the same sample area after the 30 minutes TEM beam exposure and **(e)** corresponding SAED pattern and **(f)** dark field image formed by the circled diffraction dot.

4.4.3. Performance of Solar Cells

In **Table 4.1** the influence of MAPI film thickness on device performance is listed. The thickness variation is achieved by modulating the concentration of the PbI_2 and methylammonium iodide (MAI) precursors over the range 0.6 – 1.4 mol dm^{-3}. **Figure 4.7 a** shows the variation of PCE with perovskite film thickness processed methodologies Both the conventional and co-annealing methods produce MAPI films of comparable thickness for a given precursor concentration. The data reveal that for the two processing routes there is both a difference in the performance at a specific thickness, and a difference in the thickness corresponding to the respective peak performance. The devices prepared using our co-annealing route are observed to perform best (highest PCE) with a MAPI active layer thickness of ~240 nm, with further thickness increases compromising J_{SC} and FF. It is speculated that such losses may be due to incomplete conversion of thick films under the PCBM capping layer. In contrast

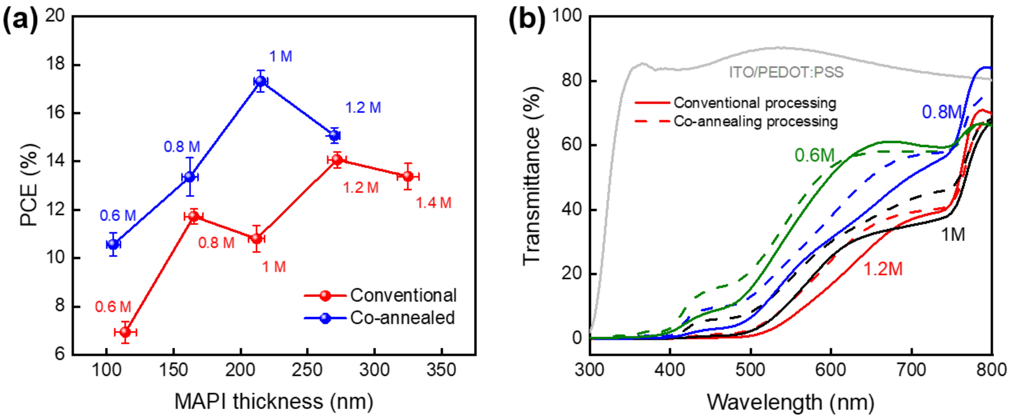

Figure 4.7 (a) Power conversion efficiency (PCE) of low-temperature-processed solar cells prepared from conventional and co-annealing routes as a function of MAPI thickness. The concentration of precursor solution (mol L^{-1}, denoted as M) is labelled beside the data point. **(b)** Transmittance spectra of full devices through conventionally processing (solid lines) and co-annealed processing (dashed lines), with MAPI prepared with different solution concentrations that are labelled on the figure.

the conventionally processed devices generally improve in PCE up to an active layer thickness of ~230 nm, above which V_{OC} and FF loses impact performance. In general, the observed PCE improvement originates mainly from the substantial improvement in V_{OC}, approximately 150-200 mV, at comparable MAPI thicknesses, suggesting a clear reduction of intrinsic photovoltage losses when the modified processing is employed.[225,226] Optical transmittance spectra (without Ag electrodes) **Figure 4.7 b**, show otherwise slightly increased transmittance of the co-annealed devices compared with those processed using the established method at comparable film thicknesses. Clearly the recombination losses during charge extraction are reduced owing to the process induced MAPI modification in the charge-transport direction. Interestingly, the co-annealed devices, at comparable MAPI thicknesses, consistently outperforming the devices prepared by the conventional processing whilst being more transparent, highlighting the opportunities for this processing route for the exploration of semi-transparent cells.

Table 4.1 Photovoltaic parameters of solar cells prepared from conventional and co-annealing routes comprising MAPI of different thickness, measured from the best 5 pixels of the devices from a single batch.

	Solution concentration (M)	MAPI thickness (nm)	J_{SC} (mA cm^{-2})	V_{OC} (mV)	FF (%)	PCE (%)
Co-annealing processing	0.6	105	15.4 ±0.6	904 ±3	75.4 ±1.0	10.5 ±0.5
	0.8	165	18.1 ±1.5	1004 ±5	73.4 ±2.9	13.4 ±0.8
	1.0	230	21.9 ±0.7	1022 ±3	76.8 ±1.4	17.2 ±0.4
	1.2	270	20.7 ±0.7	1040 ±4	70.0 ±1.2	15.1 ±0.3
Conventional processing	0.6	114	13.4 ±1.0	716±6	72.0±1.1	6.9±0.4
	0.8	165	19.6 ±0.5	813 ±3	73.3 ±1.4	11.7 ±0.3

	1.0	213	16.9 ±0.6	855 ±2	74.6 ±1.5	10.8 ±0.5
	1.2	272	20.1 ±0.4	894 ±4	75.8 ±1.4	13.6 ±0.3
	1.4	325	21.2 ±0.8	855 ±2	73.6 ±1.0	13.3 ±0.5

Figure 4.8 a shows typical current-voltage (J-V) curves of the low-temperature (<150°C) processed ITO/PEDOT:PSS/MAPI/PCBM/LiF/Ag devices comprising of conventionally processed (270 nm) and co-annealed (230 nm) MAPI layers. The data were obtained in forward and reverse scan directions, from open circuit to short circuit and *vice-versa* at a scan rate of 50 m V/s under AM1.5 illumination (1 Sun). Both sets of devices show minimal J-V hysteresis. In these two typical devices the V_{OC}, short-circuit current density (J_{SC}), fill factor (FF) and PCE of the conventionally processed device were determined to be 0.89 V, 20.0 mA/cm^2, 0.76 and 13.6 % respectively compared with 1.02 V (+ 16 %), 22.2 mA/cm^2 (+ 11 %), 0.76 (+0 %) and 17.4 % (+ 28 %) for the co-annealed device. **Figure 4.8 b** shows the external quantum efficiency (EQE) spectra of the two typical devices. The integrated J_{SC} values from EQE spectra

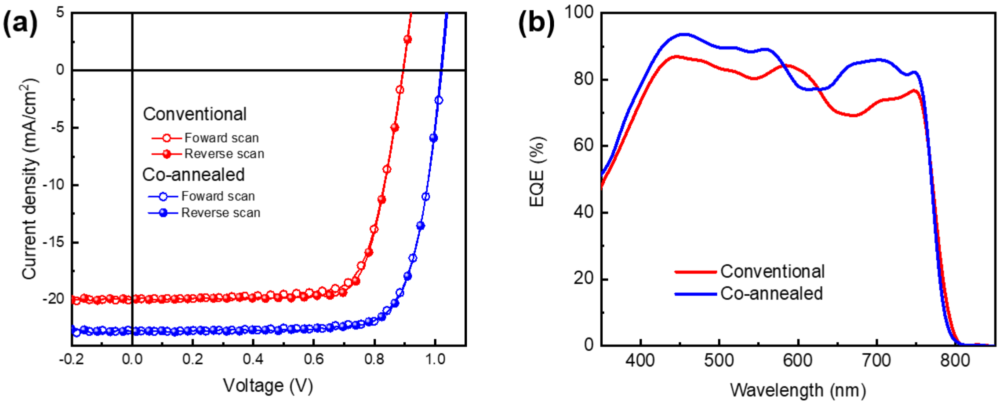

Figure 4.8 (a) Current density-voltage (J-V) plot of low-temperature-processed PEDOT:PSS/MAPI/PCBM/(LiF)Ag solar cells prepared from conventional and co-annealing routes at their optimal thickness. **(b)** External quantum efficiency spectra of the two devices.

are determined to be 21.7 mA/cm^2 (co-annealed) and 19.8 mA/cm^2 (conventional). The external quantum efficiency (EQE) spectra (**Figure 4.7 b**) for films prepared by both routes show a near identical absorption onset at ~780 nm, confirming minimal changes in optical bandgap and absorption and thus the improvements observed are attributed to reduced recombination losses, likely owing to elimination of microstructural defects. **Figure 4.9** plots the distribution of J_{SC}, V_{OC}, FF and PCE obtained from some 14 devices over 4 batches. A PCE value of 13.6% is typical for conventionally processed cells, however a PCE of 17.4% for the co-annealed devices is comparable with the best reported devices adopting PEDOT:PSS and PCBM as charge transport layers.

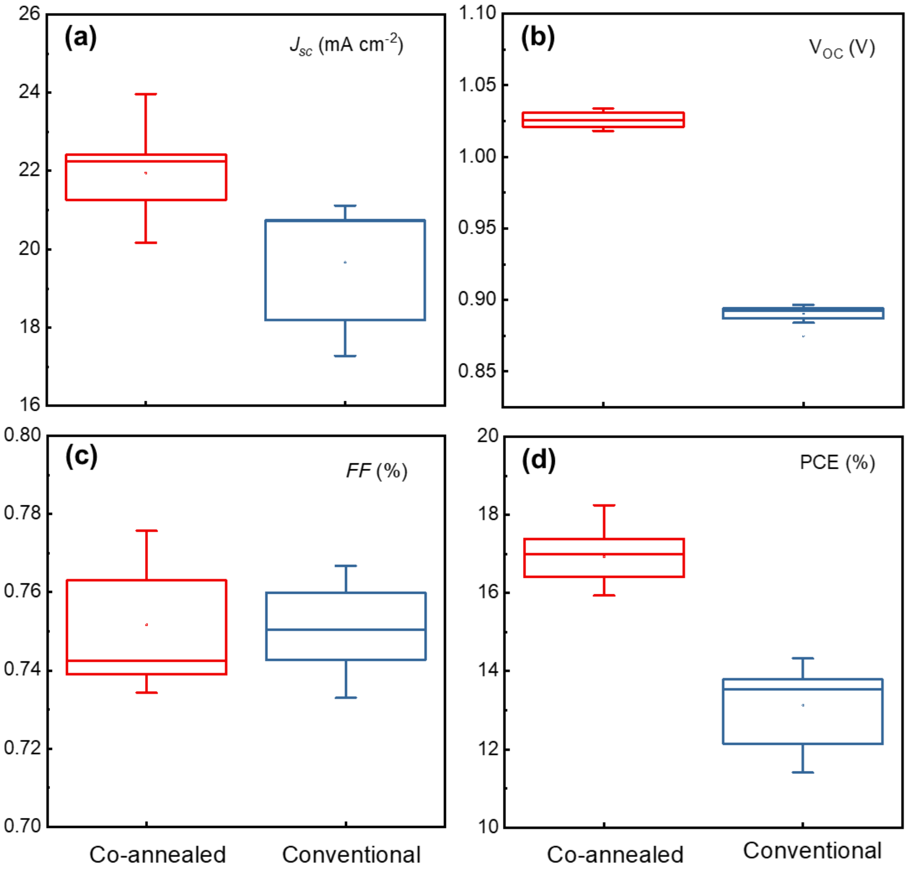

Figure 4.9 Statistical distribution of **(a)** short circuit current (J_{SC}), **(b)** open-circuit voltage (V_{OC}), **(c)** fill factor (*FF*) and **(d)** power conversion efficiency (PCE) of devices with conventionally processed MAPI and co-annealed MAPI, obtained from some 14 devices in four batches.

4.4.4. Optoelectronic Characterisation

J_{SC} and V_{OC} versus Light Intensity

To support these conclusions, the recombination mechanisms in the two devices is considered by studying the dependence of J_{SC} and V_{OC} on light intensity. J_{SC} is found to increase with light intensity (Int) according to a power-law relationship: $J_{SC} \propto \mathrm{Int}^{\alpha}$, shown in the inset figure of **Figure 4.10 a**. The derived power-law component α is plotted against light intensity in **Figure 4.10 b**. Deviation from a linear J_{SC}-Int

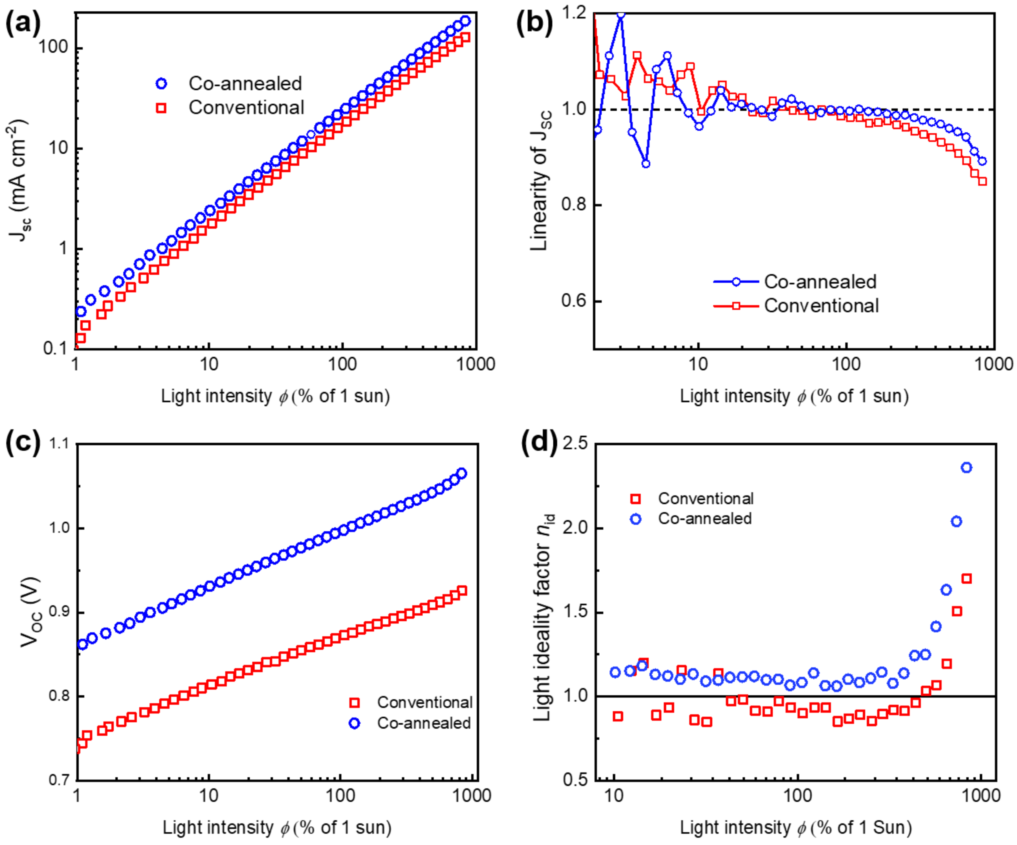

Figure 4.10 (a) Measured J_{SC} as a function of light intensity. **(b)** Linearity of J_{SC} with light intensity. **(c)** Measured V_{OC} as a function of light intensity. **(d)** Light ideality factor derived from V_{OC} vs light intensities relationship.

dependence, *i.e.* $\alpha<1$, is reported to suggest bimolecular recombination of electrons and holes in the device at short circuit.[227] It is evident that our processing modification result in improvement of linear J_{sc}-lnt dependence, particularly at higher light intensities, indicating a suppression bimolecular recombination loss and an enhancement of charge extraction and collection at short circuit – this is consistent with the improved crystallographic coherence along the charge-transport direction.

The recombination at open circuit is considered in terms of ideality factor (n_{id}). At open circuit there is no net current flow through the cell and the voltage losses due to series/parasitic resistance are minimised.[150] **Figure 4.10 c** shows the measured V_{OC} as a function of light intensity for both devices, and **Figure 4.10 d** shows the light ideality factor n_{id} deviated from equation (1). The two traces remain relatively constant from 0.1 sun up to approximately 4 sun, but differ dramatically at higher light levels. The n_{id} of conventionally processed devices is just less than 1, particularly near 1 sun, whereas within the same illumination range n_{id} of co-annealed devices is around 1.2.

A general interpretation of n_{id}, considering the recombination mechanisms in a solar cell, is that $n_{id} \approx 1$ indicates recombination of free electrons and holes, $n_{id} \approx 2$ suggests recombination of free electrons and trapped holes, or *vice versa*; and when $n_{id} < 1$ surface recombination dominates.[150] That being said, rather than indicating a dominance of radiative free-carrier recombination, the value of $n_{id} \approx 1$ for our conventionally processed devices more reasonably suggests surface recombination dominance,[196] because the V_{OC} of these devices (0.89 V) is substantially lower than the radiative limit of MAPI (~ 1.3 V). The increase of n_{id} from 1 to 1.2 for the co-annealed devices then suggests Schottky-Read-Hall recombination in bulk perovskite is becoming more dominant due to a reduction of surface recombination,[152] or due to reduced recombination via trap states that are localised in the vicinity of the interfaces. This is consistent with our previous analysis of similar perovskite solar cells where n_{id} decreases < 1 due to surface recombination.[110,148]

Charge density and recombination lifetime

Figure 4.11 a plots a measured value *n* [cm^{-2}] as a function of V_{OC}, where each point on the plot corresponds to a certain level of light intensity. The value of *n*, increasing exponentially with V_{OC} for both devices, describes the accumulation of charge carriers in the electronic states of active layer and/or charge transport layers, and is an estimation the amount of electronic charge needed to sustain a certain level of quasi-Fermi-level splitting in the respective devices. Obviously, the major difference between the *n*-V_{OC} plots of the two devices is a change in slope (1/m), where for the conventionally processed device m = 2.2 and for co-annealed device m = 3.0. As the shape of *n*-V_{OC} plots provides a measure of how charge density evolves with quasi-Fermi level splitting, the decrease of *n* - V_{OC} slope in co-annealing processed devices can be interpreted as a narrowed distribution of tail states below the band edges, leading to an increase of obtained V_{OC} for given carrier density in the cell. Moreover, the *n* value at 1 Sun equivalent illumination for the conventionally processed device is 1.02×10^{11} cm^{-2}, which is increased to 1.35×10^{11} cm^{-2} in the co-annealed device (both

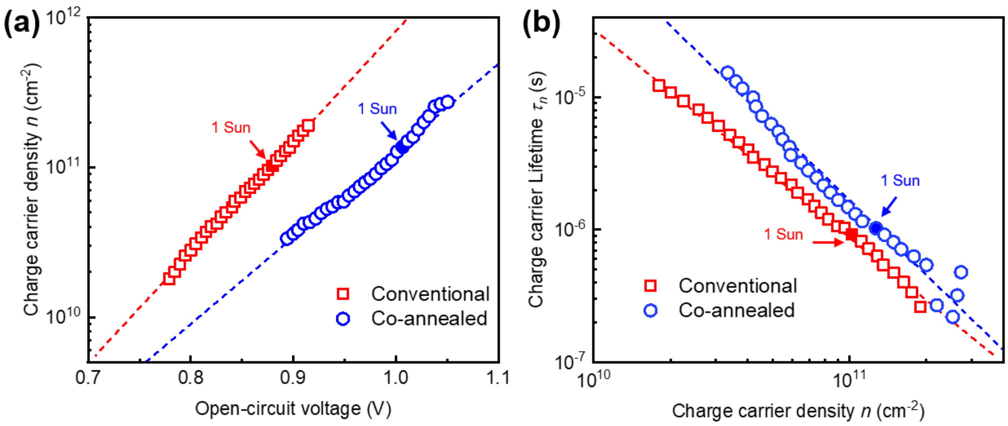

Figure 4.11 (a) Excess electronic charge density *n* at open circuit stored in the device as a function of measured V_{oc}. **(b)** Charge carrier lifetime τ_n as a function of excess electronic charge density *n* at open circuit.

marked by solid symbols in Figure 4.9a). Such an increase, approximately 35 %, in the accumulated carrier density at 1-sun is caused by an increase of their average total carrier lifetime (τ_n). **Figure 4.11 b** shows τ_n as a function of n, where the experimental data follows a power law relationship, describing the average recombination lifetime of electrons and holes in the complete device (see SI for more details). Importantly, for a given carrier density, the lifetime is increased in devices prepared by the modified processing route, which allows more charge carriers to be accumulated in the modified devices at fixed illumination intensities, increasing the quasi-Fermi level splitting and therefore V_{OC}.

V_{OC} reconstruction

As is described in the experimental chapter, if the amount excess charge accumulated in the working device (n) is corrected estimated, and the measured photovoltage decay time-constants (τ) are related to a recombination process then we should be able to calculate device V_{OC} using only these measured data and their corresponding fitting

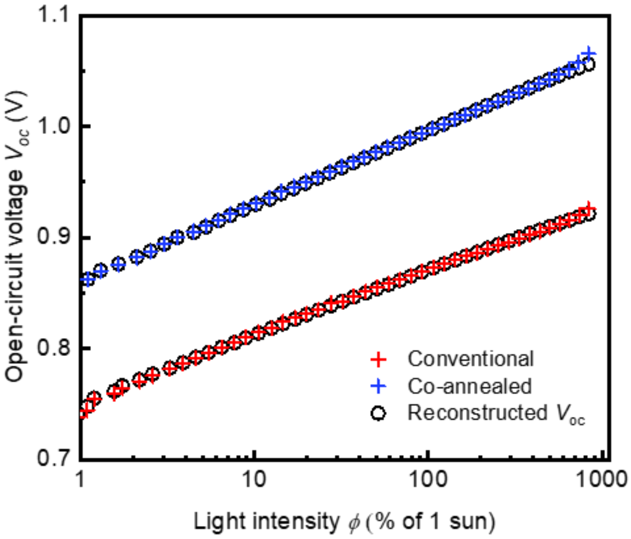

Figure 4.12 Measured V_{OC} (crosses) vs reconstructed V_{OC} (circles) of conventionally processed and co-annealed devices shown as a function of light intensity.

parameters. It is apparent in **Figure 4.12** that this reconstructed V_{OC}^{Rec} are in excellent agreement with the directly measured V_{oc} for all devices. This confirms the validity of our estimation of n and τ_n as correctly describing the *in-situ* recombination flux in a working cell.

4.4.5. Impact on Surface Recombination

To illustrate the origin of reduced recombination the photoluminescence (PL) decay of multilayer-stacks (glass/PEDOT:PSS/MAPI/PCBM) is probed, excited with a 404-nm laser from i) the glass side and ii) the PCBM side. **Figure 4.13 a** shows a clear increase of PL decay lifetime on co-annealed samples when pumped from the glass side which is not observed when pumped from the PCBM side. Importantly, such an increase of the PL lifetime at the interface describes an open-circuit condition and shall be regarded as suppression of interfacial recombination.[172] Thus the results imply that reduced recombination is mainly at PEDOT:PSS/MAPI interfaces.

It appears from above data that removal of bulk defects reduces the surface recombination in the device.[228] This is mainly due to a mitigation of electric filed screening by these ionic defects in MAPI layer,[7] such that electron diffusion to the wrong interface is retarded. By doing so, as shown in **Figure 4.13 b** and **4.13 c**, that electrons are separated from the holes at PEDOT:PSS/perovskite interfaces and thus surface recombination of perovskite is suppressed.

Our data suggest that microstructural defects in MAPI thin films are related to a lack of crystalline coherence throughout the thickness of the MAPI. The top surface of conventionally processed MAPI layer, *i.e.* the MAPI/PCBM interface, is the region susceptible of microstructural defects – likely due to the fast solvent evaporation that occurs here at the early stages of film formation. Importantly, by removing these defects interfacial recombination at PEDOT:PSS/MAPI heterojunction can be mitigated leading to enhancement of V_{OC} in PEDOT:PSS-based perovskite solar cells. Additionally, as noticed from both STEM images and TEM images that there might be some shifts in the lateral size of MAPI grain between the two processing routes. By considering that vertical grain boundaries mostly impact on thus J-V hysteresis,[229] as well as shunting pathways that affect FF,[185] the large improvement of V_{OC} measured above is not likely mainly due to the change in lateral grain size.

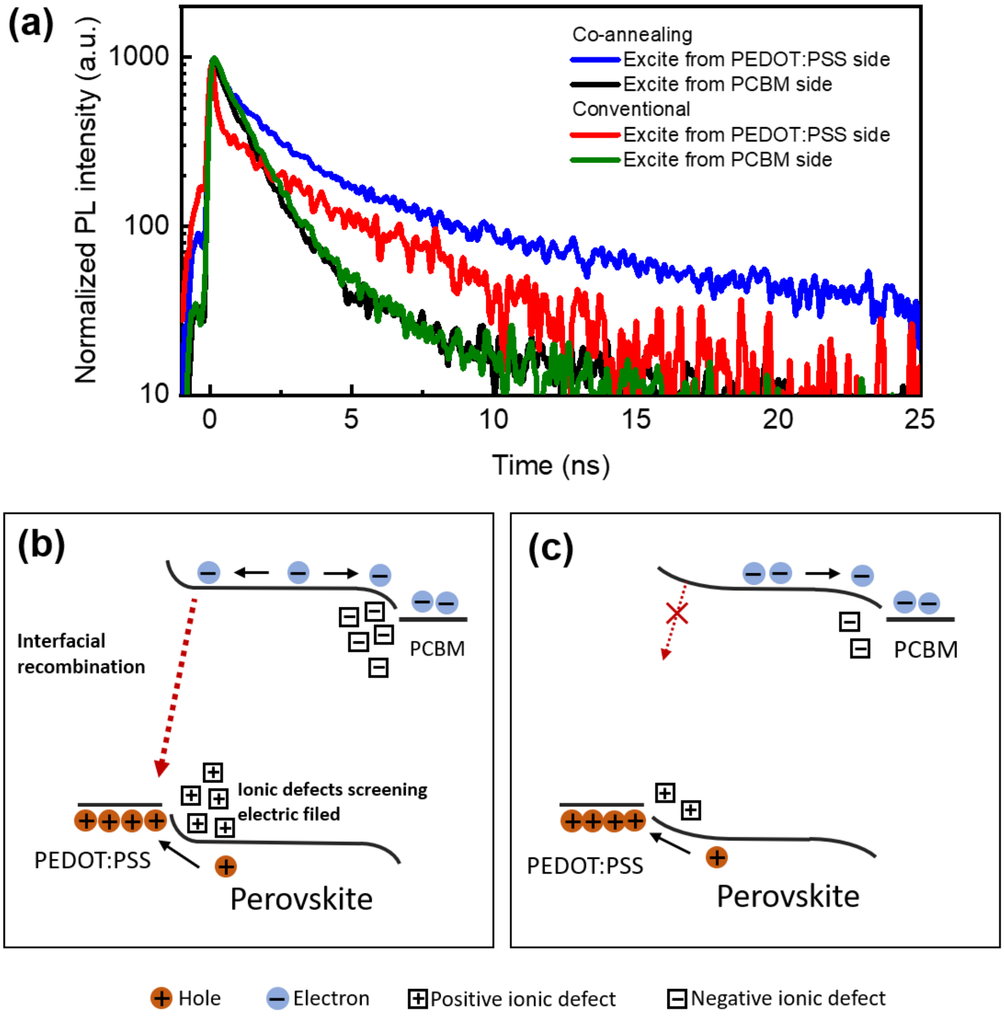

Figure 4.13 **(a)** Time-resolved photoluminescence decay of glass/ PEDOT:PSS/ perovskite/ PCBM stacks, excited with a 404-nm laser from glass side and PCBM side. **(b)** Schematic drawing of band diagram, photoexcited charge carriers and recombination processes in the perovskite solar cells, where ionic defects in perovskite screens electric field and causes interfacial recombination (left) and ionic defects are removed (right).

By showing these data the importance of controlling crystallographic defects in MAPI active layer is highlighted, however, co-existence of other loss mechanisms has hindered the co-annealing processed device from achieving comparable PCE as the most efficient cells reported,[157] the loss mechanisms are likely to be interfacial recombination owing to doping of PEDOT:PSS[204] which will be discussed in the next or energetic losses in PCBM layer.[171]

4.5 Conclusion and Perspective

In this chapter using STEM the presence of previously undetected microstructural defects and inhomogeneities in MAPI thin films that reside near the MAPI-air interface have been identified. The findings show that these defects are inherently correlated to a single step in the well-established solution processing methodology, and we outline a facile means of their elimination without increasing the number or complexity of processing steps. By removing these defects, significant improvements in intra-grain crystallographic coherence along the charge-transport direction can be achieved, which results in improved power conversion efficiencies from 13.6% to 17.4 %. The *in-situ* optoelectronic characterisations link this to an improvement in charge collection efficiency and a reduction in electron-hole recombination at PEDOT:PSS/MAPI interface and an overall decrease of trap state density in our perovskite solar cells.

The results highlight the role of advanced imaging techniques in identifying defects that play a significant effect on device performance, and our modified processing route is identified as a convenient means of eliminating electronic trap states. The modifications made to the processing method eliminate such defects from forming, improve crystallographic registry along the charge transport direction and minimise intrinsic losses in perovskite solar cells.

5. p-doping of organic hole transport layers in p-i-n perovskite solar cells: correlating open-circuit voltage and photoluminescence quenching

5.1 Declaration of contributions

The results presented in this chapter formed the basis of reference [125]

Weidong Xu and Jinhyun Kim carried out photoluminescence spectroscopic measurement.

Shengda Xu aided optical measurements.

Matyas Daboczi carried our Kelvin probe and photoemission

Chieh-Ting Lin aided with solar cell optimisation.

5.2 Abstract

The previous two chapters probed the impact of perovsktie crystallinity and microstructure on device perofrmance and particularly on V_{OC}, both with fixed device structure, *i.e.* employing PEDOT:PSS as common hole transport layers (HTL). Further boost of device PSC, neverthless, relies on engineering of the hole transport mateirals. suggsting interfacial recombiantion as one of the major loss channels in PSCs. In this chapter the role of HTL doping on V_{OC} and PCE is investitaged.

Doping is a widely implemented strategy for enhancing the inherent electronic properties of charge transport layers in photovoltaic (PV) devices. Here, in direct contrast to existing understanding, we find that a reduction in p-doping of the organic HTL leads to substantial improvements in PV performance in planar p-i-n PSCs - driven by improvements in V_{OC}. Employing a range of transient and steady state characterisation tools, we find that the improvements of V_{OC} correlate with reduced surface recombination losses in less p-doped HTLs. A simple device model including screening of bulk electric fields in the perovskite layer is used to explain this observation. In particular, photoluminescence (PL) emission of complete solar cells shows that efficient performance is correlated to a high PL intensity at open circuit and a low PL intensity at short circuit. We conclude that desirable transport layers for p-i-n PSCs should be charge selective contacts with low doping densities.

5.3 Introduction

PSCs with a p-i-n architecture are typified by a planar perovskite active layer (typically methylammonium lead halide, MAPI) sandwiched between a bottom p-type HTL and a top n-type electron transport layer (ETL). Such PSCs have drawn intensive research interest due not only to minimised current-voltage (J-V) hysteresis observed under operation[217] but also to their ease of fabrication.[230] For example, their low-temperature, solution-based processability is inherently compatible with large-volume manufacturing and enables their application in more complex device architectures *e.g.* tandem solar cells.[47] However, the attainable power conversion efficiencies (PCEs) for p-i-n devices are typically somewhat lower than their mesoporous or planar n-i-p analogues,[190] mainly because they typically exhibit a slightly lower open-circuit voltage (V_{OC}).[196] Therefore it is of particular interest to determine the factors limiting the achievable V_{OC} of planar p-i-n PSCs.

Previous studies have demonstrated that the electronic band gap,[148] crystallinity[110] and microstructural defects[231] of the photoactive perovskite layer are key factors determining device V_{OC} of PSCs. A further consideration are the recombination kinetics, where an increased rate of recombination is known to reduce V_{OC}.[148] Interestingly, when organic/polymeric charge transport layers are utilized, it has been demonstrated that PSC V_{OC} is insensitive to changes in either the highest occupied molecular orbital (HOMO) level of the HTLs employed[232,233] or to changes of the lowest unoccupied molecular orbital (LUMO) level of the ETL.[172] It has even been shown that some PSCs employing wide band gap perovskites yield V_{OC} values greater than the HTL-ETL energetic offset.[234] A widely recognized, but as yet relatively poorly understood issue in PSCs is surface recombination, in particular, for p-i-n devices, recombination that occurs at the interface between the perovskite active layer and the most widely used HTL, poly(3,4-ethylenedioxythiophene)- poly(styrenesulfonate) (PEDOT:PSS).[235] Several studies have identified this issue, and shown that modification or replacement of PEDOT:PSS can improve device V_{OC} and PCE.[168,236–238] Interestingly, in organic photovoltaics (OPVs) with analogous p-i-n architectures employing PEDOT:PSS as an HTL, surface recombination has often been found to be less important as a loss pathway;[239] indeed in many cases, state-of-the-art OPV efficiencies have been reported using PEDOT:PSS.[240] The origin of the surface recombination losses in p-i-n perovskite solar cells, and how these may be reduced by selection of HTL, is thus currently poorly understood, and is the focus of the study reported herein.

The core function of a HTL is to selectively transfer photoexcited holes from the absorbing material to the external circuit, a process which in PSCs is often monitored by photoluminescence quenching (PLQ) measurements of the absorber interfaced with a HTL.[9] During such measurements, if high PLQ efficiency is observed when the absorber is interfaced with a HTL/ETL, this is frequently interpreted as an indication of effective charge transfer – and thus indicator of efficient photocurrent generation.[241] However such PLQ may also result from undesirable surface recombination losses, as widely reported for inorganic photovoltaic devices,[127,134,242,243] complicating the interpretation of such data. In addition, PL intensity in PSCs has been shown to be dependent on device measurement conditions *i.e.* typically higher at open circuit than short circuit,[38] and non-linearly dependent upon excitation intensity, a phenomenon ascribed to charge trapping and bimolecular recombination processes.[12] Indeed some studies have suggested that, due to the low electron-hole binding energy and relatively long carrier lifetimes reported for MAPI,[244] charge carriers accumulate primarily in the perovskite layer under open circuit conditions, and are not transferred to the HTL and ETL layers at open circuit.[233] The complexity of these factors has so far hindered our understanding of how significant charge transfer and extraction kinetics are to the PCE of PSCs, and how these compete with undesired recombination losses.

This chapter focuses on the role of HTL in determining the V_{OC} and PCE of p-i-n, the so called inverted-architecture planar PSCs, specifically investigating the impact of p-doping of HTL on charge transfer and surface recombination. Herein a variety of HTLs in PSCs are investigated, all employing methylammonium lead iodide ($CH_3NH_3PbI_3$, MAPI) as the common photoactive layer. Using poly(3,4-ethylenedioxythiophene)-poly(styrenesulfonate) (PEDOT:PSS) as our reference HTL we investigate key performance parameters when poly[bis(4-phenyl)(2,4,6-trimethylphenyl)amine] (PTAA) and poly[N,N’-bis(4-butylphenyl)-N,N’-bis(phenyl)benzidine] (PTPD) are used as alternative HTLs. The variations in PL intensity observed between short and open circuit conditions are a powerful and relatively easy to obtain probe of surface recombination losses. From these results it is concluded that reducing p-doping in HTLs is an effective strategy for reducing surface recombination losses in p-i-n perovskite solar cells and can result in enhanced device V_{OC} values and overall PCEs.

5.4 Experimental Results

5.4.1. Device performance Based on Different HTLs.

Photovoltaic Performance

P-i-n PSCs were prepared with a structure of glass/ITO/HTL/ MAPI(500nm)/PCBM(50nm)/LiF(0.7nm)/Ag (100nm). Four HTLs, PEDOT:PSS (40 nm), PTAA (20 nm) and PTPD (20 nm) were deposited on indium-doped tin oxide (ITO) substrates, in all cases the MAPI layers were fabricated with the same procedure.[84] The [6,6]-phenyl-C_{61}-butyric acid methyl ester (PCBM) was deposited onto the MAPI layer as electron transport layer (ETL) and LiF/Ag bilayer was thermally evaporated on top of PCBM as cathode to complete the device. Prior to deposition of MAPI thin films, an ultrathin Poly [(9,9-bis(3'-(N,N-dimethylamino)propyl)-2,7-fluorene)-alt-2,7-(9,9–dioctylfluorene)] (PFN) poly-electrolyte layer was spun onto PTPD and PTAA to reduce their surface hydrophobicity.

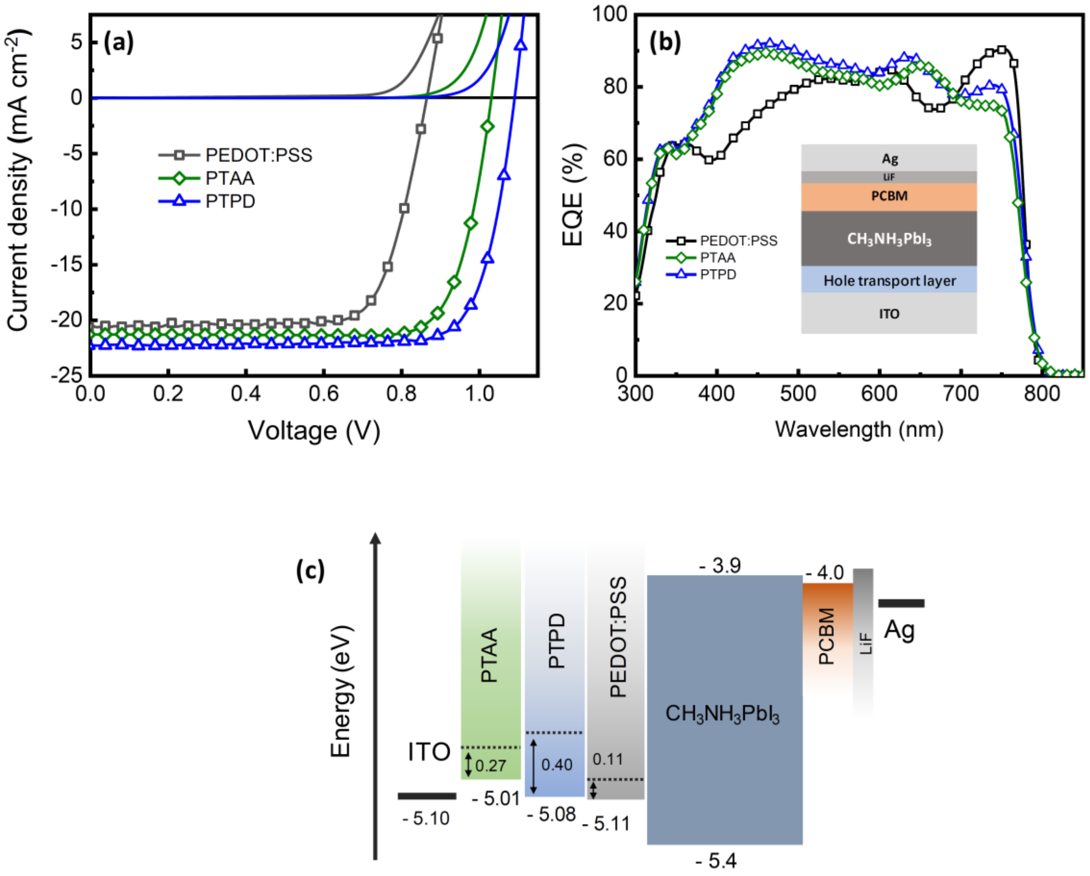

Figure 5.1 (a) J-V curves of typical p-i-n perovskite solar cells based on PEDOT:PSS, PTAA and PTPD as HTLs, under AM1.5 1 Sun equivalent illumination at a scan rate of 50 mV s^{-1} in reverse bias. **(b)** External quantum efficiency (EQE) spectra of these devices. The inset figure shows a schematic drawing of device structure. **(c)** Schematic drawing of flat-band energy diagram of the solar cells, showing the highest occupied molecular orbital (HOMO) level, and equilibrium Fermi level (dashed lines) of these HTLs. The energetic differences between HOMO and Fermi level are calculated and labelled on the figure and will be discussed below.

Figure 5.1 a shows representative J-V characteristic for devices prepared with the various HTLs measured under illumination and in the dark. The photovoltaic performance parameters based on 5 different pixels are also summarized in **Table 5.1**. The power conversion efficiency (PCE) of the PEDOT:PSS HTL device was determined to be 13.5 ± 0.2%, which is consistent with previous chapters and with existing literature,[190] when the alternative HTLs are employed PCE increases from 18.9 ± 0.3% (PTAA) reaching 19.6 ± 0.2% (PTPD). Analysis of the output characteristics makes it apparent that the observed overall performance improvements closely follow increases in open circuit voltage (V_{OC}). The external quantum efficiency (EQE) spectra of representative devices are shown in **Figure 1 b,** with a schematic illustration of the device shown in the inset. All devices show a comparable EQE onset at approximately 780 nm, but the device employing PEDOT:PSS has a couple of regions where the measured EQE is significantly less than the other materials.

Table 5.1 Performance and photovoltaic parameters of PSCs with different HTL

	J_{SC} (mA cm^{-2})	V_{OC} (V)	FF	PCE (%)
PEDOT:PSS	*20.49* ± 0.21	*0.864* ±0.008	*0.754* ± 0.007	*13.49* ± 0.20
PTAA	22.17 ± 0.12	1.073 ±0.004	0.792 ± 0.008	18.85 ± 0.29
PTPD	22.38 ± 0.31	1.095 ±0.004	0.798 ± 0.010	19.61 ± 0.15

Energetics of HTL

In **Figure 5.1 c** shows a flat-band energy diagram for these p-i-n devices is shown, in addition the HOMO levels of the HTLs, obtained by measuring their ionization potential through ambient pressure photoemission spectroscopy (APS),[245] are added**.** In **Figure 5.2 a** the chemical structure the HTM is shown, in combine with APS data in **Figure 5.2 b–d**. Importantly, whilst there is some variation in the HOMO values between HTLs, there is no correlation between these values and the V_{OC} observed, consistent with existing literature.[232] The dashed lines in **Figure 5.1 c** indicate the equilibrium dark Fermi level of the HTLs measured with a Kelvin probe, **Figure 5.2 e-h**.

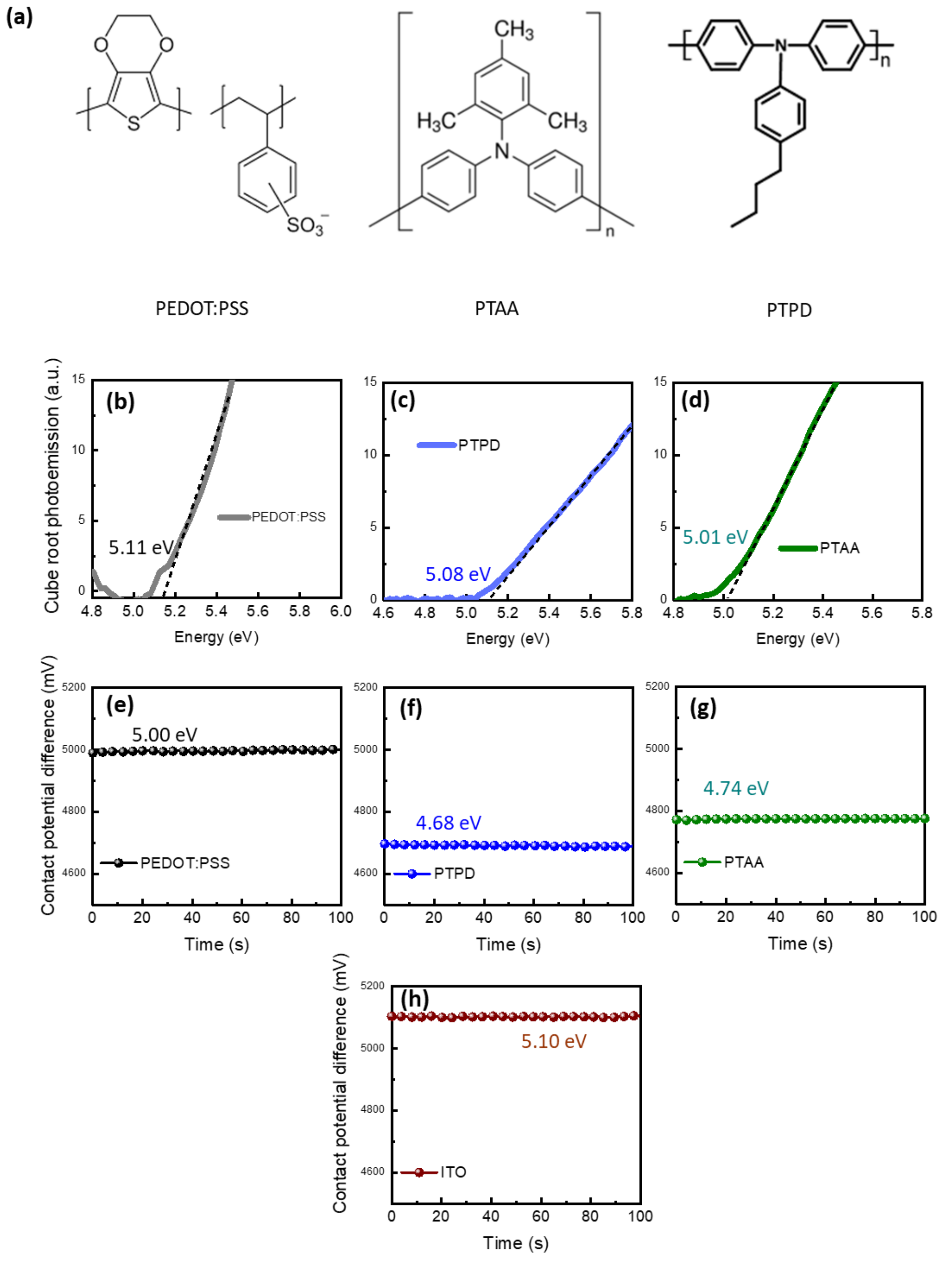

Figure 5.2 **(a)** Chemical structures of organic hole transport materials. **(b)** – **(d)** Photoemission spectra of the HTLs. **(e)** – **(h)** Work function of the HTLs and ITO.

The significance of this energetic difference between HOMO and Fermi level, labelled in the figure, will be discussed further below.

Characterisation of Bulk Properties

In order to exclude the possibility that the observed variations in V_{OC} are induced by structural or morphological variations in the MAPI layers on the various HTLs, a range of complimentary characterisation techniques are employed, namely X-ray diffraction (XRD) (**Figure 5.3 a)**; UV-Vis absorption spectroscopy (**Figure 5.3 b)** and scanning electron microscopy (SEM) (**Figure 5.3 c-e**). Analysis of the peak positions, intensities and full-widths at half-maximum (FWHM) of the XRD data (**Table 5.2)** show no

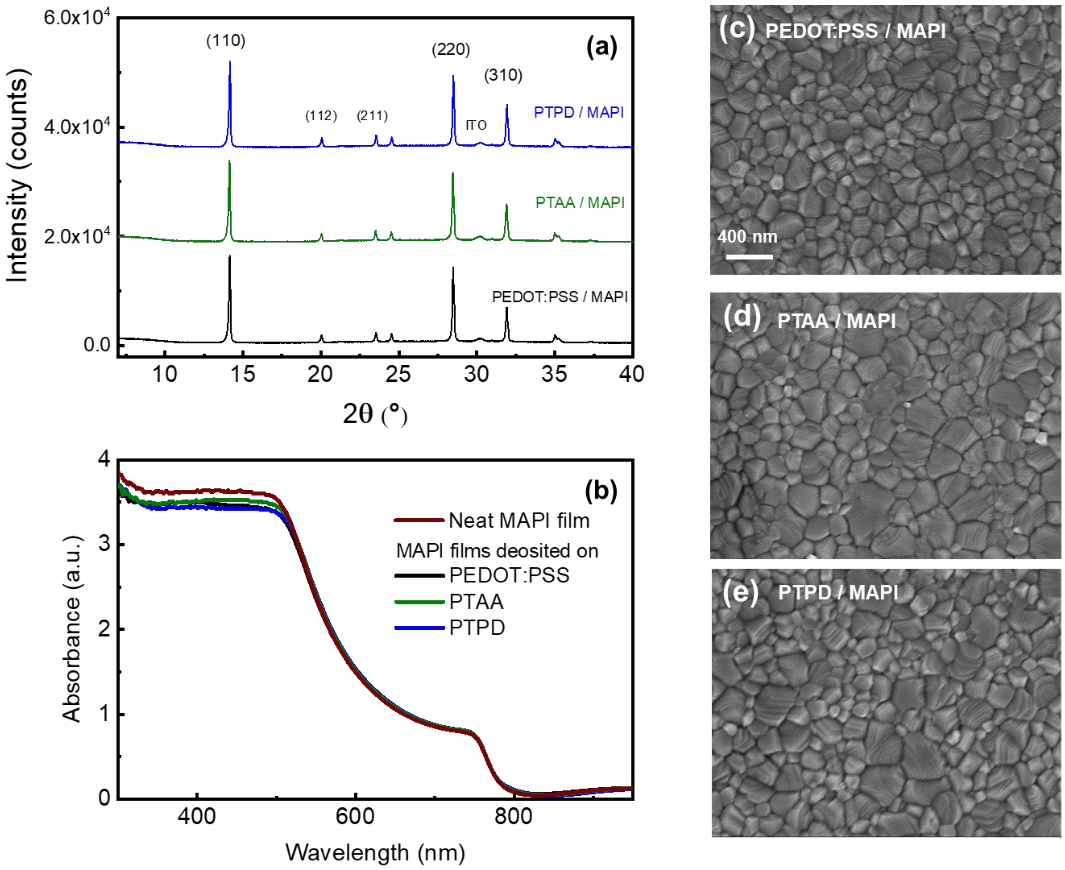

Figure 5.3 Properties of bulk perovskite deposited on different HTLs. **(a)** X-ray diffraction patterns and **(b)** ultraviolet-visible (UVvis) absorbance spectra. **(c)** – **(e)** Surface scanning electron microscopy (SEM) images of MAPI films deposited on different HTLs.

appreciable differences as the HTL is altered.[110] Similarly, the MAPI absorbance spectra show no significant differences as the HTLs change and the surface of the MAPI films, characterised by SEM, are comparable, with all showing a compact, coalesced structure with no observable variation in grain size nor the presence of pinholes. As such, we can conclude that the differences in device performance shown in **Figure 5.1** do not result from differences in the macroscopic properties of the MAPI layers in these devices.

Table 5.2 XRD parameters of MAPI films deposited on different HTLs

	PEDOT:PSS / MAPI	PTAA / MAPI	PTPD / MAPI
Peak position (degree)	14.15	14.14	14.16
FWHM (degree)	0.10	0.09	0.10
Peak intensity (count)	16567	16855	16264

5.4.2. Photoluminescence Analyses

PL of HTL/Perovskite Films

The photoluminescence quenching (PLQ) studies are now considered as a potential assay of hole transfer from MAPI to the HTLs. **Figure 5.4** shows PL emission spectra of a bare MAPI film and MAPI films in contact with the various HTLs. To ensure the PLQ measurements are relevant and comparable to the measurements made of

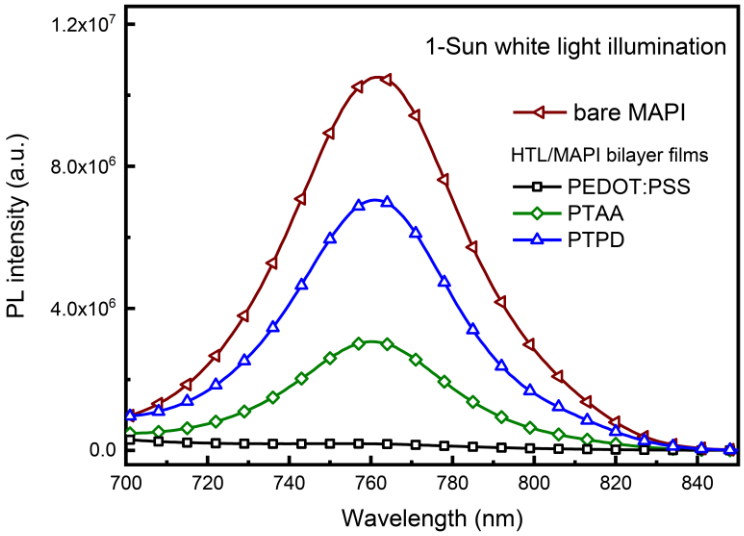

Figure 5.4 PL emission of MAPI film and stacks of HTL/MAPI bilayer films under 1 Sun equivalent white-light illumination.

operational devices, and in particular to avoid severe charge trapping effects observed within MAPI under low intensity irradiation conditions,[9] our PLQ measurements employed white light illumination at 1-Sun equivalent intensity. From these data, the bi-layer PLQ (PLQ_{BL}) efficiency was estimated as the difference in emission intensity between a bare MAPI film and the various bilayers, listed in **Table 1**. From the table it is apparent that there is an inverse relationship between device PCE and PLQ_{BL} efficiency – such that the bilayers showing lower PLQ_{BL} efficiency in the presence of HTL, in other words higher PL emission intensity in bilayers, yield the higher device PCE in complete devices. This observation is clearly counter to the widely used interpretation of PLQ_{BL} as a measure of the efficiency of desired charge transfer to the transport layer, but is rather suggestive that for this sample series, higher PLQ_{BL} may be indicative of enhanced surface recombination losses,[134] as we explore further below.

PL of Complete Solar Cells

The bare MAPI and the MAPI/HTL bilayer films detailed in Figure 5.4 were prepared using glass substrates and in the absence of a top electrode *i.e.* where there is no charge extraction to an external circuit and all photogenerated charges must ultimately recombine. Thus, our PL measurements were performed under conditions most equivalent to open circuit. Now the PL emission is considered of the corresponding complete devices held under 1-Sun equivalent illumination at either open circuit or short circuit conditions, as shown in **Figure 5.5 a – 5.5 d.** Under short circuit conditions, all devices showed similar, relatively low intensity photoluminescence (PL_{SC}). This is indicative of efficient charge transfer to the ETL/HTL layers in these devices, most likely associated with efficient charge extraction to the external circuit under these conditions, suppressing radiative recombination in the absorber layer. The relative invariance of PL_{SC} between HTLs agrees with the relatively consistent J_{SC} values observed for these devices (Table 5.1). In contrast, the PL intensity measured at open circuit (PL_{OC}) varies considerably between devices. In particular, it is found that the relative intensity of PL_{OC} between these devices tracks the trend observed for the relative PL intensity of the bilayer films in Figure 5.4. Whilst for efficient HTLs, *i.e.* PTPD, the PL intensity increases substantially between short and open circuit conditions, it is almost unchanged for the PEDOT:PSS device. To quantify this effect, we determined the open-circuit-to-short-circuit (OC-to-SC) PL quenching efficiency ($PLQ_{OC\text{-}SC}$) calculated as (PL_{OC} – PL_{SC})/PL_{OC}, describing the magnitude of the difference in PL emission intensity between open and short circuit. It is noted that this quantification avoids the need to compare the absolute emission intensities between devices, which could also be influenced by the optical reflections of these devices. **Figure 5.5e** plots the calculated values of device V_{OC} and PCE versus $PLQ_{OC\text{-}SC}$. A clear correlation is observed, with both PCE and V_{OC} correlated with an increase of $PLQ_{OC\text{-}SC}$. This implies that for the PSCs studied herein, enhanced device performance correlates with a high PL intensity at open circuit and low PL intensity at short circuit.

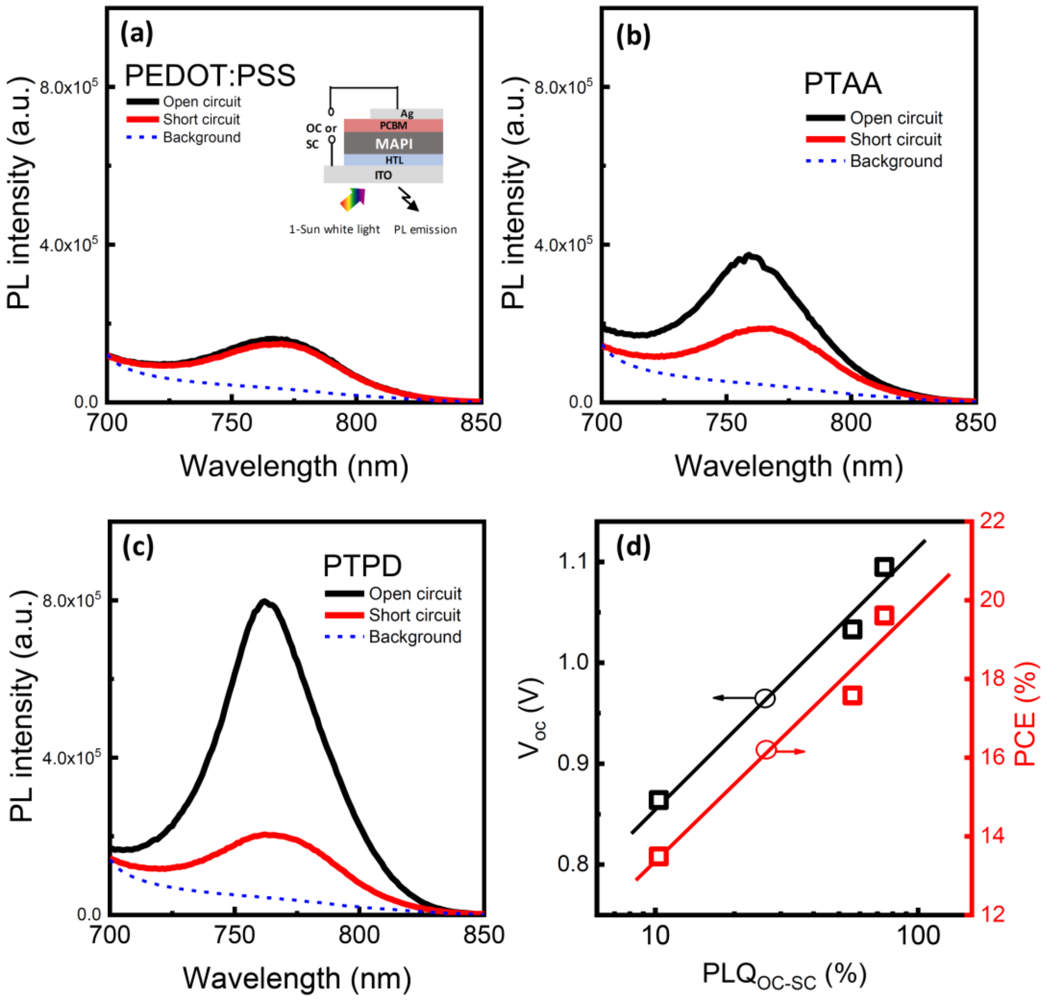

Figure 5.5 (a) – (c) PL emission spectra of ITO/HTL/MAPI/PCBM/(LiF)Ag complete devices at short circuit and open circuit with PEDOT:PSS, PTAA and PTPD as HTL. The inset figure in (a) shows a schematic drawing of the measurements. **(d)** Correlation of V_{OC} and PCE versus OC-to-SC PL quenching efficiency (PLQ_{OC-SC}) in complete devices.

This is consistent with general photovoltaic device physics,[1] with optical excitation of efficient devices expected to yield maximal radiative recombination at open circuit but efficient charge extraction at short circuit.[246,247] However, to the best of our knowledge, this behaviour has not previously been directly correlated with device efficiency for PSCs in the current literature.

Correlation of PL Quenching and HTL Doping

Now the origins of the observed variation in PLQ_{OC-SC} and V_{OC} between the HTLs are considered. As shown above neither the measured device V_{OC} nor PCE correlate with the HOMO levels of the HTLs, there is also no apparent correlation between the measured HTL's E_F and the measured device performance metrics. The p-doping of the HTLs is considered as a potential explanation for the observed behaviour. It is known that increased doping levels lead to greater HTL conductivity thus reduced the voltage losses due to electrical resistance.[248,249] The p-doping for the various HTLs is quantified by calculating the energy difference between their HOMO and E_F values. This energy difference, denoted as $E_F – E_{HOMO}$, indicates the relative p-type doping levels to be PEDOT:PSS > PTAA > PTPD. Utilising these data, the measured PLQ_{BL}, PLQ_{OC-SC}, device V_{OC} and PCE versus measured E_F - E_{HOMO} (**Figures 5.6 a – 5.6 b)** are plotted. It is clear from Figure 5.6a that as p-doping of HTL increases, there is a decrease in PLQ_{BL} measured in the presence of the HTLs, and an increase in PLQ_{OC-SC} in complete devices, suggesting that increased p-doping of our HTLs quenches PL emission at OC. This correlates with the trend shown in Figure 5.6b showing that both increased V_{OC} and PCE derives from a reduction in HTL p-doping. It is thus evident that the devices with the highest measured V_{OC}, and therefore PCE, are those that employ least p-doped HTLs.

5.4.3. Evidence of Surface Recombination

When combined, these data support the suggestion that the observed variations in device performance are not related to shift of HOMO levels but most likely originate from differences in surface recombination losses, and specifically that these surface recombination losses are primarily determined by the extent of p-doping of the HTL layer. To probe further the recombination losses in our device series analysis of device optoelectronic performance is carried out.

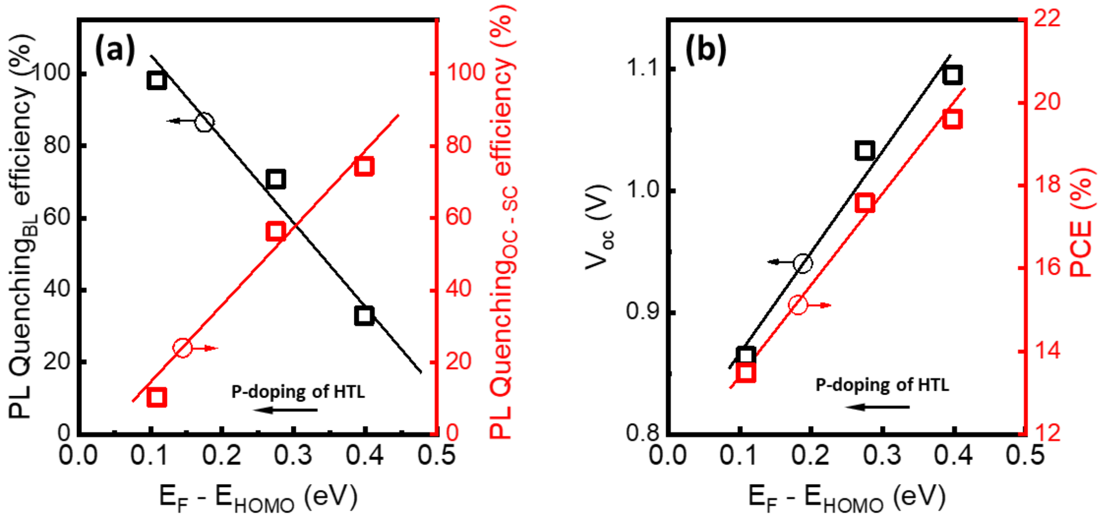

Figure 5.6 (a) Correlation of photoluminescence quenching efficiency in HTL/MAPI bilayer films (PLQ$_{BL}$) and in complete devices between open circuit and short circuit (PLQ$_{OC-SC}$), with the p-doping level of HTL that is estimated by the difference of HOMO and Fermi level, E$_F$ - E$_{HOMO}$. **(b)** Correlation of device V$_{OC}$ and PCE with the E$_F$ - E$_{HOMO}$ of HTL.

One widely used assay of such recombination losses is to measure the evolution of V$_{OC}$ with light intensity the derive an ideality factor n_{id} from the slope of V$_{OC}$ -light intensity relationship: $n_{id} = \frac{q}{\mathrm{k}T} \cdot \frac{\delta V_{oc}}{\delta \ln(I)}$, where kT is the thermal energy, I the light intensity and q the unit charge. **Figure 5.7 a** shows the semi-logarithmic plot of steady state V$_{OC}$ versus light intensity, and the n_{id} values obtained by fitting the plot between 0.04 – 4 Suns. The most efficient devices *i.e.* those with higher V$_{OC}$ and PTPD and PTAA as HTLs, both show rather large values of n_{id}, 1.79 and 1.84 respectively. In contrast, devices with lower V$_{OC}$, as seen with PEDOT:PSS HTLs, exhibited lower n_{id} of 1.70 and 1.12 respectively. A lower n_{id} in combination with lower device V$_{OC}$ is typically attributed the devices limited by monomolecular surface recombination at the contacts,[152,237,250] resulting in less steep increase of V$_{OC}$ with light intensity in the semi-logarithmic plot. Interestingly, devices with high V$_{OC}$ and high PCE exhibiting n_{id} values close to 2 have also been reported for efficient n-i-p, conventional PSC's,[149] indicative of higher order losses such as bimolecular recombination. These data thus are consistent with non-radiative recombination at open circuit in PEDOT:PSS cells being related to the presence of monomolecular recombination at HTL/MAPI interface, often referred to as surface recombination.

To support these hypotheses, and correlate the observed variation in V_{OC} to modulations in the p-doping of the HTL influencing surface recombination at the MAPI/HTL interface, additional transient optoelectronic measurements are carried out at varying illumination intensities to determine accumulated charge densities and charge recombination lifetimes at open circuit as a function of device V_{OC}. **Figures 5.7 b** plots the excess (photogenerated) charge density (n) in these devices as a function of V_{OC}, in which all devices show an approximately exponential increase of n with V_{OC}, assigned to charge "stored" in the electronic states of MAPI and/or contact layers. The overall charge recombination kinetics of the complete devices can be quantified by the lifetime of charge carriers (τ) derived from TPV decays, plotted in **Figure 5.7 c** as a function of charge density. The slope of the n vs V_{OC} plots for all of the HTLs investigated are similar (Figure 5.7b) suggesting that these devices are dominated by charge accumulation in the MAPI layer. This is consistent with our recent work employing PEDOT:PSS as an HTL in p-i-n devices, where it is found that at very low light intensities photogenerated charge accumulated primarily on the device contacts and at higher intensities, as employed for the data in **Figure 5.7 b** and **5.7 c**, that charge primarily accumulated within the MAPI layer.[148] It is striking that the PEDOT:PSS device data in Figure 5.7b shows equivalent accumulated charge densities at much lower measured V_{OC} values than the devices with a lesser degree of p-doping. As the accumulated charge density is a measure of the active layer quasi-Fermi level splitting, this observation implies that when employing PEDOT:PSS as the HTL, the externally measured V_{OC} is substantially (~150 mV) less than active layer quasi-Fermi level splitting. Analogous data have been shown in organic solar cells as a function of metal-oxide HTL processing conditions, with the aid of device modelling, that such a reduction in V_{OC} relative to active layer quasi-Fermi level splitting is expected in the presence of surface recombination losses.[250] The presence of surface recombination losses is further supported by Figure 5.7c, which shows that increased HTL p-doping is correlated with faster recombination kinetics for matched densities of accumulated charge. This trend was also observed for organic solar cells with increased surface recombination losses.[250] As a result of these slower recombination kinetics, devices

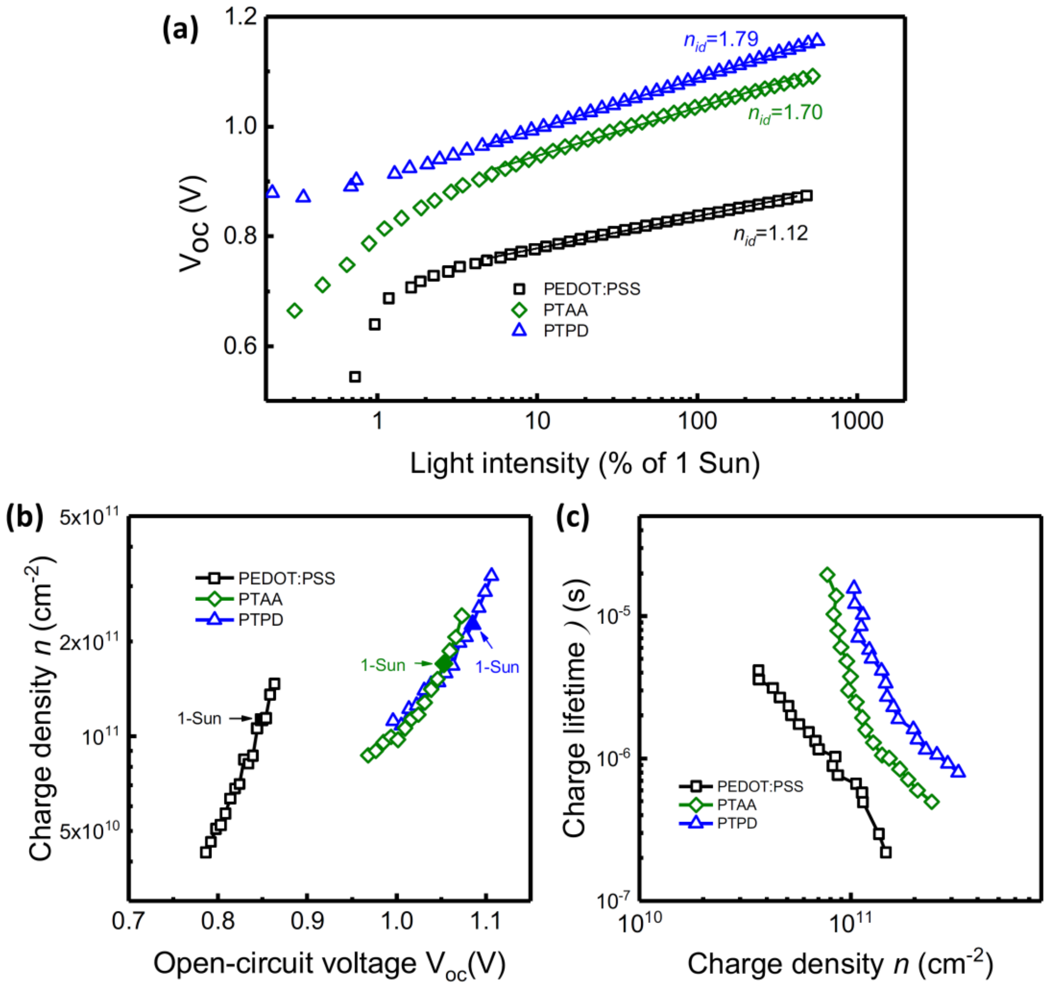

Figure 5.7 (a) Evolution of device V_{OC} as a function of light intensity, and the light ideality factor n_{id} derived from fitting the plot between 0.04 – 4 Suns. (b) Charge carrier density n as a function of V_{OC} in the solar cells with various HTLs. The solid symbol corresponding to approximate 1-Sun condition. **(c)** Charge recombination lifetime τ derived from transient photovoltage (TPV) decay as a function of n.

with suppressed surface recombination can "store" more photoexcited charge within the active layer under 1 Sun (these conditions are marked as solid symbols in Figure 5b). This gives rise to an additional increase of V_{OC} by about 50 - 85 mV for the less p-doped HTL's compared to PEDOT:PSS. The approximate 1-Sun accumulated charge densities are PTPD (2.3×10^{11} cm^{-2}) > PTAA (1.9×10^{11} cm^{-2}) > PEDOT:PSS (1.1×10^{11} cm^{-2}). These correlate with the order of their PL_{OC} intensities, consistent with higher accumulated charge densities resulting from suppressed non-radiative, in this case surface, recombination and thus resulting in enhanced radiative recombination and therefore PL. In summary, our ideality factor and transient optoelectronic measurements all support enhanced surface recombination losses with more doped HTLs, resulting in devices with reduced V_{OC}.

5.5 Discussion and Conclusion

In this chapter the significance of p-doping in the HTL of p-i-n PSCs has been demonstrated, specifically that a reduction in p-doping results in significant improvements in device V_{OC} and PCE. By employing a range of complimentary techniques, including photoluminescence quenching, photoemission spectroscopy and kelvin probe analyses, device ideality factor and measurements of charge carrier densities and lifetimes at open circuit, it is concluded that the reduction in device V_{OC} observed in more p-doped HTLs results from enhanced surface recombination losses. In particular it is found that measurement of the open-circuit-to-short-circuit (OC-to-SC) PL quenching efficiency is an effective assay of such surface recombination losses, with high device performance correlating with a high PL intensity at open circuit (where charges are primarily confined to, and recombine in, the photoactive layer) and a low PL intensity at short circuit (where charges are efficiently extracted to the external circuit). It can therefore be concluded that minimisation of HTL doping is a key consideration for the optimization of the performance of planar p-i-n PSCs.

The enhanced surface recombination losses for p-doped HTL layers implies this recombination is associated with the dark charge present in these layers, rather than photoinjected charge. Typical carrier densities in PEDOT:PSS thin films are approximately 2 x 10^{20} cm^{-3},[251] corresponding to 8 x 10^{14} cm^{-2} for the 40 nm film deposited in our devices. This is approximately 3-orders of magnitude greater than the photogenerated charge density in PEDOT:PSS devices under 1-Sun illumination at open circuit (1.1 x 10^{11} cm^{-2}). Thus it can be concluded that when employing PEDOT:PSS, the density of dark charge carriers in the HTL available to undergo recombination processes is far higher than the density of photogenerated carriers. In this context, the enhanced surface recombination with greater HTL p-doping can be understood in terms of a loss of selectivity of the HTL due to the high dark carrier density, enabling not only hole but also electron transfer to the HTL layer, resulting in a net loss of photocarriers. It is apparent that this origin of surface recombination is distinct from that often observed in other inorganic solar cells such as silicon or cadmium telluride, where surface recombination is often reported to be mediated by dangling bonds at surfaces or grain boundaries, resulting in trap mediated surface recombination.[1] It is noted the mechanism of surface recombination found herein also differs from that often discussed in n-i-p PSC's employing TiO_2 as ETL, where trap states at the TiO_2/perovskite interface have been reported to mediate surface recombination losses[252,253] and has also been associated with the observation of *J-V* hysteresis in the n-i-p devices,[79,185] which is otherwise absent in the p-i-n devices studied in this work.

In contrast to the conclusions drawn here for planar p-i-n PSCs, highly doped PEDOT:PSS is widely used in OPVs[240] and in hybrid silicon/PEDOT:PSS solar cells[254] yielding excellent device performance. In such devices, efficient performance has also been observed with other doped HTLs.[249,255] It is therefore interesting to consider why PSCs are more susceptible to efficiency losses associated with surface recombination with doped HTLs than OPVs. The difference in recombination mechanisms is described by the schematic in **Figures 5.8 a – 5.8 c**. Figure 5.8c illustrates a typical energy level diagram for an OPV at open circuit. In this case, the build-in potential drops across the photoactive layer, forming an electric field that drives holes to the HTL and electrons to the ETL. As such, this built in field suppresses surface recombination losses at the HTL/organic interface, even when this HTL is doped, as it drives electrons away from this interface.[192] In contrast, in PSCs, screening effects caused by the diffusion of ionic defects in the MAPI layer [74] confine the potential drop in the MAPI layer to a thin space charge layer near the device interfaces, with the MAPI bulk being field-free,[7] as shown in Figures 5.8a-b. Such field screening allows for considerable electron diffusion towards the HTL/perovskite interface, and therefore the potential for photogenerated electrons to recombine with holes in the HTL, resulting in surface recombination (Figure 5.8b). This provides a rational for our observation herein that employing an

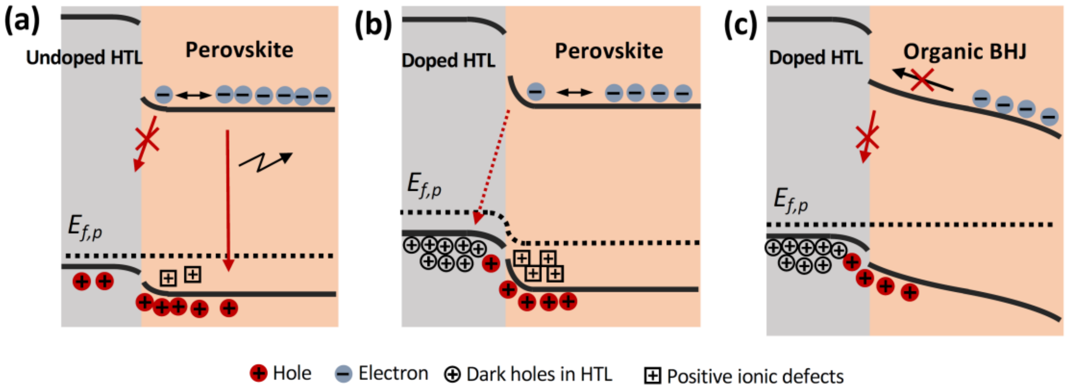

Figure 5.8 Schematic drawing of open circuit band diagram and charge accumulation/combination in the HTL interface in a p-i-n perovskite solar cells with **(a)** an undoped HTL and **(b)** a doped HTL, and **(c)** in a typical organic bulk heterojunction (BHJ) solar cell with doped HTL.

undoped, selective HTL is more critical for perovskite solar cells than for analogous organic solar cells.

Our analyses indicate that non-selective, heavily doped contacts, widely used in OPVs, are not desirable for PSCs. As lower doping levels reduce conductivity, the thickness of the HTL must be controlled to minimise series resistance losses. For example, for the devices studied in our work, increasing the thickness of the PTPD layer above 20 nm significantly reduced device FF and J_{SC}, whereas thickness variations of the PEDOT:PSS and doped PTAA layers did not cause appreciable degradation of device performance, **Figure 5.9**. The lower conductivity of the less p-doped HTLs can also be

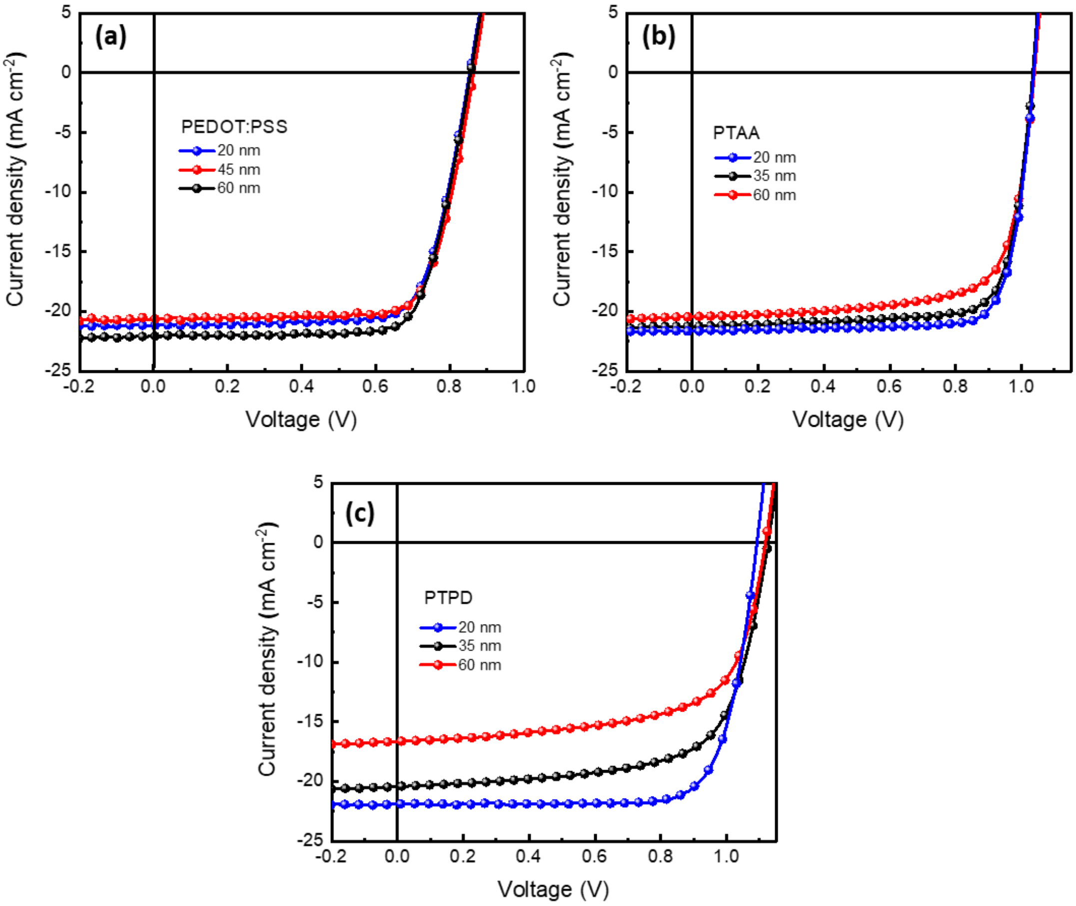

Figure 5.9 J-V characteristics of solar cells based on PEDOT:PSS, PTAA and PTPD with varied HTL thickness.

a potential problem for n-i-p PSCs where PTAA layer thicknesses much thicker than those explored herein can be required to effectively cover the perovskite active layer – hence in such circumstances doping of PTAA is typically required to improve conductivity. Interestingly extreme doping of PTAA with lithium salts in such devices has been reported to result in a > 200 mV loss in V_{OC},[159] a case analogous to our results.

Our observation that the best performing p-i-n PSC studied here exhibits the highest device PL efficiency, when measured under open circuit conditions, is comparable to observations in inorganic solar cells.[127,134,242] Under open circuit conditions, all charge must recombine in the device; a high PL efficiency measured under these conditions implies a suppression of undesirable non-radiative recombination losses, and thus an enhancement of bulk, radiative recombination. This observation is agreement with the trend in PL studies of neat perovskite films and with device electroluminescence studies, where in both cases higher emission intensities correlated with higher photovoltaic device performance.[110,204,236] Our observations are also consistent with a recent study by Wolff *et al,*[172] which showed that introducing a charge blocking layer at the perovskite/ETL interface resulted in enhanced bulk recombination relative to surface recombination, and yielded a higher V_{OC}. It is concluded that by suppressing surface recombination, and thus confining recombination to the absorber layer, higher device V_{OC} and PCE can be achieved. As such, minimizing bulk non-radiative recombination losses with in the MAPI layer, either by passivating bulk defects[132] or optimizing the perovskite composition,[162] as well as minimising recombination at the MAPI/ETL interface, should lead to further improvements in device performance.

6. Conclusions and Further Work

The last chapter aimed to summarise insights of the working principles of perovskite solar cells. I started by fabricating p-i-n perovskite solar cells with PEDOT:PSS as the HTL and PCBM as the ETL, with reference devices achieving a PCE of 14%. By improving film crystallinity the PCE was improved to 16.9% (Chapter 3), and was further improved to 17.4% through controlling microstructural defects in perovskite films (Chapter 4). In these two chapters the role of perovskite film quality, including crystallinity, orientation, *etc*, is clearly highlighted. However, these PCEs are still far behind the reported values of state-of-the-art PSCs. I then move on to replacing PEDOT:PSS with PTAA and PTPD while remaining MAPI film unchanged. A greater PCE improvement up to 19.6% is achieved, showing that modifying charge transport layers is more critical to improving device performance (Chapter 3).

6.1. Bulk Recombination *vs* Surface Recombination

The primary question addressed by this thesis is whether PSCs are dominated by bulk recombination loss or surface recombination loss. The answer is, both bulk recombination losses exist, but surface recombination appears to be more dominant. Although in Chapter 3 and 4 improvement of PCE enabled by controlling bulk recombination is shown, these devices still suffer great surface recombination due to the use of PEDOT:PSS – replacing PEDOT:PSS with PTAA or PTPD yields greater improvement of PCE, suggesting that surface recombination is the primary loss pathways in p-i-n PSCs.

Owing to sensitivity of processing methodology to the underlying HTLs, methods adopted in Chapter 3 and 4 to improve film quality is not applicable on PTAA or PTPD. Recently, we employed a post-treatment based on solvent annealing that can improve the crystallinity of perovskite film regardless of film processing methodology, show in **Figure 6.1 a** and **6.1 b** the PCE of devices with PTPD, PEDOT:PSS as HTLs and device no HTL, all comprising untreated and treated perovskite films. The devices are anticipated to suffer even greater surface recombination when HTL is removed. In all cases the post-treatment can improve device PCE, but more profound improvement is observed when the device comprises PEDOT:PSS and when HTL is removed. It shows that improving perovskite crystallinity in these devices increase their resistance against surface recombination. This observation, highlighted by the schematic drawing of **Figure 6.1 c**, consistent with our conclusion in chapter 5, implies that field screening by ionic defects in the low-crystallinity perovskite films is partially responsible for the vulnerability to surface recombination.

In addition, this study reveals PSCs exhibit apparently varied slope of n-V_{OC} (**Figure 5.7 b**) when HTL is altered – these variations are frequently observed in OSCs and are assigned to varied distribution of tail states in the photoactive layer.[256] The data herein highlights that the overall tail states distribution depends strongly on charge transport

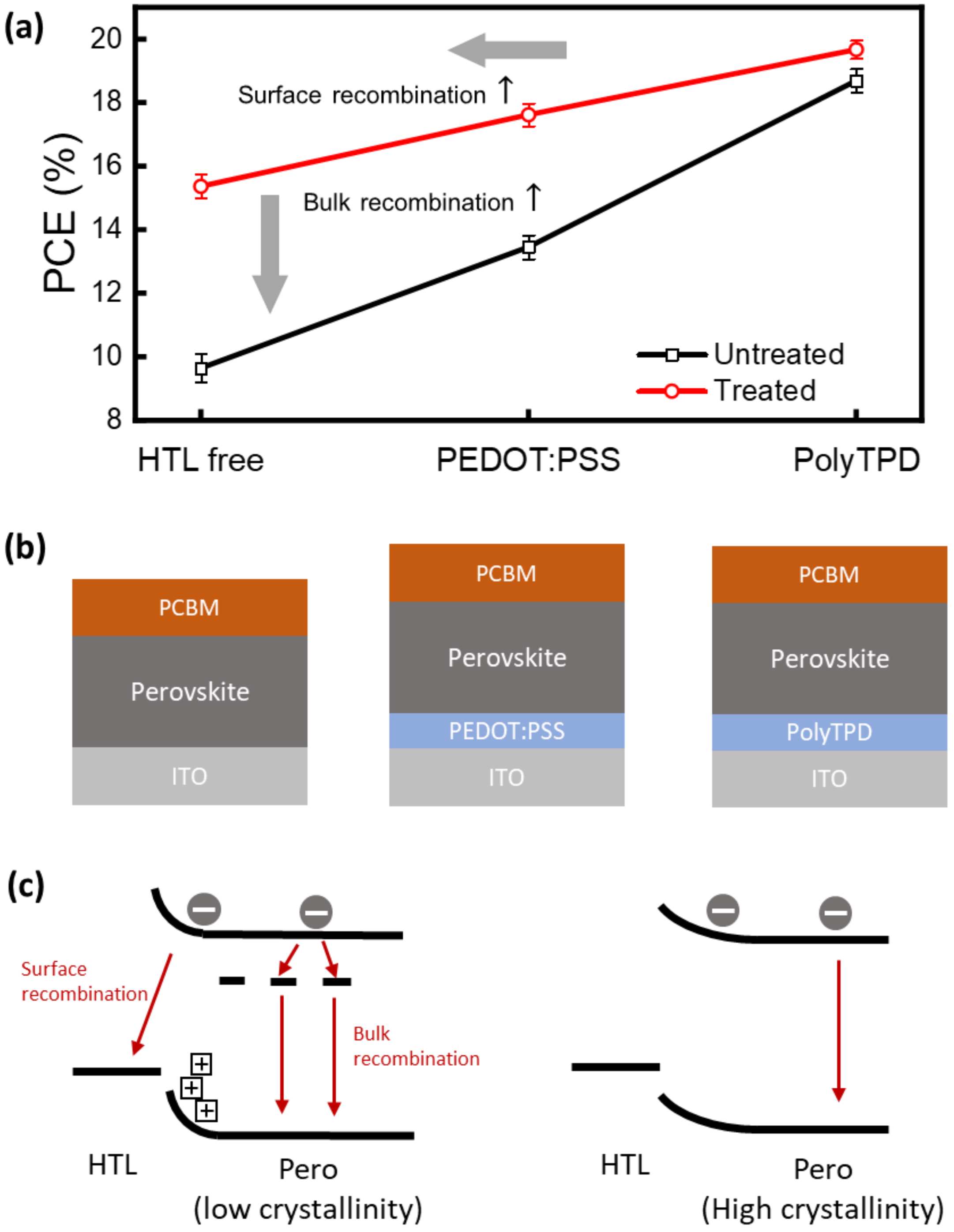

Figure 6.1 **(a)** PCE of devices with untreated perovskite films and treated perovskite films with improved crystallinity, both in devices with PTPD, PEDOT:PSS as HTL and in devices with no HTL. **(b)** Schematic drawing showing the layer composition in the PSC. **(c)** Schematic drawing the correlation of surface recombination/bulk recombination with crystallinity of perovskite films.

layers, and thus is an estimation of tail states or trap states in the full device instead of in the perovskite layer. In other words, electronic trap states in charge transport layers plays significant role in the energetics of full PSC. The lifetime derived from TPV measurement, **Figure 5.7 c**, exhibit greater dependence on HTL than on perovskite crystallinity. These results all support that surface recombination plays a greater role in determining the performance of p-i-n PSCs.

6.2. Re-interpretation of Photoluminescence Quenching

The study reveals the complexity in interpreting photoluminescence quenching data of a photoactive layer/charge transport layer heterojunction that was previously used to estimate charge transfer efficiency: it can be caused by surface recombination. The results in Chapter 5 clearly demonstrate PL quenching correlating to poor device performance. The ambiguity herein is possibly owing that the typical glass/HTL/perovskite sample configuration in PL measurement is equivalent to open circuit condition, in such case photoexcited charge carriers accumulate at the HTL/perovskite interfaces if surface recombination is minimised resulting in hindered charge transfer and bulk recombination. Previously such ambiguity can be resolved by probing the kinetics of the charge transport layers using nano-second TA spectroscopy,[136] where charge transfer kinetics and the following interfacial recombination kinetics can distinguished.

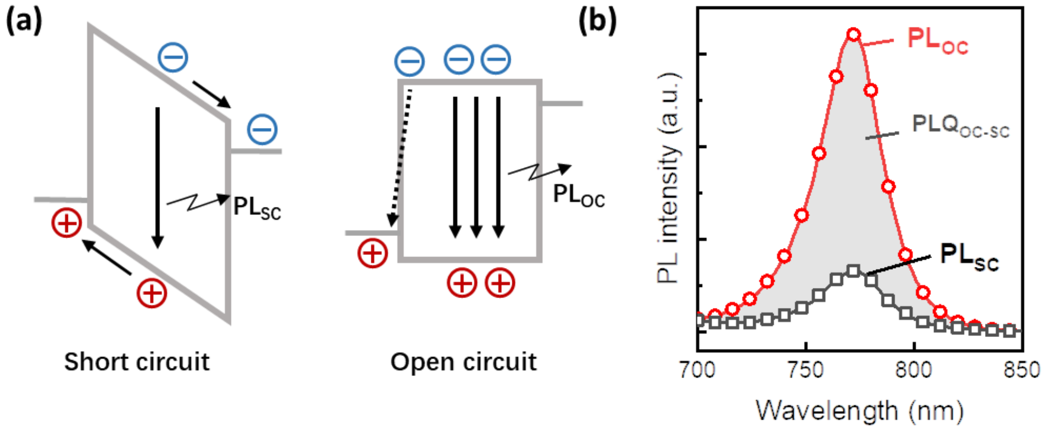

Figure 6.2 **(a)** Schematic drawing showing the origin of PL of a full PSC at open circuit and short circuit. **(b)** Typical PL spectra of a full PSC.

To resolve the ambiguity using PL spectroscopy of charge transfer and surface recombination we developed a methodology to measure PL emission of full device held between open circuit and short circuit. As highlighted in **Figure 6.2 a**, efficiency of charge extraction can be estimated by measuring the PL emission intensity at short circuit while non-radiative recombination loss is characterized by the PL at open circuit. Typical PL spectra is shown in **Figure 6.2 b**. The data in Chapter 5 reveals that PTPD and PEDOT:PSS show reasonably low but comparable PL at short circuit, contrasting the observation of bilayer PL emission, whereas a remarkable difference is seen at open circuit. High PL at open circuit confirms that charge carriers predominantly accumulate in perovskite layer.

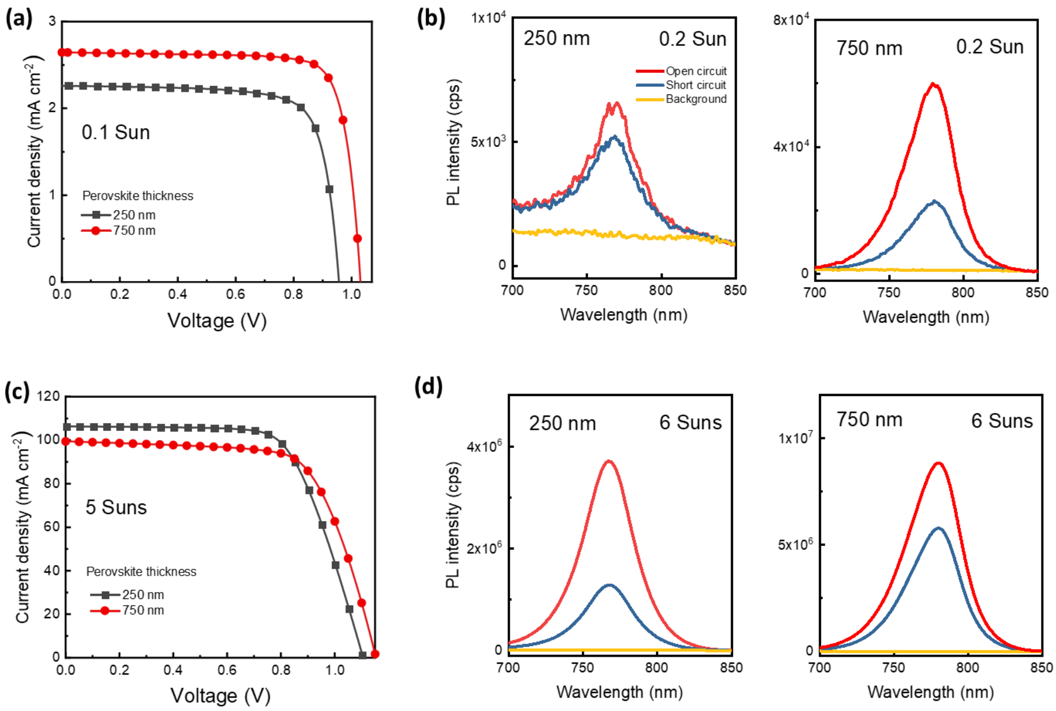

Figure 6.3 (a) J-V curves of two devices (with 250 nm and 750 nm perovskite films) under 0.1 Sun illumination. **(b)** Typical PL spectra of a full PSC under laser excitation with excitation intensity equivalent to 0.2 Sun. **(c), (d)** J-V curves under 5 Suns illumination and PL spectra with excitation intensity equivalent to 6 Suns.

The results highlight an issue that excellent PSCs show exhibit maximum PL at open circuit but minimum PL at short circuit, in accordance with classical photovoltaic principle. As such PSC operate more analogous to inorganic solar cells. In a broader context the interpretation PL quenching strongly depends whether the measured sample is close to open circuit or short circuit condition, in former case high quenching efficiency indicates non-radiative recombination loss while in later case it implies efficient charge extraction.

This method is adopted as an assay of charge extraction versus charge recombination complementary to conventional PL quenching assay. Its validity can be further testified by correlating the PCE of PSC with their PL_{OC}/PL_{SC} under different light intensities. **Figure 6.3** compares the J-V curves of two PSCs (with different perovskite thickness) against their PL spectra under low light level and high light level. It can be seen that the two devices exhibit contrasting behaviour depending on light intensity: the thick device show better performance under low light but poorer performance under high light. Interestingly, a consistent trend is shown by the PL spectra, that the thick device exhibit remarkable difference between PL_{OC} and PL_{OC} under low light, while such difference becomes less significant under high light. In accordance, the thin device exhibits contrast the same trend between PCE and PL can be seen in the thin device. The results herein, importantly, suggest that the performance of PSC is not only affected perovskite film thickness but also by light intensity, with these changes all correlating to variations of PL behaviours.

6.3. Further Work

The final section summarises a couple of unresolved issues in this study as potential further work:

Optimization of Device Fabrication and Performance

(i) PEDOT:PSS is a lost-cost hole transporting material with excellent processability despite its relatively poor device performance. Fabrication of high-quality thin-film perovskite may minimise the efficiency gap between PEDOT:PSS device and PTPD device, and thus making device PCE less sensitive to HTL. This would potentially bring PSC more analogous to inorganic solar cells.

(ii) Having realised the limited versatility of the processing modifications employed in this study (*i.e.* neither "MAI excess" nor "co-annealing" works for DE-dripping method due to change of solvent), it is critical to develop a strategy, most likely a post-treatment method, that is free from the influence of underlying substrates or deposition method adopted.

(iii) The impact of ETL should be studied provided that suitable electron transporting materials other than PCBM, such as non-fullerene acceptors, can be found.

Charge Carrier Dynamics

(i) In an attempt to distinguish charge transfer and surface/interfacial recombination, nano-second TAS system need to be developed to monitor charge carrier kinetics in the HTL or ETL.

(ii) Time-resolved PL spectroscopy should be carried out on HTL/perovskite/ETL triple-layer stacks or even full devices. The PL decay dynamics should be very different from those in bi-layer stacks. It is anticipated that the PL lifetime in triple-layer stacks should be very different from typically used bi-layer stacks and should be more relevant to charge recombination instead of charge extraction.

(iii) PL spectroscopy can be carried out in full devices under varied light intensity and varied applied bias. It would be interesting to measure PL emission intensity across the J-V curve.

(iv) It also remains unclear why TPV (up to microsecond) lifetime is much longer than typical lifetime of neat perovskite film (normally hundreds of nanosecond). In this case what is the role of spatial separation of charge in the full devices – this can be correlated to measurement of PL decay in a triple-layer stack.

References

1. Nelson, J. *The physics of solar cells*. vol. 57 (World Scientific, 2003).

2. Yin, W., Shi, T. & Yan, Y. Unique properties of halide perovskites as possible origins of the superior solar cell performance. *Adv. Mater.* **26**, 4653–4658 (2014).

3. Stoumpos, C. C., Malliakas, C. D. & Kanatzidis, M. G. Semiconducting Tin and Lead Iodide Perovskites with Organic Cations: Phase Transitions, High Mobilities, and Near-Infrared Photoluminescent Properties. *Inorg. Chem.* **52**, 9019–9038 (2013).

4. Mosconi, E., Amat, A., Nazeeruddin, M. K., Grätzel, M. & De Angelis, F. First-Principles Modeling of Mixed Halide Organometal Perovskites for Photovoltaic Applications. *J. Phys. Chem. C* **117**, 13902–13913 (2013).

5. Caprioglio, P. *et al.* On the Relation between the Open-Circuit Voltage and Quasi-Fermi Level Splitting in Efficient Perovskite Solar Cells. *Adv. Energy Mater.* **9**, (2019).

6. Kirchartz, T., Agostinelli, T., Campoy-Quiles, M., Gong, W. & Nelson, J. Understanding the Thickness-Dependent Performance of Organic Bulk Heterojunction Solar Cells: The Influence of Mobility, Lifetime, and Space Charge. *J. Phys. Chem. Lett.* **3**, 3470–3475 (2012).

7. Calado, P. *et al.* Evidence for ion migration in hybrid perovskite solar cells with minimal hysteresis. *Nat. Commun.* **7**, 13831 (2016).

8. Wang, Z. *et al.* High irradiance performance of metal halide perovskites for concentrator photovoltaics. *Nat. Energy* **3**, (2018).

9. Kim, J. *et al.* Excitation Density Dependent Photoluminescence Quenching and Charge Transfer Efficiencies in Hybrid Perovskite/Organic Semiconductor Bilayers. *Adv. Energy Mater.* **8**, 1802474 (2018).

10. Richter, J. M. *et al.* Enhancing photoluminescence yields in lead halide perovskites by photon recycling and light out-coupling. *Nat. Commun.* **7**, 13941 (2016).

11. Wu, X. *et al.* Trap states in lead iodide perovskites. *J. Am. Chem. Soc.* **137**,

2089–2096 (2015).

12. Wen, X. *et al.* Defect trapping states and charge carrier recombination in organic – inorganic halide. *J. Mater. Chem. C* **4**, 793–800 (2015).

13. Stranks, S. D. *et al.* Recombination Kinetics in Organic-Inorganic Perovskites: Excitons, Free Charge, and Subgap States. *Phys. Rev. Appl.* **2**, 1–8 (2014).

14. Yin, W.-J., Shi, T. & Yan, Y. Unusual defect physics in CH3NH3PbI3 perovskite solar cell absorber. *Appl. Phys. Lett.* **104**, 63903 (2014).

15. Tahara, H., Endo, M., Wakamiya, A. & Kanemitsu, Y. Experimental Evidence of Localized Shallow States in Orthorhombic Phase of CH3NH3PbI3 Perovskite Thin Films Revealed by Photocurrent Beat Spectroscopy. *J. Phys. Chem. C* **120**, 5347–5352 (2016).

16. deQuilettes, D. W. *et al.* Charge-Carrier Recombination in Halide Perovskites. *Chem. Rev.* **119**, 11007–11019 (2019).

17. Kahn, A. Fermi level, work function and vacuum level. *Mater. Horizons* **3**, 7–10 (2016).

18. Shuttle, C. G. *et al.* Bimolecular recombination losses in polythiophene: Fullerene solar cells. *Phys. Rev. B - Condens. Matter Mater. Phys.* **78**, 1–4 (2008).

19. Eames, C. *et al.* Ionic transport in hybrid lead iodide perovskite solar cells. *Nat. Commun.* **6**, (2015).

20. Planck, M. On the law of distribution of energy in the normal spectrum. *Ann. Phys.* **4**, 1 (1901).

21. Gottschalg, R. *The solar resource and the fundamentals of solar radiation for renewable energy systems*. (Sci-Notes, 2001).

22. Laue, E. G. The measurement of solar spectral irradiance at different terrestrial elevations. *Sol. Energy* **13**, 43–57 (1970).

23. Perez, R., Ineichen, P., Seals, R., Michalsky, J. & Stewart, R. Modeling daylight availability and irradiance components from direct and global irradiance. *Sol. energy* **44**, 271–289 (1990).

24. Bird, R. E. & Riordan, C. Simple solar spectral model for direct and diffuse irradiance on horizontal and tilted planes at the earth's surface for cloudless atmospheres. *J. Clim. Appl. Meteorol.* **25**, 87–97 (1986).

25. Kim, Y. C. *et al.* Printable organometallic perovskite enables large-area, low-dose X-ray imaging. *Nature* **550**, 87–91 (2017).

26. Shockley, W. & Queisser, H. J. Detailed balance limit of efficiency of p-n junction solar cells. *J. Appl. Phys.* **32**, 510–519 (1961).

27. Goetzberger, A., Knobloch, J. & Voss, B. Crystalline silicon solar cells. *New York* 114–118 (1998).

28. Wang, X., Khan, M. R., Gray, J. L., Alam, M. A. & Lundstrom, M. S. Design of GaAs solar cells operating close to the Shockley–Queisser limit. *IEEE J. Photovoltaics* **3**, 737–744 (2013).

29. Blakemore, J. S. Semiconducting and other major properties of gallium arsenide. *J. Appl. Phys.* **53**, R123–R181 (1982).

30. Deb, S. K. Thin-film solar cells: an overview. *Renew. energy* **8**, 69–92 (1996).

31. Carlson, D. E. & Wronski, C. R. Amorphous silicon solar cell. *Appl. Phys. Lett.* **28**, 671–673 (1976).

32. Ferekides, C. S. *et al.* High efficiency CSS CdTe solar cells. *Thin Solid Films* **361**, 520–526 (2000).

33. Naghavi, N., Spiering, S., Powalla, M., Cavana, B. & Lincot, D. High-efficiency copper indium gallium diselenide (CIGS) solar cells with indium sulfide buffer layers deposited by atomic layer chemical vapor deposition (ALCVD). *Prog. Photovoltaics Res. Appl.* **11**, 437–443 (2003).

34. Grätzel, M. Dye-sensitized solar cells. *J. Photochem. Photobiol. C Photochem. Rev.* **4**, 145–153 (2003).

35. O'Regan, B. & Gratzel, M. A low-cost, high-efficiency solar cell based on dye-sensitized colloidal TiO2 films. *Nature* **353**, 737–740 (1991).

36. Dennler, G., Scharber, M. C. & Brabec, C. J. Polymer-fullerene bulk-heterojunction solar cells. *Adv. Mater.* **21**, 1323–1338 (2009).

37. Hoppe, H. & Sariciftci, N. S. Organic solar cells: An overview. *J. Mater. Res.* **19**, 1924–1945 (2004).

38. Tvingstedt, K. *et al.* Radiative efficiency of lead iodide based perovskite solar cells. *Sci. Rep.* **4**, 1–7 (2014).

39. Kojima, A., Teshima, K., Shirai, Y. & Miyasaka, T. Organometal Halide Perovskites as Visible-Light Sensitizers for Photovoltaic Cells. *J. Am. Chem. Soc.* **131**, 6050–6051 (2009).

40. Im, J.-H., Lee, C.-R., Lee, J.-W., Park, S.-W. & Park, N.-G. 6.5% efficient perovskite quantum-dot-sensitized solar cell. *Nanoscale* **3**, 4088–4093 (2011).

41. Kim, H.-S. *et al.* Lead iodide perovskite sensitized all-solid-state submicron thin film mesoscopic solar cell with efficiency exceeding 9%. *Sci. Rep.* **2**, (2012).

42. Zhou, H. *et al.* Interface engineering of highly efficient perovskite solar cells. *Science (80-.).* **345**, 542–546 (2014).

43. Best Research-Cell Efficiencies Rev. 01-03-2019 (NREL, 2019); https://www.nrel.gov/pv/assets/pdfs/pv-efficiency-chart.20190103.

44. Lee, M. M., Teuscher, J., Miyasaka, T., Murakami, T. N. & Snaith, H. J. Efficient Hybrid Solar Cells Based on Meso-Superstructured Organometal Halide Perovskites. *Science.* **338**, 643–647 (2012).

45. Liu, M., Johnston, M. B. & Snaith, H. J. Efficient planar heterojunction perovskite solar cells by vapour deposition. *Nature* **501**, 395–398 (2013).

46. Jeng, J. Y. *et al.* CH3NH3PbI3 Perovskite/Fullerene Planar-Heterojunction Hybrid Solar Cells. *Adv. Mater.* **25**, 3727–3732 (2013).

47. Bush, K. A. *et al.* 23.6%-Efficient Monolithic Perovskite/Silicon Tandem Solar Cells With Improved Stability. *Nat. Energy* **2**, 1–7 (2017).

48. Schaak, R. E. & Mallouk, T. E. Perovskites by Design: A Toolbox of Solid-State Reactions. *Chem. Mater.* **14**, 1455–1471 (2002).

49. Porterfield, W. W. *Inorganic chemistry.* (Academic press, 2013).

50. Sato, T., Takagi, S., Deledda, S., Hauback, B. C. & Orimo, S. Extending the

applicability of the Goldschmidt tolerance factor to arbitrary ionic compounds. *Sci. Rep.* **6**, 23592 (2016).

51. Lee, J. W. *et al.* Formamidinium and cesium hybridization for photo- and moisture-stable perovskite solar cell. *Adv. Energy Mater.* **5**, (2015).

52. Weller, M. T., Weber, O. J., Henry, P. F., Di Pumpo, A. M. & Hansen, T. C. Complete structure and cation orientation in the perovskite photovoltaic methylammonium lead iodide between 100 and 352 K. *Chem. Commun.* **51**, 4180–4183 (2015).

53. Onoda-Yamamuro, N., Matsuo, T. & Suga, H. Calorimetric and IR spectroscopic studies of phase transitions in methylammonium trihalogenoplumbates. *J. Phys. Chem. Solids* **51**, 1383–1395 (1990).

54. Onoda-Yamamuro, N., Yamamuro, O., Matsuo, T. & Suga, H. p-T phase relations of CH 3 NH 3 PbX 3 (X= Cl, Br, I) crystals. *J. Phys. Chem. Solids* **53**, 277–281 (1992).

55. Oku, T. Crystal Structures of CH3NH3PbI3 and Related Perovskite Compounds Used for Solar Cells. *Sol. Cells - New Approaches Rev.* (2015) doi:10.5772/59284.

56. Chang, Y. H., Park, C. H. & Matsuishi, K. First-principles study of the Structural and the electronic properties of the lead-Halide-based inorganic-organic perovskites (CH~ 3NH~ 3) PbX~ 3 and CsPbX~ 3 (X= Cl, Br, I). *Journal-Korean Phys. Soc.* **44**, 889–893 (2004).

57. Brivio, F., Walker, A. B. & Walsh, A. Structural and electronic properties of hybrid perovskites for high-efficiency thin-film photovoltaics from first-principles. *APL Mater.* **1**, (2013).

58. Walsh, A. & Watson, G. W. The origin of the stereochemically active Pb (II) lone pair: DFT calculations on PbO and PbS. *J. Solid State Chem.* **178**, 1422–1428 (2005).

59. Giorgi, G., Fujisawa, J. I., Segawa, H. & Yamashita, K. Small photocarrier effective masses featuring ambipolar transport in methylammonium lead iodide perovskite: A density functional analysis. *J. Phys. Chem. Lett.* **4**, 4213–4216 (2013).

60. Miyata, A. *et al.* Direct measurement of the exciton binding energy and

effective masses for charge carriers in organic-inorganic tri-halide perovskites. *Nat. Phys.* **11**, 582–587 (2015).

61. Wolf, S. de *et al.* Organometallic Halide Perovskites: Sharp Optical Absorption Edge and Its Relation to Photovoltaic Performance. *J. Phys. Chem. C* **5**, 1035–139 (2014).

62. Seeger, K. *Semiconductor physics*. (Springer Science & Business Media, 2013).

63. West, A. R. *Solid state chemistry and its applications*. (John Wiley & Sons, 2014).

64. Queisser, H. J. & Haller, E. E. Defects in Semiconductors : Some Fatal , Some Vital.

65. Ball, J. M. & Petrozza, A. Defects in perovskite-halides and their effects in solar cells. *Nat. Energy* **1**, (2016).

66. Mahajan, S. Defects in semiconductors and their effects on devices. *Acta Mater.* **48**, 137–149 (2000).

67. Kim, J., Lee, S. H., Lee, J. H. & Hong, K. H. The role of intrinsic defects in methylammonium lead iodide perovskite. *J. Phys. Chem. Lett.* **5**, 1312–1317 (2014).

68. Yuan, Y. *et al.* Photovoltaic Switching Mechanism in Lateral Structure Hybrid Perovskite Solar Cells. *Adv. Energy Mater.* **5**, 1–7 (2015).

69. Juarez-Perez, E. J. *et al.* Photoinduced Giant Dielectric Constant in Lead Halide Perovskite Solar Cells. *J. Phys. Chem. Lett.* **5**, 2390–2394 (2014).

70. Frost, J. M. & Walsh, A. What Is Moving in Hybrid Halide Perovskite Solar Cells? *Acc. Chem. Res.* **49**, 528–535 (2016).

71. Li, C. *et al.* Iodine Migration and its Effect on Hysteresis in Perovskite Solar Cells. *Adv. Mater.* **28**, 2446–2454 (2016).

72. Bai, S. *et al.* Planar perovskite solar cells with long-term stability using ionic liquid additives. *Nature* **571**, 245–250 (2019).

73. Leijtens, T. *et al.* Mapping Electric Field-Induced Switchable Poling and

Structural Degradation in Hybrid Lead Halide Perovskite Thin Films. *Adv. Energy Mater.* **5**, 1500962 (2015).

74. Belisle, R. A. *et al.* Interpretation of inverted photocurrent transients in organic lead halide perovskite solar cells: proof of the field screening by mobile ions and determination of the space charge layer widths. *Energy Environ. Sci.* **10**, 192–204 (2017).

75. Pockett, A. & Carnie, M. J. Ionic Influences on Recombination in Perovskite Solar Cells. *ACS Energy Lett.* **2**, 1683–1689 (2017).

76. Calado, P. *et al.* Identifying Dominant Recombination Mechanisms in Perovskite Solar Cells by Measuring the Transient Ideality Factor. *Phys. Rev. Appl.* **11**, 1 (2019).

77. Bergmann, V. W. *et al.* Real-space observation of unbalanced charge distribution inside a perovskite-sensitized solar cell. *Nat. Commun.* **5**, 5001 (2014).

78. Snaith, H. J. *et al.* Anomalous Hysteresis in Perovskite Solar Cells. *J. Phys. Chem. Lett.* **5**, 1511–1515 (2014).

79. Van Reenen, S., Kemerink, M. & Snaith, H. J. Modeling Anomalous Hysteresis in Perovskite Solar Cells. *J. Phys. Chem. Lett.* **6**, 3808–3814 (2015).

80. Richardson, G. *et al.* Can slow-moving ions explain hysteresis in the current–voltage curves of perovskite solar cells? *Energy Environ. Sci.* **9**, 1476–1485 (2016).

81. Meloni, S. *et al.* Ionic polarization-induced current–voltage hysteresis in CH3NH3PbX3 perovskite solar cells. *Nat. Commun.* **7**, 10334 (2016).

82. Tress, W., Leo, K. & Riede, M. Influence of hole-transport layers and donor materials on open-circuit voltage and shape of I-V curves of organic solar cells. *Adv. Funct. Mater.* **21**, 2140–2149 (2011).

83. Guerrero, A. *et al.* Interfacial degradation of planar lead halide perovskite solar cells. *ACS Nano* **10**, 218–224 (2016).

84. Lee, J. *et al.* Achieving Large-Area Planar Perovskite Solar Cells by Introducing an Interfacial Compatibilizer. **1606363**, 1–8 (2017).

85. Jeon, N. J. *et al.* Solvent engineering for high-performance inorganic–organic hybrid perovskite solar cells. *Nat. Mater.* **13**, 897–903 (2014).

86. Jeon, N. J. *et al.* Solvent engineering for high-performance inorganic-organic hybrid perovskite solar cells. *Nat. Mater.* **13**, 897–903 (2014).

87. Miyamae, H., Numahata, Y. & Nagata, M. The crystal structure of lead (II) iodide-dimethylsulphoxide (1/2), PbI2 (dmso) 2. *Chem. Lett.* **9**, 663–664 (1980).

88. Reimer, L. *Scanning electron microscopy: physics of image formation and microanalysis*. vol. 45 (Springer, 2013).

89. Flegler, S. L. & Flegler, S. L. *Scanning & Transmission Electron Microscopy*. (Oxford University Press, 1997).

90. Evekhart, T. E., Wells, O. O. & Oatley, C. W. Factors affecting contrast and resolution in the scanning electron microscope. *Int. J. Electron.* **7**, 97–111 (1959).

91. Jenkins, R. & Snyder, R. L. *Introduction to X-ray powder diffractometry*. vol. 138 (Wiley New York, 1996).

92. Williams, D. B. & Carter, C. B. The transmission electron microscope. in *Transmission electron microscopy* 3–17 (Springer, 1996).

93. Champness, P. E. *Electron diffraction in the transmission electron microscope*. vol. 47 (Bios Scientific, 2001).

94. Buseck, P., Cowley, J. & Eyring, L. *High-Resolution Transmission Electron Microscopy: And Associated Techniques*. (Oxford University Press, 1989).

95. Crewe, A. V, Wall, J. & Welter, L. M. A high-resolution scanning transmission electron microscope. *J. Appl. Phys.* **39**, 5861–5868 (1968).

96. Dellby, N., Krivanek, L., Nellist, D., Batson, E. & Lupini, R. Progress in aberration-corrected scanning transmission electron microscopy. *Microscopy* **50**, 177–185 (2001).

97. Ishitani, T., Tsuboi, H., Yaguchi, T. & Koike, H. Transmission electron microscope sample preparation using a focused ion beam. *Microscopy* **43**, 322–326 (1994).

98. Jauncey, G. E. M. The scattering of x-rays and Bragg's law. *Proc. Natl. Acad. Sci. U. S. A.* **10**, 57 (1924).

99. Warren, B. E. *X-ray Diffraction*. (Courier Dover Publications, 1969).

100. Swanson, H. E. *Standard X-ray diffraction powder patterns*. vol. 1 (US Department of Commerce, National Bureau of Standards, 1953).

101. Docampo, P. *et al.* Influence of the orientation of methylammonium lead iodide perovskite crystals on solar cell performance. *APL Mater.* **2**, (2014).

102. Wadsworth, A. *et al.* Highly Efficient and Reproducible Nonfullerene Solar Cells from Hydrocarbon Solvents. *ACS Energy Lett.* **2**, 1494–1500 (2017).

103. Kim, Y. C. *et al.* Engineering interface structures between lead halide perovskite and copper phthalocyanine for efficient and stable perovskite solar cells. *Energy Environ. Sci.* **10**, 2109–2116 (2017).

104. Giesbrecht, N. *et al.* Synthesis of Perfectly Oriented and Micrometer-Sized MAPbBr 3 Perovskite Crystals for Thin Film Photovoltaic Applications. *ACS Energy Lett.* acsenergylett.6b00050 (2016) doi:10.1021/acsenergylett.6b00050.

105. Melitz, W., Shen, J., Kummel, A. C. & Lee, S. Kelvin probe force microscopy and its application. *Surf. Sci. Rep.* **66**, 1–27 (2011).

106. Zhang, W. *et al.* Enhanced optoelectronic quality of perovskite thin films with hypophosphorous acid for planar heterojunction solar cells. *Nat. Commun.* **6**, (2015).

107. Gilliland, G. D. *Photoluminescence spectroscopy of crystalline semiconductors*. *Materials Science and Engineering: R: Reports* vol. 18 (1997).

108. D., B. *et al.* Efficient luminescent solar cells based on tailored mixed-cation perovskites. *Sci. Adv.* **2**, e1501170 (2016).

109. Sutter-Fella, C. M. *et al.* High Photoluminescence Quantum Yield in Band Gap Tunable Bromide Containing Mixed Halide Perovskites. *Nano Lett.* **16**, 800–806 (2015).

110. Du, T. *et al.* Elucidating the Origins of Subgap Tail States and Open-Circuit Voltage in Methylammonium Lead Triiodide Perovskite Solar Cells. *Adv.*

Funct. Mater. **28**, 1801808 (2018).

111. Fang, H.-H., Wang, F., Adjokatse, S., Zhao, N. & Loi, M. A. Photoluminescence Enhancement in Formamidinium Lead Iodide Thin Films. *Adv. Funct. Mater.* **26**, 4653–4659 (2016).

112. Richter, J. M. *et al.* Enhancing photoluminescence yields in lead halide perovskites by photon recycling and light out-coupling. *Nat. Commun.* **7**, (2016).

113. Wang, J. T.-W. *et al.* Efficient Perovskite Solar Cells by Metal Ion Doping. *Energy Environ. Sci.* **9**, 2892–2901 (2016).

114. Abdi-Jalebi, M. *et al.* Maximizing and stabilizing luminescence from halide perovskites with potassium passivation. *Nature* **555**, 497–501 (2018).

115. 2018-NE-Visualization and suppression of interfacial recombination for high-efficiency large-area pin perovskite solar cells.pdf.

116. Hoke, E. T. *et al.* Reversible photo-induced trap formation in mixed-halide hybrid perovskites for photovoltaics. *Chem. Sci.* **6**, 613–617 (2015).

117. DeQuilettes, D. W. *et al.* Photo-induced halide redistribution in organic-inorganic perovskite films. *Nat. Commun.* **7**, (2016).

118. Chen, S. *et al.* Mobile Ion Induced Slow Carrier Dynamics in Organic-Inorganic Perovskite CH3NH3PbBr3. *ACS Appl. Mater. Interfaces* **8**, 5351–5357 (2016).

119. Sheng, R. *et al.* Photoluminescence characterisations of a dynamic aging process of organic-inorganic CH3NH3PbBr3 perovskite. *Nanoscale* **8**, 1926–1931 (2016).

120. Steele, J. A. *et al.* Role of Electron-Phonon Coupling in the Thermal Evolution of Bulk Rashba-Like Spin-Split Lead Halide Perovskites Exhibiting Dual-Band Photoluminescence. *ACS Energy Lett.* **4**, 2205–2212 (2019).

121. Fang, X. *et al.* Effect of excess PbBr2 on photoluminescence spectra of CH3NH3PbBr3 perovskite particles at room temperature. *Appl. Phys. Lett.* **108**, 071109 (2016).

122. van Franeker, J. J. *et al.* Monitoring Thermal Annealing of Perovskite Solar

Cells with In Situ Photoluminescence. *Adv. Energy Mater.* **7**, 1601822 (2017).

123. Kong, W. *et al.* Characterization of an abnormal photoluminescence behavior upon crystal-phase transition of perovskite CH3NH3PbI3. *Phys. Chem. Chem. Phys.* **17**, 16405–11 (2015).

124. Shirakata, S. & Nakada, T. Photoluminescence and time-resolved photoluminescence in Cu(In, Ga)Se 2 thin films and solar cells. *Phys. Status Solidi Curr. Top. Solid State Phys.* **6**, 1059–1062 (2009).

125. Du, T. *et al.* p-Doping of organic hole transport layers in p–i–n perovskite solar cells: correlating open-circuit voltage and photoluminescence quenching. *J. Mater. Chem. A* **7**, 18971–18979 (2019).

126. Trupke, T., Bardos, R. A., Abbott, M. D. & Cotter, J. E. Suns-photoluminescence: Contactless determination of current-voltage characteristics of silicon wafers. *Appl. Phys. Lett.* **87**, 1–4 (2005).

127. Shirakata, S. & Nakada, T. Time-resolved photoluminescence in Cu(In,Ga)Se2thin films and solar cells. *Thin Solid Films* **515**, 6151–6154 (2007).

128. Ferraioli, L., Maddalena, P., Parretta, A., Wang, A. & Zhao, J. Current-voltage characteristics of high-efficiency silicon solar cells from photoluminescence. *Appl. Phys. Lett.* **85**, 4222–4224 (2004).

129. O'Connor, D. *Time-correlated single photon counting*. (Academic Press, 2012).

130. Yamada, Y., Yamada, T., Shimazaki, A., Wakamiya, A. & Kanemitsu, Y. Interfacial Charge-Carrier Trapping in CH3NH3PbI3-Based Heterolayered Structures Revealed by Time-Resolved Photoluminescence Spectroscopy. *J. Phys. Chem. Lett.* **7**, 1972–1977 (2016).

131. Brenes, R. *et al.* Metal Halide Perovskite Polycrystalline Films Exhibiting Properties of Single Crystals. *Joule* **1**, 155–167 (2017).

132. Zheng, X. *et al.* Defect passivation in hybrid perovskite solar cells using quaternary ammonium halide anions and cations. *Nat. Energy* **2**, 17102 (2017).

133. Bai, Y. *et al.* Oligomeric Silica-Wrapped Perovskites Enable Synchronous Defect Passivation and Grain Stabilization for Efficient and Stable Perovskite

Photovoltaics. *ACS Energy Lett.* **4**, 1231–1240 (2019).

134. Metzger, W. K. *et al.* Time-resolved photoluminescence studies of CdTe solar cells. *J. Appl. Phys.* **94**, 3549–3555 (2003).

135. Xing, G. *et al.* Long-Range Balanced Electron- and Hole-Transport Lengths in Organic-Inorganic CH3NH3PbI3. *Science (80-.).* **342**, 344–347 (2013).

136. Haque, S. A. *et al.* Charge separation versus recombination in dye-sensitized nanocrystalline solar cells: The minimization of kinetic redundancy. *J. Am. Chem. Soc.* **127**, 3456–3462 (2005).

137. Hutter, E. M., Kirchartz, T., Ehrler, B., Cahen, D. & Von Hauff, E. Pitfalls and prospects of optical spectroscopy to characterize perovskite-transport layer interfaces. *Appl. Phys. Lett.* **116**, (2020).

138. Stolterfoht, M. *et al.* Voltage-Dependent Photoluminescence and How It Correlates with the Fill Factor and Open-Circuit Voltage in Perovskite Solar Cells. *ACS Energy Lett.* **4**, 2887–2892 (2019).

139. Eisner, F. D. *et al.* Hybridization of Local Exciton and Charge-Transfer States Reduces Nonradiative Voltage Losses in Organic Solar Cells. *J. Am. Chem. Soc.* **141**, 6362–6374 (2019).

140. Berera, R., van Grondelle, R. & Kennis, J. T. M. Ultrafast transient absorption spectroscopy: Principles and application to photosynthetic systems. *Photosynth. Res.* **101**, 105–118 (2009).

141. Manser, J. S. & Kamat, P. V. Band filling with free charge carriers in organometal halide perovskites. *Nat. Photonics* **8**, Ahead of Print (2014).

142. Stranks, S. D. *et al.* Electron-Hole Diffusion Lengths Exceeding 1 Micrometer in an Organometal Trihalide Perovskite Absorber. *Science* **342**, 341–344 (2014).

143. Shuttle, C. G. *et al.* Experimental determination of the rate law for charge carrier decay in a polythiophene: Fullerene solar cell. *Appl. Phys. Lett.* **92**, 90–93 (2008).

144. Sum, T. C. *et al.* Spectral Features and Charge Dynamics of Lead Halide Perovskites: Origins and Interpretations. *Acc. Chem. Res.* **49**, 294–302 (2016).

145. Barnes, P. R. F. *et al.* Interpretation of optoelectronic transient and charge extraction measurements in dye-sensitized solar cells. *Adv. Mater.* **25**, 1881–1922 (2013).

146. Kiermasch, D., Baumann, A., Fischer, M., Dyakonov, V. & Tvingstedt, K. Revisiting lifetimes from transient electrical characterization of thin film solar cells; A capacitive concern evaluated for silicon, organic and perovskite devices. *Energy Environ. Sci.* **11**, 629–640 (2018).

147. O'Regan, B. C. *et al.* Optoelectronic studies of methylammonium lead iodide perovskite solar cells with mesoporous TiO<inf>2</inf>: Separation of electronic and chemical charge storage, understanding two recombination lifetimes, and the evolution of band offsets during J - V hysteresis. *J. Am. Chem. Soc.* **137**, 5087–5099 (2015).

148. Wheeler, S. *et al.* Transient Optoelectronic Analysis of the Impact of Material Energetics and Recombination Kinetics upon the Open-Circuit Voltage of Hybrid Perovskite Solar Cells. *J. Phys. Chem. C* **121**, 13496–13506 (2017).

149. Kirchartz, T. & Nelson, J. Meaning of reaction orders in polymer:fullerene solar cells. *Phys. Rev. B - Condens. Matter Mater. Phys.* **86**, 1–12 (2012).

150. Kirchartz, T., Deledalle, F., Tuladhar, P. S., Durrant, J. R. & Nelson, J. On the differences between dark and light ideality factor in polymer:Fullerene solar cells. *J. Phys. Chem. Lett.* **4**, 2371–2376 (2013).

151. Kirchartz, T., Pieters, B. E., Kirkpatrick, J., Rau, U. & Nelson, J. Recombination via tail states in polythiophene:fullerene solar cells. *Phys. Rev. B - Condens. Matter Mater. Phys.* **83**, 1–13 (2011).

152. Tress, W. *et al.* Interpretation and Evolution of Open-Circuit Voltage, Recombination, Ideality Factor and Subgap Defect States during Reversible Light-Soaking and Irreversible Degradation of Perovskite Solar Cells. *Energy Environ. Sci.* **11**, 151–165 (2018).

153. Lenes, M., Morana, M., Brabec, C. J. & Blom, P. W. M. Recombination-limited photocurrents in low bandgap polymer/fullerene solar cells. *Adv. Funct. Mater.* **19**, 1106–1111 (2009).

154. Hristov, B. Quantifying Bimolecular Recombination Losses in Organic Bulk Heterojunction Solar Cells. *Silva Balc.* **15**, 50–57 (2014).

155. Koster, L. J. A., Mihailetchi, V. D., Xie, H. & Blom, P. W. M. Origin of the light intensity dependence of the short-circuit current of polymer/fullerene solar cells. *Appl. Phys. Lett.* **87**, 1–3 (2005).

156. Stolterfoht, M. *et al.* Photocarrier drift distance in organic solar cells and photodetectors. *Sci. Rep.* **5**, (2015).

157. Correa-Baena, J.-P. *et al.* The rapid evolution of highly efficient perovskite solar cells. *Energy Environ. Sci.* **10**, 710–727 (2017).

158. Tress, W. Perovskite Solar Cells on the Way to Their Radiative Efficiency Limit – Insights Into a Success Story of High Open-Circuit Voltage and Low Recombination. *Adv. Energy Mater.* **7**, 1602358 (2017).

159. Correa-Baena, J.-P. *et al.* Identifying and suppressing interfacial recombination to achieve high open-circuit voltage in perovskite solar cells. *Energy Environ. Sci.* **10**, 1207–1212 (2017).

160. Yao, J. *et al.* Quantifying losses in open-circuit voltage in solution-processable solar cells. *Phys. Rev. Appl.* **4**, 1–10 (2015).

161. Stranks, S. D. Nonradiative Losses in Metal Halide Perovskites. *ACS Energy Lett.* **2**, 1515–1525 (2017).

162. Saliba, M. *et al.* Cesium-containing triple cation perovskite solar cells: improved stability, reproducibility and high efficiency. *Energy Environ. Sci.* **9**, 1989–1997 (2016).

163. Tao, C. *et al.* Fully Solution-Processed n–i–p-Like Perovskite Solar Cells with Planar Junction: How the Charge Extracting Layer Determines the Open-Circuit Voltage. *Adv. Mater.* **29**, 1604493 (2017).

164. Seo, J. *et al.* Benefits of very thin PCBM and LiF layers for solution-processed p–i–n perovskite solar cells. *Energy Environ. Sci.* **7**, 2642 (2014).

165. Jeng, J.-Y. *et al.* CH3NH3PbI3 Perovskite/Fullerene Planar-Heterojunction Hybrid Solar Cells. *Adv. Mater.* **25**, 3727–3732 (2013).

166. Liu, D. *et al.* Improved Performance of Inverted Planar Perovskite Solar Cells with F4-TCNQ Doped PEDOT:PSS Hole Transport Layer. *J. Mater. Chem. A* **5**, 5701–5708 (2017).

167. Zhao, D. *et al.* High-efficiency solution-processed planar perovskite solar cells with a polymer hole transport layer. *Adv. Energy Mater.* **5**, 1–5 (2015).

168. Bi, C. *et al.* Non-wetting surface-driven high-aspect-ratio crystalline grain growth for efficient hybrid perovskite solar cells. *Nat. Commun.* **6**, 7747 (2015).

169. Park, J. H. *et al.* Efficient CH3NH3PbI3 Perovskite Solar Cells Employing Nanostructured p-Type NiO Electrode Formed by a Pulsed Laser Deposition. *Adv. Mater.* **27**, 4013–4019 (2015).

170. Chen, S. *et al.* Exploring the Limiting Open-Circuit Voltage and the Voltage Loss Mechanism in Planar CH3NH3PbBr3 Perovskite Solar Cells. *Adv. Energy Mater.* **6**, 1–9 (2016).

171. Shao, Y., Yuan, Y. & Huang, J. Correlation of energy disorder and open-circuit voltage in hybrid perovskite solar cells. *Nat. Energy* **1**, 15001 (2016).

172. Wolff, C. M. *et al.* Reduced Interface-Mediated Recombination for High Open-Circuit Voltages in CH3NH3PbI3Solar Cells. *Adv. Mater.* **29**, 1–8 (2017).

173. Kim, H.-S. *et al.* Mechanism of carrier accumulation in perovskite thin-absorber solar cells. *Nat Commun* **4**, 2242 (2013).

174. Zheng, X. *et al.* Defect passivation in hybrid perovskite solar cells using quaternary ammonium halide anions and cations. *Nat. Energy* **2**, 17102 (2017).

175. Yamada, Y., Nakamura, T., Endo, M., Wakamiya, A. & Kanemitsu, Y. Photocarrier recombination dynamics in perovskite CH3NH3PbI3 for solar cell applications. *J. Am. Chem. Soc.* **136**, 11610–3 (2014).

176. Shao, S. *et al.* The Effect of the Microstructure on Trap-Assisted Recombination and Light Soaking Phenomenon in Hybrid Perovskite Solar Cells. *Adv. Funct. Mater.* **26**, 8094–8102 (2016).

177. Leijtens, T. *et al.* Carrier trapping and recombination: the role of defect physics in enhancing the open circuit voltage of metal halide perovskite solar cells. *Energy Environ. Sci.* **9**, 3472–3481 (2016).

178. Wright, A. D. *et al.* Band-Tail Recombination in Hybrid Lead Iodide Perovskite. *Adv. Funct. Mater.* **27**, 1–8 (2017).

179. Kim, Y. C. *et al.* Beneficial Effects of PbI2 Incorporated in Organo-Lead Halide Perovskite Solar Cells. *Adv. Energy Mater.* **6**, 1502104 (2015).

180. You, J. *et al.* Moisture assisted perovskite film growth for high performance solar cells. *Appl. Phys. Lett.* **105**, 183902 (2014).

181. Nie, W. *et al.* High-efficiency solution-processed perovskite solar cells with millimeter-scale grains. *Science.* **347**, 522–525 (2015).

182. Qiu, W. *et al.* Pinhole-free perovskite films for efficient solar modules. *Energy Environ. Sci.* **9**, 484–489 (2016).

183. Lee, Y. H. *et al.* Unraveling the Reasons for Efficiency Loss in Perovskite Solar Cells. *Adv. Funct. Mater.* (2015).

184. Jeon, N. J. *et al.* Solvent engineering for high-performance inorganic–organic hybrid perovskite solar cells. *Nat Mater* **13**, 897–903 (2014).

185. Du, T. *et al.* Formation, location and beneficial role of PbI 2 in lead halide perovskite solar cells. *Sustain. Energy Fuels* **1**, 119–126 (2017).

186. Maller, R., Porte, Y., Alshareef, H. N. & McLachlan, M. A. Probing the doping mechanisms and electrical properties of Al, Ga and In doped ZnO prepared by spray pyrolysis. *J. Mater. Chem. C* (2016).

187. Franklin, J. B. *et al.* Optimised pulsed laser deposition of ZnO thin films on transparent conducting substrates. *J. Mater. Chem.* **21**, 8178–8182 (2011).

188. Liu, T., Chen, K., Hu, Q., Zhu, R. & Gong, Q. Inverted Perovskite Solar Cells: Progresses and Perspectives. *Adv. Energy Mater.* **6**, 1600457 (2016).

189. Yan, W. *et al.* Hole-Transporting Materials in Inverted Planar Perovskite Solar Cells. *Adv. Energy Mater.* **6**, 1–20 (2016).

190. Meng, L., You, J., Guo, T. F. & Yang, Y. Recent Advances in the Inverted Planar Structure of Perovskite Solar Cells. *Acc. Chem. Res.* **49**, 155–165 (2016).

191. Yu, H., Lu, H., Xie, F., Zhou, S. & Zhao, N. Native Defect-Induced Hysteresis Behavior in Organolead Iodide Perovskite Solar Cells. *Adv. Funct. Mater.* **26**, 1411–1419 (2016).

192. Credgington, D., Jamieson, F. C., Walker, B., Nguyen, T. Q. & Durrant, J. R. Quantification of geminate and non-geminate recombination losses within a solution-processed small-molecule bulk heterojunction solar cell. *Adv. Mater.* **24**, 2135–2141 (2012).

193. Collins, S. D., Proctor, C. M., Ran, N. A. & Nguyen, T.-Q. Understanding Open-Circuit Voltage Loss through the Density of States in Organic Bulk Heterojunction Solar Cells. *Adv. Energy Mater.* **6**, 1501721 (2016).

194. Heumueller, T. *et al.* Disorder-Induced Open-Circuit Voltage Losses in Organic Solar Cells During Photoinduced Burn-In. *Adv. Energy Mater.* **5**, 1500111 (2015).

195. Hawks, S. A. *et al.* Relating recombination, density of states, and device performance in an efficient polymer:fullerene organic solar cell blend. *Adv. Energy Mater.* **3**, 1201–1209 (2013).

196. Tress, W. Perovskite Solar Cells on the Way to Their Radiative Efficiency Limit – Insights Into a Success Story of High Open-Circuit Voltage and Low Recombination. *Adv. Energy Mater.* **7**, (2017).

197. Dane, W. *et al.* Impact of microstructure on local carrier lifetime in perovskite solar cells. **348**, 683–686 (2015).

198. Wetzelaer, G. J. A. H. *et al.* Trap-Assisted Non-Radiative Recombination in Organic-Inorganic Perovskite Solar Cells. *Adv. Mater.* **27**, 1837–1841 (2015).

199. Yang, M. *et al.* Do Grain Boundaries Dominate Non-Radiative Recombination in $CH_3NH_3PbI_3$ Perovskite Thin Films? *Phys. Chem. Chem. Phys.* **19**, 5043–5050 (2017).

200. Leijtens, T. *et al.* Carriers Trapping and Recombination: the Role of Defect Physics in Enhancing the Open Circuit Voltage of Metal Halide Perovskite Solar Cells. *Energy Environ. Sci.* **9**, 3472–3481 (2016).

201. Wang, Q. *et al.* Qualifying composition dependent p and n self-doping in CH3NH3PbI3. *Appl. Phys. Lett.* **105**, 163508 (2014).

202. Bi, C. *et al.* Understanding the formation and evolution of interdiffusion grown organolead halide perovskite thin films by thermal annealing. *J. Mater. Chem. A* **2**, 18508–18514 (2014).

203. Eng, M. P., Barnes, P. R. F. & Durrant, J. R. Concentration-dependent hole mobility and recombination coefficient in bulk heterojunctions determined from transient absorption spectroscopy. *J. Phys. Chem. Lett.* **1**, 3096–3100 (2010).

204. Hou, Y. *et al.* Overcoming the Interface Losses in Planar Heterojunction Perovskite-Based Solar Cells. *Adv. Mater.* **28**, 5112–5120 (2016).

205. deQuilettes, D. W. *et al.* Photo-induced halide redistribution in organic–inorganic perovskite films. *Nat. Commun.* **7**, 11683 (2016).

206. Petrus, M. L. *et al.* The Influence of Water Vapor on the Stability and Processing of Hybrid Perovskite Solar Cells Made from Non-Stoichiometric Precursor Mixtures. *ChemSusChem* **9**, 2699–2707 (2016).

207. Rehman, W. *et al.* Photovoltaic mixed-cation lead mixed-halide perovskites: links between crystallinity, photo-stability and electronic properties. *Energy Environ. Sci.* **10**, 361–369 (2017).

208. Du, T. *et al.* Probing and Controlling Intragrain Crystallinity for Improved Low Temperature–Processed Perovskite Solar Cells. *Adv. Funct. Mater.* **28**, 1803943 (2018).

209. Jeon, N. J. *et al.* Compositional engineering of perovskite materials for high-performance solar cells. *Nature* **517**, 476–480 (2015).

210. Snaith, H. J. Perovskites: the emergence of a new era for low-cost, high-efficiency solar cells. *J. Phys. Chem. Lett.* **4**, 3623–3630 (2013).

211. Liang, P. W. *et al.* Additive Enhanced Crystallization of Solution-Processed Perovskite for Highly Efficient Planar-Heterojunction Solar Cells. *Adv. Mater.* **26**, 3748–3754 (2014).

212. Seo, J., Noh, J. H. & Seok, S. Il. Rational Strategies for Efficient Perovskite Solar Cells. *Acc. Chem. Res.* **49**, 562–572 (2016).

213. Ball, J. M., Lee, M. M., Hey, A. & Snaith, H. J. Low-temperature processed meso-superstructured to thin-film perovskite solar cells. *Energy Environ. Sci.* **6**, 1739–1743 (2013).

214. Heo, J. H. *et al.* Planar CH3NH3PbI3 perovskite solar cells with constant 17.2% average power conversion efficiency irrespective of the scan rate. *Adv.*

Mater. **27**, 3424–3430 (2015).

215. Jeng, J. Y. *et al.* Nickel Oxide Electrode Interlayer in CH3NH3PbI3 Perovskite/PCBM Planar-Heterojunction Hybrid Solar Cells. *Adv. Mater.* **26**, 4107–4113 (2014).

216. Docampo, P., Ball, J. M., Darwich, M., Eperon, G. E. & Snaith, H. J. Efficient organometal trihalide perovskite planar-heterojunction solar cells on flexible polymer substrates. *Nat Commun* **4**, 2761 (2013).

217. Heo, J. H., Han, H. J., Kim, D., Ahn, T. K. & Im, S. H. Hysteresis-less inverted CH 3 NH 3 PbI 3 planar perovskite hybrid solar cells with 18.1% power conversion efficiency. *Energy Environ. Sci.* **8**, 1602–1608 (2015).

218. Malinkiewicz, O. *et al.* Metal-Oxide-Free Methylammonium Lead Iodide Perovskite-Based Solar Cells: the Influence of Organic Charge Transport Layers. *Adv. Energy Mater.* **4**, 1400345 (2014).

219. Yang, Z. *et al.* High-Performance Fully Printable Perovskite Solar Cells via Blade-Coating Technique under the Ambient Condition. *Adv. Energy Mater.* **5**, 1500328 (2015).

220. Kim, H., Lim, K.-G. & Lee, T.-W. Planar heterojunction organometal halide perovskite solar cells: roles of interfacial layers. *Energy Environ. Sci.* **9**, 12–30 (2016).

221. Xiao, M. *et al.* A Fast Deposition-Crystallization Procedure for Highly Efficient Lead Iodide Perovskite Thin-Film Solar Cells. *Angew. Chemie* **126**, 10056–10061 (2014).

222. Lekstrom, M., McLachlan, M. A., Husain, S., McComb, D. W. & Shollock, B. A. Using the in situ lift-out technique to prepare TEM specimens on a single-beam FIB instrument. in *Journal of Physics: Conference Series* (eds. Baker, R. T., Mobus, G. & Brown, P. D.) vol. 126 12028 (2008).

223. Mclachlan, M. A. *et al.* Probing local and global ferroelectric phase stability and polarization switching in ordered macroporous PZT. *Adv. Funct. Mater.* **21**, 941–947 (2011).

224. Li, D. *et al.* Size-dependent phase transition in methylammonium lead iodide perovskite microplate crystals. *Nat. Commun.* **7**, (2016).

225. Chueh, C. C. *et al.* Toward high-performance semi-transparent polymer solar cells: Optimization of ultra-thin light absorbing layer and transparent cathode architecture. *Adv. Energy Mater.* **3**, 417–423 (2013).

226. You, P., Liu, Z., Tai, Q., Liu, S. & Yan, F. Efficient Semitransparent Perovskite Solar Cells with Graphene Electrodes. *Adv. Mater.* **27**, 3632–3638 (2015).

227. Van Duren, J. K. J. *et al.* Relating the morphology of poly(p-phenylene vinylene)/ methanofullerene blends to solar-cell performance. *Adv. Funct. Mater.* **14**, 425–434 (2004).

228. Correa-Baena, J. P. *et al.* Changes from Bulk to Surface Recombination Mechanisms between Pristine and Cycled Perovskite Solar Cells. *ACS Energy Lett.* **2**, 681–688 (2017).

229. Correa-Baena, J. P. *et al.* Unbroken Perovskite: Interplay of Morphology, Electro-optical Properties, and Ionic Movement. *Adv. Mater.* **1**, 5031–5037 (2016).

230. You, J. *et al.* Low-temperature solution-processed perovskite solar cells with high efficiency and flexibility. *ACS Nano* (2014).

231. Du, T. *et al.* Probing and Controlling Intragrain Crystallinity for Improved Low Temperature–Processed Perovskite Solar Cells. *Adv. Funct. Mater.* **28**, 1803943 (2018).

232. Belisle, R. A., Jain, P., Prasanna, R., Leijtens, T. & McGehee, M. D. Minimal Effect of the Hole-Transport Material Ionization Potential on the Open-Circuit Voltage of Perovskite Solar Cells. *ACS Energy Lett.* **1**, 556–560 (2016).

233. Jiménez-López, J., Cambarau, W., Cabau, L. & Palomares, E. Charge Injection, Carriers Recombination and HOMO Energy Level Relationship in Perovskite Solar Cells. *Sci. Rep.* **7**, 6101 (2017).

234. Dar, M. I. *et al.* High photovoltage in perovskite solar cells: New physical insights from the ultrafast transient absorption spectroscopy. *Chem. Phys. Lett.* **683**, 211–215 (2017).

235. Lim, K. G. *et al.* Boosting the power conversion efficiency of perovskite solar cells using self-organized polymeric hole extraction layers with high work function. *Adv. Mater.* **26**, 6461–6466 (2014).

236. Khadka, D. B., Shirai, Y., Yanagida, M., Ryan, J. W. & Miyano, K. Exploring the effects of interfacial carrier transport layers on device performance and optoelectronic properties of planar perovskite solar cells. *J. Mater. Chem. C* **5**, 8819–8827 (2017).

237. Tvingstedt, K. *et al.* Removing Leakage and Surface Recombination in Planar Perovskite Solar Cells. *ACS Energy Lett.* **2**, 424–430 (2017).

238. Wijeyasinghe, N. *et al.* Copper(I) Thiocyanate (CuSCN) Hole-Transport Layers Processed from Aqueous Precursor Solutions and Their Application in Thin-Film Transistors and Highly Efficient Organic and Organometal Halide Perovskite Solar Cells. *Adv. Funct. Mater.* **27**, 1701818 (2017).

239. Maennig, B. *et al.* Organic p-i-n solar cells. *Appl. Phys. A* **79**, 1–14 (2004).

240. He, Z. *et al.* Enhanced power-conversion efficiency in polymer solar cells using an inverted device structure. *Nat. Photonics* **6**, 591–595 (2012).

241. Cha, H. *et al.* An Efficient, “Burn in” Free Organic Solar Cell Employing a Nonfullerene Electron Acceptor. *Adv. Mater.* **29**, 1–8 (2017).

242. Yang, M. J. *et al.* Photoluminescence analysis of InGaP top cells for high-efficiency multi-junction solar cells. *Sol. Energy Mater. Sol. Cells* **45**, 331–339 (1997).

243. Metzger, W. K. *et al.* Recombination kinetics and stability in polycrystalline Cu(In,Ga)Se2 solar cells. *Thin Solid Films* **517**, 2360–2364 (2009).

244. Wehrenfennig, C., Eperon, G. E., Johnston, M. B., Snaith, H. J. & Herz, L. M. High charge carrier mobilities and lifetimes in organolead trihalide perovskites. *Adv. Mater.* **26**, 1584–1589 (2014).

245. Harwell, J. R. *et al.* Probing the energy levels of perovskite solar cells: Via Kelvin probe and UV ambient pressure photoemission spectroscopy. *Phys. Chem. Chem. Phys.* **18**, 19738–19745 (2016).

246. Yablonovitch, E. SOLAR CELLS. Lead halides join the top optoelectronic league. *Science* **351**, 1401 (2016).

247. Bryant, D. *et al.* Light and oxygen induced degradation limits the operational stability of methylammonium lead triiodide perovskite solar cells. *Energy Environ. Sci.* **9**, 1655–1660 (2016).

248. Burschka, J. *et al.* Tris(2-(1 H -pyrazol-1-yl)pyridine)cobalt(III) as p-type dopant for organic semiconductors and its application in highly efficient solid-state dye-sensitized solar cells. *J. Am. Chem. Soc.* **133**, 18042–18045 (2011).

249. Irwin, M. D., Buchholz, D. B., Hains, A. W., Chang, R. P. H. & Marks, T. J. p-Type semiconducting nickel oxide as an efficiency-enhancing anode interfacial layer in polymer bulk-heterojunction solar cells. *Proc. Natl. Acad. Sci.* **105**, 2783–2787 (2008).

250. Wheeler, S. *et al.* Influence of Surface Recombination on Charge-Carrier Kinetics in Organic Bulk Heterojunction Solar Cells with Nickel Oxide Interlayers. *Phys. Rev. Appl.* **4**, 29–31 (2015).

251. Yamashita, M., Otani, C., Okuzaki, H. & Shimizu, M. Nondestructive measurement of carrier mobility in conductive polymer PEDOT:PSS using terahertz and infrared spectroscopy. *2011 30th URSI Gen. Assem. Sci. Symp. URSIGASS 2011* **1**, 3–6 (2011).

252. Zhang, F. *et al.* Interfacial Oxygen Vacancies as a Potential Cause of Hysteresis in Perovskite Solar Cells. *Chem. Mater.* **28**, 802–812 (2016).

253. Leijtens, T. *et al.* Overcoming ultraviolet light instability of sensitized TiO 2 with meso-superstructured organometal tri-halide perovskite solar cells. *Nat. Commun.* **4**, 2885 (2013).

254. Jäckle, S. *et al.* Junction formation and current transport mechanisms in hybrid n-Si/PEDOT:PSS solar cells. *Sci. Rep.* **5**, 1–12 (2015).

255. Wijeyasinghe, N. *et al.* p-Doping of Copper(I) Thiocyanate (CuSCN) Hole-Transport Layers for High-Performance Transistors and Organic Solar Cells. *Adv. Funct. Mater.* **28**, 1–14 (2018).

256. Credgington, D. & Durrant, J. R. Insights from transient optoelectronic analyses on the open-circuit voltage of organic solar cells. *J. Phys. Chem. Lett.* **3**, 1465–1478 (2012).